ACCOUNTING FOR NONUNIFORM INDUCED PROPERTIES IN PRODUCTION ANALYSIS OF UNCONVENTIONAL RESERVOIRS

A Dissertation

by

GORGONIO FUENTES CRUZ

Submitted to the Office of Graduate and Professional Studies of
Texas A&M University
in partial fulfillment of the requirements for the degree of

DOCTOR OF PHILOSOPHY

Chair of Committee,	Eduardo Gildin
Co-Chair of Committee,	Peter P. Valkó
Committee Members,	Thomas A. Blasingame
	Zenon Medina-Cetina
Head of Department,	A. Daniel Hill

December 2014

Major Subject: Petroleum Engineering

ABSTRACT

Several conceptual models for unconventional reservoirs have been proposed in recent years based on extensions of well-studied analytical/semi-analytical models for conventional reservoirs. The standard semi-analytical approaches assume uniform properties in the reservoir. In this study, we develop new models for production data analysis of hydraulically fractured wells based on the concept of nonuniform induced properties, in particular, the induced permeability field and the induced interporosity flow field. In the induced permeability field approach, we consider the case when the hydraulic fracturing operation alters the ability of the formation to conduct fluids throughout, but in varying degrees depending on the distance from the main hydraulic fracture plane. In the induced interporosity flow field, we assume that, as a result of the hydraulic fracturing treatment, the density of micro-fractures (natural and induced) is high near the hydraulic fracture face, but gradually decreases away from it.

We also address common issues related to variations in the wellbore pressure, desorption effects, and non-linearity caused by gas flow, with the intent to provide a simple, yet clear understanding of their effects on the production performance.

The methods used in this work include mostly semi-analytical techniques (Laplace transform and numerical inversion to the time domain). Analytical (formulae in the time domain) and numerical simulation (finite difference) techniques are also used to validate

the results from the new models. The results indicate that the maximum and minimum induced permeabilities may provide the key to evaluate the overall completion efficiency in unconventional formations, where the extent and quality of the stimulated volume are equally significant. Also, the closely spaced micro-fractures have a strong impact on well performance, even when their density is diminishing toward the far parts of the stimulated reservoir. We conclude that the new models preserve the typical linear-flow signature of commonly observed well performance of unconventional shale reservoirs; however, the extrapolation of the production behavior departs from the standard models significantly.

This research contributes to the understanding of the production behavior of unconventional reservoirs to characterize the quality of the stimulated reservoir and to consider often neglected factors effecting forecasts of well performance.

DEDICATION

This dissertation is dedicated to my mother, Violeta, my sister Reyna, and my brothers Sergio, Manuel and Roberto for all the love and support they have provided me throughout my life.

Inspiration unlocks the future; technology will catch up.

— a line of dialogue in The Wind Rises, from Hayao Miyazaki

ACKNOWLEDGEMENTS

I would like to thank the following for their contributions to this work: Dr. Peter P. Valkó, co-chair of my advisory committee, for his teaching, guidance and long discussions. Dr. Eduardo Gildin, chair of my advisory committee, for his guidance, teaching and encouragement. Dr. Thomas A. Blasingame and Dr. Zenon Medina-Cetina, for serving on my advisory committee and for their suggestions throughout the course of this research.

Thanks also go to my friends, colleagues, faculty and staff of the Harold Vance Department of Petroleum Engineering for making my time at Texas A&M University a great experience. I also want to extend my gratitude to the Mexican Petroleum Institute and the Conacyt–Sener–Hidrocarburos Fund for providing the funding for this research.

Finally, thanks to my mother and siblings for their encouragement and patience.

TABLE OF CONTENTS

Page

LIST OF FIGURES

Page

LIST OF TABLES

Page

1. INTRODUCTION *

Many models of analytic, semi-analytic and numerical nature have been proposed in recent years, responding to the fast paced transformation in the type of formations produced and the completion configurations applied, especially in US onshore fields. From the geological and geophysical perspective the most prominent unconventional resource is shale gas, but several other formation-fluid combinations are also within the reach of current technology (Bohacs et al. 2013). Common to all these *unconventional resources* are the organic-matter-rich matrix with small pore sizes, extreme low permeability measured in laboratory conditions, and the inherently related lack of migration.

---

*Part of this section is reprinted with permission from Fuentes-Cruz, G., Gildin, E., and Valkó, P.P. 2014. Capturing the Essence of Flow from Unconventional Reservoirs. *Hydraulic Fracturing Quarterly* **1** (01): 39–53. Copyright [2014] by Hydraulic Fracturing Quarterly journal.

The storage and flow mechanisms involved are certainly richer than what was once considered in traditional reservoir engineering (Akkutlu and Fathi 2012), but many of these peculiarities have been already successfully incorporated into the traditional petroleum engineering toolkit. Adsorption, diffusion, slippage, natural fractures, spatially composite reservoir models have been with us for decades (Abdassah and Ershaghi 1986; King and Ertekin 1991).

The word unconventional also implies massive stimulation, with the multi-fractured horizontal well as the new standard configuration. Models of various complexities for this configuration have also been available for a long time, arching from Mukherjee and Economides (1991) and Larsen and Hegre (1991) through Raghavan et al. (1997) to Meyer et al. (2010), to mention just a few.

The currently accepted conceptualization of hydraulic stimulation of shale formations is strongly related to the monitoring of the treatments using microseismic monitoring (Maxwell et al. 2002; Mayerhofer et al. 2006, 2010; Wuestefeld et al. 2012). It is widely accepted, that during the treatment a complex network of fracture branches evolve, penetrating deeply into the formation. With the opening faces slipping relative to each other, a partially open conductive structure remains in place after the injection ends. The observations have led to the introduction of two significant concepts. Stimulated Reservoir Volume (SRV) refers to the affected space (within the envelope of the detected microsesmicity) as described e.g. in Mayerhofer et al. (2010). The second

concept, Fracture Complexity, refers to the irregularity in the temporal-spatial appearance of the detected events (Fisher et al. 2005) that is believed to correspond to propagation arrest and branching. Both these phenomenological concepts have been widely adopted (Gale et al. 2007; King 2010), but with considerable variability in the meaning.

A great body of work is available regarding network evolution, including laboratory experiments (Renshaw and Pollard 1995; Zhou et al. 2008; Jeffrey et al. 2009; Suarez-Rivera et al. 2012), mine-back observations (Warpinski and Teufel 1987), and various numerical models (Olson and Taleghani 2009; Gu et al. 2011; Fu et al. 2013).

Nevertheless, there are many open questions. There is no clear consensus, whether the branches of the network form a single, connected tree-like structure or not, whether they consist of reopened pre-existing natural fractures and/or newly induced fractures evolving along structural weaknesses, whether tensile or shear failure is involved in the actual opening. Little is known about what measurable formation properties may be responsible for a specific network behavior. Laboratory experiments can illustrate concepts but suffer from the scale discrepancy. The networks cannot easily be observed directly in the subsurface and microseismic interpretations are nonunique.

A consensus exists with respect to the basic effect: even if the proppant material cannot reach a certain branch of the network, or even if the branch is not connected to the

perforations, the slippage caused by residual opening or some other type of rock failure provides increased flow capacity within its vicinity.

From the petroleum production perspective, we can distinguish three broad groups of models. The first group idealizes the completion/stimulation as superposing on the formation matrix a tree-like fracture network rooted from the perforation cluster. The models attempt to describe the actual geometry of the structure and its function in receiving flow through its walls and conducting flow to the perforations (Dershowitz and Miller 1995). In this explicit hydraulic fracture modeling or discrete fracture network (DFN) approach a particularly attractive element is, that details of the microseismic trace can be directly used as input (Mirzaei and Cipolla 2012). A less attractive element is the inherent necessity of stochastic initialization of the natural fracture network that will affect both the propagation and the production model. The DNF approach is based on the stochastic modeling concept and therefore, every realization of the Discrete Natural Fracture network will produce different results.

The second group retains the concept of primary hydraulic fracture connected to the perforations and accounts for all other secondary effects in a continuum (or double continuum) description of the SRV. The primary fracture is often idealized as a fully penetrating (both vertically and laterally) infinite conductivity fracture (Bello and Wattenbarger 2010; Kanfar et al. 2013); but some authors take into account additional details in the description of the primary hydraulic fractures (Al Rbeawi and Tiab 2012).

If such a model is combined with the dual porosity idealization, it is natural to consider the altered permeability only in the fracture medium and within the SRV (Brown et al. 2011; Ozkan et al. 2011). Mathematically, such shale models are not new; they belong to the large class of composite reservoir models. Composite models contain a large number of model parameters and almost always suffer from the problem of non-uniqueness of the parameter set identified from production data. As many new type curve families are generated, with more and more *humps* and similar features, without evidence of having anything similar in real data, the analyst have little choice but relying on default values. However, more unique individual phenomena such as *frac hits* are still out of the reach of even the most sophisticated models (Ajani and Kelkar 2012). Meanwhile, production data usually show a recurrent behavior that can be captured by a minimum number of parameters (Nobakht and Mattar 2012). There is a third group of models, accounting for all effects of the stimulation treatment in a completely continuum approach, see e.g. Wang and Liu (2011).

The approach introduced in this work belongs to the second group: considering the primary hydraulic fracture connected to the perforations and accounting for all other secondary effects in a continuum framework.

Considering the main distinctive feature of unconventional production data, we build upon the fundamental linear flow geometry in physical space with the sink located at the hydraulic fracture face, but also capture the effect of induced nonuniform properties in

two approaches: 1) induced permeability field in the bulk of the formation with increasing flow capacity (permeability-area product) along a streamline approaching the sink, 2) induced interporosity-flow field that originates as a consequence of the nonuniform matrix block size. The matrix-block-size distribution may result from the opening or generation of fractures; the density of these fractures (natural and induced) is assumed to be higher near the hydraulic fracture face, leading to a reduction in the characteristic dimension (of the matrix blocks) along a streamline approaching the hydraulic fracture.

Based on the above, the objectives of this research are:

- Develop the *induced permeability field* model within the single medium and dual porosity/dual permeability idealization. Generate type curves for production data analysis, as well as closed form approximate solutions in the time domain. Also, analyze field data to introduce practical guidelines for the analysis of production data of massively stimulated reservoirs.
- Develop the *induced interporosity-flow field* model in the dual porosity/dual permeability idealization. Provide type curves for production data analysis, as well as closed form approximate formulae in the time domain.
- Investigate the *decaying wellbore pressure* solutions to determine the effects of commonly observed trends of wellbore pressure on the well performance.

- Investigate the effects of desorption and nonlinearities caused by gas properties to quantify the impact of using semi-analytical models in the analysis of production data from unconventional reservoirs.
- Strengthen the diagnostics based on standard plots, by using the dimensionless group $q_w t/G_p$. This dimensionless group can be interpreted as the ratio between the actual time and the material balance time.

The addition of the induced permeability field and induced interporosity-flow field approaches into the semi-analytical group of models is significant because the standard models consider uniform properties. The new semi-analytical approaches are important to characterize the stimulated volume and to consider often neglected factors effecting forecasts in the well performance of multi-fractured horizontal wells producing in shale systems. Alternative determinant features, such as nonuniform permeability, nonuniform matrix-block size and the analytical treatment of the variable wellbore pressure, are crucial to explaining the production performance in shale reservoirs. Also, this work contributes in the diagnostics of production data by the use of the dimensionless group $q_w t/G_p$, which enables identifying departures from the typical flow regimes observed in the well performance of unconventional reservoirs.

In this work, we start by introducing the induced permeability field concept within the single and double-porosity/double-permeability frameworks in section 2 and section 3, respectively. Then, we present the induced interporosity-flow field approach in section

4. We also present, in section 5, the discussion of the effects of nonlinearities caused by gas properties, as well as the effect of desorption in the well performance. Finally, the conclusions are stated in section 6.

2. THE INDUCED PERMEABILITY FIELD – SINGLE POROSITY *

2.1. Introduction

Standard models for production data analysis of hydraulically fractured wells assume uniform permeability throughout the reservoir (Wattenbarger et al. 1998; El-Banbi and Wattenbarger 1998). Nevertheless, the fracturing treatment induces a permeability alteration around the hydraulic fracture because of the shear or tensile failure of the natural fractures away from the main fracture plane (Palmer et al. 2007; Ge and Ghassemi 2011). Thus, in this work we consider that the average effect of the failure of weak planes leads to a nonuniform permeability distribution depending on the distance to the hydraulic fracture. The present approach uses minimum reference to geomechanics; it does not involve description of stress fields.

---

*Reprinted with permission from Fuentes-Cruz, G., Gildin, E., and Valkó, P.P. 2014. Analyzing Production Data from Hydraulically Fractured Wells: The Concept of Induced Permeability Field. *SPE Reservoir Evaluation & Engineering* **17** (02): 220–232. http://dx.doi.org/10.2118/163843-PA. Copyright [2014] by Society of Petroleum Engineers.

The assumption of nonuniform reservoirs is common in fractal theory (the use of concepts of diffusion on fractal-like structures that leads to anomalous diffusion) either for well pressure testing (Barker 1988; Chang and Yortsos 1990) or production data analysis (Camacho et al. 2008). Beier (1994) developed a model for a vertically fractured well producing in a fractal reservoir under transient conditions, but most of the models in fractal theory are available for radial flow geometry. Essentially, one can always achieve the signature of fractal theory results by assuming a varying permeability-area product that uses a power-law relationship.

In massively stimulated reservoirs the permeability-area product increases along a streamline approaching the fracture. The power-law relation for flow capacity, which would require a negative exponent under this situation, diverges in a linear geometry when the inner boundary condition is evaluated at the fracture face. This issue severly limits the applicability of power-law functions not only because they become singular under the assumption of fracture width equal to zero, but also because of the extreme sensitivity to any assumed non-zero width. Pondering the behavior of power-law related models and recognizing common signatures in production field data sets, we suggest exponential and linear functions to represent the permeability field. We assume that these functions depend on the distance to the main fracture plane and on the dimensionless threshold permeability (the reciprocal stimulation ratio), which is defined next.

Current models do not address the effect of the permeability alteration around the fractures on the scale of well-spacing; we account for this effect by using the stimulation ratio concept, which represents how the permeability in the zone near the fracture compares with the threshold permeability. The threshold permeability, created by the fracturing treatment, is the minimum value of permeability in the stimulated reservoir volume. The functions describing permeability must converge to the uniform case when the stimulation ratio is equal to one.

The specific functional form to describe the post-hydraulic-fracturing permeability depends on the fluid-rock interactions and the geomechanics involved during (and after) the fracturing treatment. Hummel and Shapiro (2013) obtained nonlinear permeability distributions (during the generation of the hydraulic fracture) using microseismic data from Barnett shale. They found the largest permeability magnitudes at small radial distances from the borehole. For production data analysis purposes, the magnitude and shape of the permeability distribution at the end of the hydraulic fracture evolution might change as a consequence of the abrupt pressure drop generated when the well is set to production. Geomechanical analysis together with the microseismics can provide useful insights for understanding the stimulated reservoir, though some key attributes, such as the mechanics of the hydraulic fracture, can be aseismic (Warpinski et al. 2013). In this work, we assume exponential and linear distributions because they are the simplest way to incorporate the monotonic decrease of the permeability enhancement as the distance to the hydraulic fracture increases. This new approach is consistent with the observation

of more stimulation near the hydraulic fracture and introduces the minimum additional parameters, suitable for production data analysis. The power-law relation can also be considered, provided that the divergence at zero hydraulic fracture width is avoided; this can be achieved by assuming a composite stimulated-reservoir (between the hydraulic fractures) with two regions: one narrow zone around the hydraulic fracture plane with finite permeability, and a second zone having a decreasing permeability profile with a power-law type variation. Composite-region models involving power-law distributions (with the corresponding increase in the number of parameters) have been proposed in the literature for radial systems to describe permeability or mobility variations in falloff tests (Poon 1995; Fuentes-Cruz et al. 2010).

Results from the induced permeability model show that decline type curves (Fetkovich 1980; Doublet et al. 1994) enable identifying features commonly ignored with the uniform model. The differences between these models are evident not only in the production decline curves, but also in the dimensionless productivity index (Helmy and Wattenbarger 1998). These differences are significant in the late-transient and boundary-dominated periods.

We note that the concept of the induced permeability field can be extended to the dual porosity framework (considering either transient or pseudosteady fluid transfer from matrix to fractures) such that the natural and induced fractures, affected and/or created by the intensive stimulation, have distance-dependent properties. The inclusion of the

second medium brings out two additional dimensionless parameters, the fracture storativity and the interporosity flow coefficient. The combination of these parameters, together with the dimensionless threshold permeability, leads to a rich variety of phenomena addressed in section 3. Here, we focus on the cases where the total system (or one intensively stimulated subsystem) is dominant and hence a single-porosity model is appropriate. We show that many features important for analyzing unconventional wells are already present in the single medium version of the model. This approach explains, in a direct manner, the production behavior of fractured wells from shale gas reservoirs exhibiting skin factor effect, transient linear flow, late-transient flow, and late-time boundary effects.

2.2. Nonuniform induced permeability field: the new approach

This section presents a discussion about the implications of the nonuniform permeability field on the well performance, as well as a summary of the equations derived for the single porosity model. One should refer to Appendix A, which presents the mathematical model in dimensionless form and the details of the derivations. The initial and boundary conditions are similar to those commonly used in well testing and decline curve analysis. To our knowledge, the solution in Laplace space has not been published before. In checking the formulation we used Mathematica (Wolfram 2012) extensively. The Laplace space solution was numerically inverted using the multi-precision Gaver-Wynn-Rho algorithm (Valkó and Abate, 2004). Additionally, we solved special cases analytically to verify the correctness of the numerical results.

2.2.1. Model description

Fig. 2.1 depicts a hydraulically fractured well producing in a closed SRV. In shale reservoirs, the volume affected by the fracturing operation is the SRV (Mayerhofer et al. 2010). The enhancement of the stimulated volume originates from the shear or tensile failure of the natural fractures away from the main fracture plane. Thus, natural (or induced) fractures are reopened (or opened) leading to an altered system whose permeability distribution is not uniform.

Although the fracturing operation induces a fracture network with a complex geometry, it is reasonable to expect the highest value of permeability (k^0) near the main fracture plane. As the distance to the fracture plane increases, the permeability enhancement reduces until it reaches a minimum value (k^*) because the energy coming from the fracturing treatment dissipates. This threshold permeability is also induced by the fracturing operation; it is inside the SRV element and there is no significant flow beyond its position (y^*) because: a) there is a plane of symmetry between adjacent SRV elements acting as an equivalent no-flow boundary or b) there is no induced permeability as a result of the energy dissipation of the fracturing operation. The permeability of the non-induced medium is the formation, matrix, or virgin permeability. We consider that the drainage area is confined to the SRV (where Darcy's law is valid) because the contribution of the non-induced region, having sub-microdarcy permeability, is negligible (Mayerhofer et al. 2006).

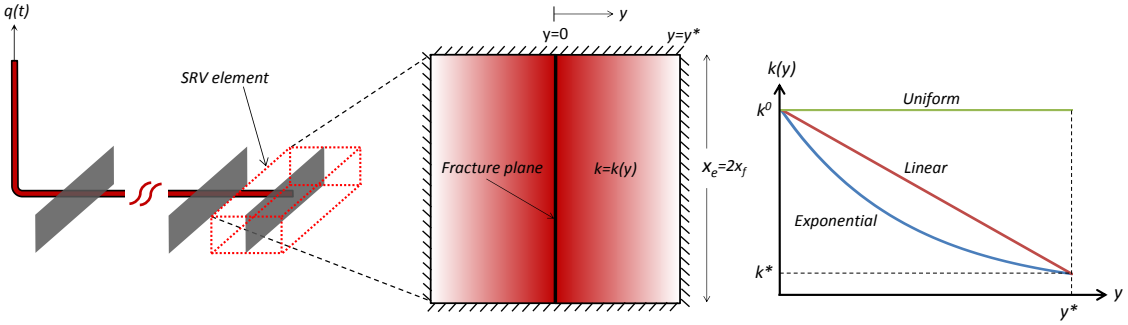

Fig. 2.1—New model for fracture-stimulated reservoirs. Exponential and linear functions represent the permeability field after fracturing operation.

In Fig. 2.1, the SRV element has a rectangular geometry with length $2y^*$, width x_e, and thickness h. The infinite conductivity fracture, located at the middle of the SRV element, fully penetrates the reservoir in both height (h) and lateral extent (x_e). This means that the hydraulic fracture length ($2x_f$) is equal to the lateral extent of the stimulated volume ($2x_f = x_e$). Although the evaluation of the fracture length is usually a target of production data analysis (PDA), nonuniqueness issues have been reported when estimating fracture length using PDA, even for models assuming uniform permeability field (Cipolla et al. 2009). Recent efforts have been addressed for fracture length estimation by using 2-phase flow-back data (Clarkson and Williams-Kovacs 2013) as well as the integration of different sources such as fracture model calibrated with microseismic mapping (Cipolla et al. 2009).

If we assume that there is a plane of symmetry between adjacent SRV elements acting as a no-flow boundary, then the length of the SRV element in the y direction can be

approximated as half the distance between the main hydraulic fracture planes. Additionally, we assume that there is no interference between the adjacent wellbores.

The induced permeability is an exponential or linear function of the distance to the fracture plane (Eqs. A-8 and A-9). The value of permeability at the fracture face is equal to k^0, and the value at the boundary of the SRV element (y^*) is equal to k^*.

In dimensionless form, the permeability field goes from 1 (at $y_D = 0$) to k_D^* (at $y_D = y_D^* = y^*/x_f$). The parameter $k_D^* = k^*/k^0$ is the dimensionless threshold permeability. The ratio $k^0/k^* = 1/k_D^*$ is the stimulation ratio (SR) that shows how many times the permeability is induced near the fracture face compared to the induced permeability at the outer boundary. The permeability field collapses to the uniform case for *SR*=1.

The new model is SRV based (Mohaghegh 2013) because the focus is not on the determination of the size of the SRV (which we consider set by the stage spacing) but on the deterioration of flow capacity away from the fracture face of the primary hydraulic fracture.

It is important to distinguish between the physical model and the flow model. Although the physical model (shear and tensile failure of the formation rock and reopening natural fracture network) is complex, the flow model is addressing only the most relevant aspect: the effect of flow-capacity decrease away from the fracture. In this case, the flow

model is a standard single-medium, homogenous model with location dependent permeability. This approach introduces only one additional parameter which is a distinct advantage in production data analysis where we often have to cope with the ill-posed nature of the parameter estimation problem.

2.2.2. Production behavior for exponential and linear permeability fields

Fig. 2.2 shows the well performance for an exponential permeability field and zero skin factor from synthetic data. The short-time approximation in dotted line on Fig. 2.2A ($q_{wD\text{-}STA}$, Eq. A-21) indicates that the linear flow regime (half-slope line on log-log plot) is the same irrespective of the dimensionless threshold permeability. Therefore, identifying the value of the dimensionless threshold permeability (or the value of the stimulation ratio) by using data only during the transient linear flow is not possible because the production behavior is a function of the maximum induced permeability (k^0):

$$q_g = \frac{n_{HF} h \sqrt{(\phi \mu c_t)_i}\,[m(p_i) - m(p_{wf})]}{315.1\,T} x_f \sqrt{k^0} \sqrt{\frac{1}{t}} \quad \text{.....(2.1)}$$

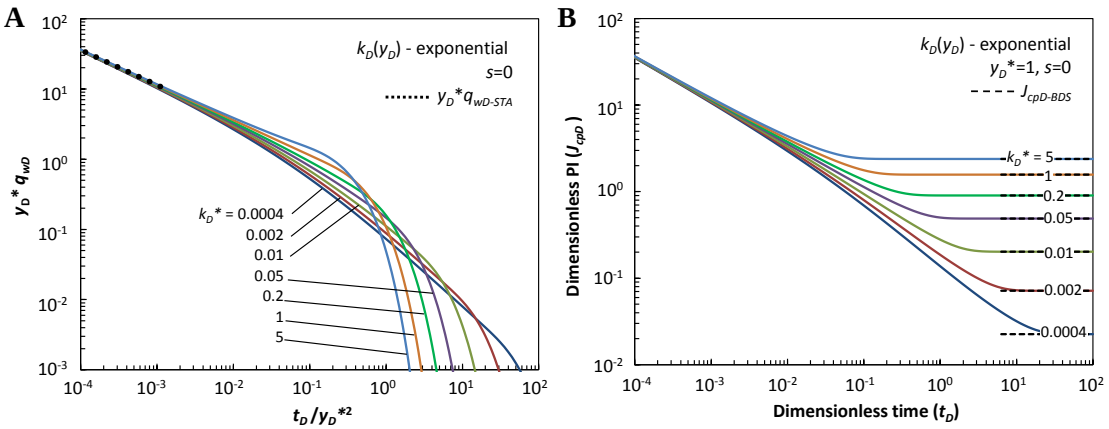

Fig. 2.2—The dimensionless threshold permeability strongly affects the well performance of fracture-stimulated reservoirs with exponentially-varying permeability.

Fig. 2.2A also illustrates that the dimensionless threshold permeability controls the deviation from the transient linear flow and as a consequence, the onset of the boundary-dominated state: the lower the threshold permeability, the earlier the departure from the linear flow (and later the beginning of the boundary-dominated state). In this work, we use the terminology boundary-dominated state (BDS) to describe the long-time behavior when all the boundaries influence the well performance, flowing at constant wellbore pressure. We use pseudosteady state (PSS) to describe the analogous long-term behavior when the well is flowing at constant wellbore rate.

The format shown in Fig. 2.2A was proposed by Wattenbarger et al. (1988); it enables collapsing all the curves for different values of y_D*. This means that whatever the elongation (on a horizontal plane) of the SRV element, the shape of the production response is the same; it is only shifted in the vertical and horizontal directions. A similar reasoning is conducted for a vertical elongation because the gravitational forces are

ignored. For a given lateral reservoir extent (x_e), the vertical elongation can be quantified by the ratio h/y^*.

The analytical approximation of dimensionless productivity index (denoted as PI) during BDS ($J_{cpD\text{-}BDS}$, Eq. A-23) accurately predicts the stabilized value at long times (dashed lines on Fig. 2.2B). Computing $J_{cpD\text{-}BDS}$ from the analytical expression is straightforward in common spreadsheet programs. We obtained this expression following the procedure of Hagoort (2011). As expected, as the dimensionless threshold permeability increases, the dimensionless PI during BDS also increases because of the higher flow capacity in the overall SRV element.

Fig. 2.3 shows the well performance for a linear permeability field. Similar to the exponential case, the transient linear flow is independent of the dimensionless threshold permeability. In this case, the deviations from the uniform case are less evident than the exponential case, but still significant. We observe that the well performance shows the same behavior if $k_D^* \leq 0.01$. Thus, if the induced permeability field is linear, then we cannot characterize the contrast between the maximum and minimum permeabilities for high values of stimulation ratio ($SR=1/k_D^* \geq 100$). The dashed lines in Fig. 2.3B show that Eq. A-24, for $J_{cpD\text{-}BDS}$, is precise. These values represent a necessary reference in reservoir engineering, even when the time for reaching the BDS is long in shale gas reservoirs.

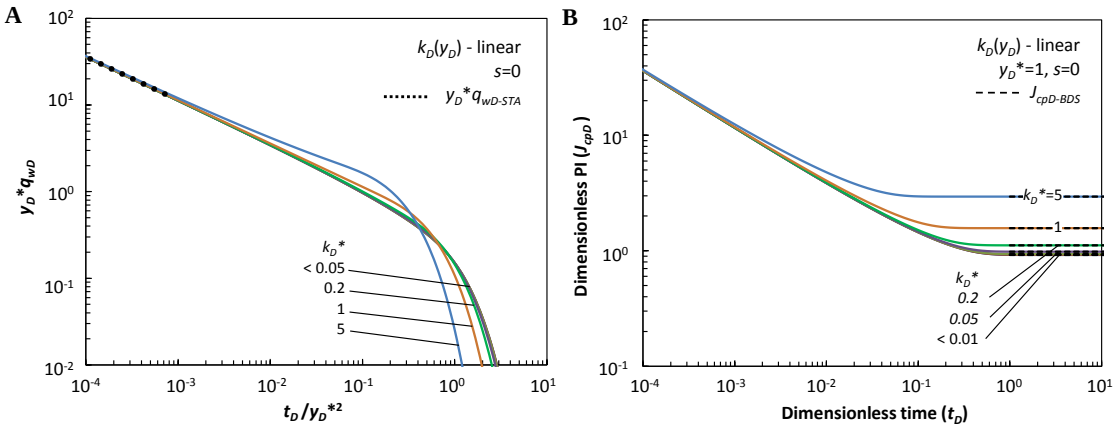

Fig. 2.3—The well performance of fracture-stimulated reservoirs with linearly-varying permeability departs from the uniform case. If k_D* is less than 0.01, then well performance shows the same behavior irrespective of the value of k_D*.

From **Fig. 2.4,** the well performance for exponential, linear, and uniform permeability distributions has a discernible signature after the linear flow regime; this enables not only determining the stimulation ratio, but also characterizing the permeability distribution (exponential, linear, or uniform) by analyzing production data reaching the late-transient and/or boundary-dominated state. Taking the uniform permeability field as a reference, the exponential and linear permeability fields exhibit an earlier and smoother transition from linear to BDS, leading to a longer transition between linear flow and BDS.

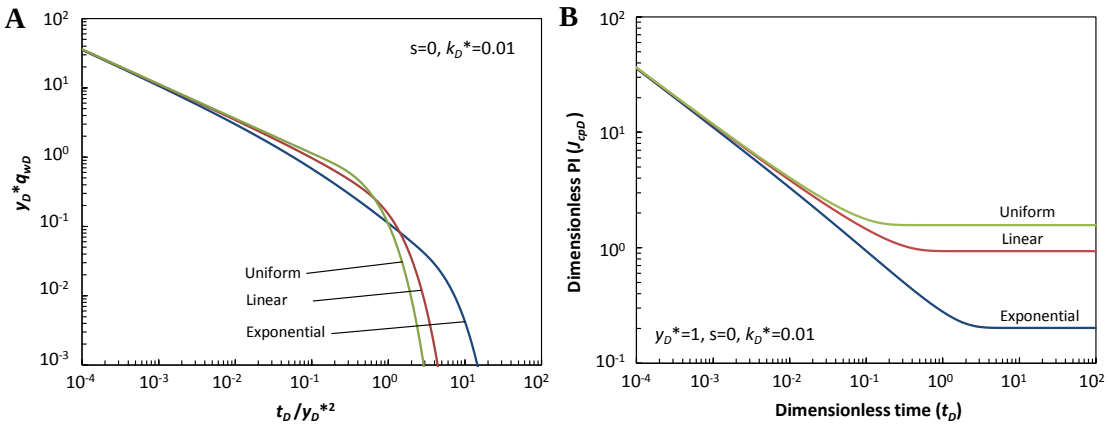

Fig. 2.4—Characteristic signatures of the three different permeability distributions appear at intermediate and late time.

In general, during the transient linear flow the production decline curves of the uniform permeability field show the same behavior as the exponential and linear cases (Eq. A-21). Thus, we cannot distinguish between them by analyzing production data only from the linear flow regime because the production behavior is a function of the maximum induced permeability in all three cases, provided that the permeability near the fracture face is the same for the three distributions. This explains, in addition to the reasons provided by Wattenbarger et al. (1998), the frequent occurrence of the linear flow and justifies the use of the uniform permeability model during the transient linear flow but also emphasizes the potential and uncertain departure from it at intermediate and late times. Thus, we should be extremely careful to use the uniform permeability model for the forecast of production data and SRV characterization.

The dimensionless PI is also affected by the permeability distribution during the late transient and BDS (Fig. 2.4B). **Fig. 2.5** shows that, during BDS and PSS, the

dimensionless PI for exponential permeability field exhibits a considerable reduction for small values of k_D*. This is likely to be the case in real situations according to our approach of lower permeability enhancement at larger distances from the hydraulic fracture plane. The significant relative difference between $J_{cpD\text{-}BDS}$ and $J_{crD\text{-}PSS}$ in the case of exponential field is understandable if we think about the fact that, during BDS (constant wellbore pressure), more of the produced fluid comes from further places than during PSS (constant wellbore rate). In the case of exponential induced permeability field, it means that flow must travel from places where the permeability is very low compared to k^0.

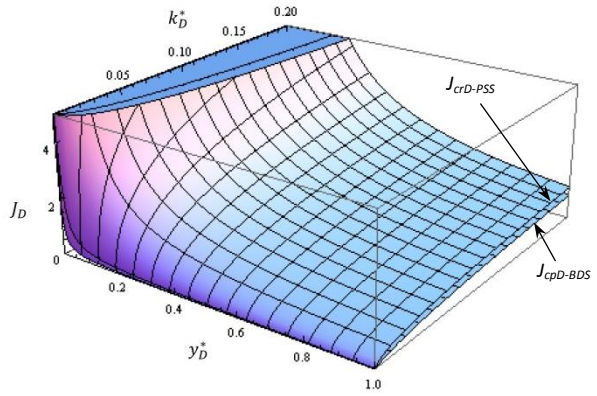

Fig. 2.5—During BDS (constant wellbore pressure) and PSS, the dimensionless PI for exponential permeability field exhibits a significant reduction as k_D* decreases, specially at small values of k_D*.

The skin factor modifies the transient linear flow. As a result, the production rate flattens at short time (**Fig. 2.6**). According to Eq. A-31, similar to the equation for uniform reservoirs (Bello 2009), the early-time approximation of dimensionless reciprocal rate is

equal to the skin factor (dashed lines on Fig. 2.6A). This feature is useful to estimate the skin factor from field data:

$$s = \frac{n_{HF}k^0h[m(p_i)-m(p_{wf})]}{1423T}\frac{1}{q_g} \quad \text{.....(2.2)}$$

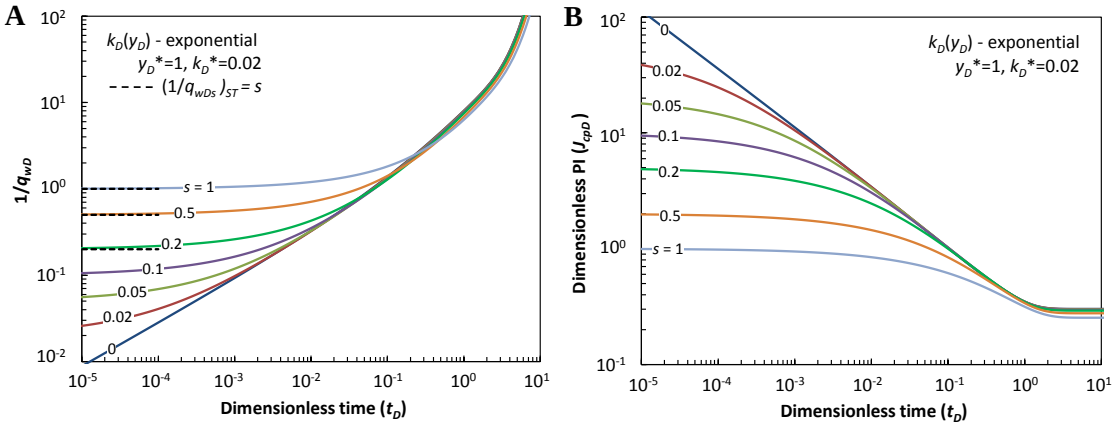

Fig. 2.6—Small values of skin factor control the behavior of the production decline curves during the early (skin dominated) and intermediate transient periods, irrespective of the actual functional form of the induced permeability field.

From Fig. 2.6, we conclude that the influence of skin factor on production behavior is strong and can affect the well performance even at long times. We note that Eq. A-31 is also valid for radial geometry. Nevertheless, the flattening originated from the skin factor disappears at extremely short times. This might explain why Eq. A-31 is not popular in conventional reservoir evaluations (where radial flow is the most frequent flow regime, and linear flow appears at extremely short times). Also, in conventional reservoirs the standard tools for formation evaluations are the pressure transient tests,

usually affected by wellbore storage masking any presence of pressure stabilization (because of skin factor effect) at short times. These equations (Eq. A-31 and Eq. 2.2) become more useful for analyzing unconventional reservoirs where the linear flow lasts for a long time.

In summary, Figs. 2.2 through 2.6 illustrate that the production behavior for the induced nonuniform permeability field departs considerably from the uniform case (*SR*=1). We identify a *skin-dominated* period at short times, and then a transient linear flow occurs for both linear and exponential permeability fields, identical to the one for the uniform case. Finally, we observe a late transient period followed by the boundary-dominated state; these two periods have a discernible signature depending on the permeability distribution and the dimensionless threshold permeability. The resulting response could be complex because these regimes may overlap in time.

2.3. Field example

We present one case from a gas well in the Barnett shale. The data correspond to a horizontal well, with multiple fracture stages. We outline the methodology to analyze the field data as follows:

- Determine the product $x_f\sqrt{k^0}$ by using conventional methods (Wattenbarger et al., 1998): the Cartesian slope of $1/q_g$ versus $\sqrt{t}$ plot and Eq. 2.1.

- Estimate an initial value of k^0 using the value of x_f coming from external sources or type curve matching.
- Set a stabilized value of $1/q_g$ by following the trend at short times. This value and the maximum induced permeability lead to the estimation of the skin factor (Eq. 2.2).
- Determine the threshold permeability using the type curve matching of the late-transient time data. Then, tune the estimations by matching the overall production history using an optimization algorithm. The last step can modify the initial values of k^0, skin factor and k_D* slightly (x_f can also be included in the optimization process). Data analysis beyond the transient linear flow enables overcoming the nonuniqueness of the problem. The final set of parameters obtained with the regression analysis should be compared with the estimations using the basic type curve matching.

In the last step (optimization procedure), we assume known values of half-length of SRV element (y*) and fracture half length ($x_f = x_e /2$). In the Barnett Shale, fracturing technology and well-spacing have mutually evolved into a mature and balanced state and hence the parameter y* can be estimated taking half the distance between adjacent planes of hydraulic fractures and x_f can be taken as half distance between horizontal wells. In fields with less history, the integration of information from other sources (e.g., 2-phase flow-back data, calibrated fracture modeling, pressure transient testing, numerical

reservoir modeling, and microseismic fracture mapping) is crucial for reducing the number of unknown parameters and mitigating nonuniqueness issues in PDA.

The selection of the permeability distribution (exponential, linear, power-law, or any other function) can be done by observing the signatures of the production data trend if there is no additional information suggesting a particular function. The distribution chosen is crucial because, together with the stimulation ratio, they describe the quality of the stimulated reservoir. If the production data are the only source of information, x_f can be estimated using type curves similar to Figs. 2.2A and 2.3A. This type curve matching provides initial values of k^0 and x_f, from the X-axis and Y-axis matches, respectively:

$$k^0 = \frac{(\phi\mu c_t)_i y^{*2}}{0.006328} \frac{\left(t_D/y_D^{*2}\right)_M}{(t)_M} \quad \text{.....(2.3)}$$

$$x_f = \frac{1423 T y^*}{n_{HF} k^0 h[m(p_i) - m(p_{wf})]} \frac{(q_g)_M}{(y_D^* q_{wD})_M} \quad \text{.....(2.4)}$$

The parameter k_D* is also estimated from the corresponding k_D*-curve that best fits the late transient and/or BDS data.

Table 2.1 lists the general data for the analysis of Well 5. This well, from Barnett shale, belongs to a set of gas wells located in Tarrant and Johnson Counties, Texas, USA. **Fig. 2.7** shows the actual data from Well 5. The influence of the skin factor is apparent at

short times, and then the linear flow is evident by showing a half-slope line. This half slope spans apparently from 60 days to 600 days (Fig. 2.7A). Fig. 2.7B shows the match obtained with the three models (exponential, linear, and uniform permeability). The exponential case is a more realistic option because it matches the overall trend of the production history. The parameter estimation was performed using the Levenberg-Marquardt algorithm (Marquardt 1963) by minimizing the sum of squares of the differences between the actual data and the model. The estimation of the stimulation ratio is feasible in this example because Well 5 has data beyond the transient linear period.

Table 2.1—Well, gas, and reservoir data. Well 5	
h, ft	306
ϕ, fraction	0.048
c_{ti} , psi^{-1}	2.51 x 10^{-4}
B_{gi} , RB/Mscf	0.916
μ_i , cp	0.018
p_i , psia	3115
p_{wf} , psia	500
$m(p_i)$, psi^2/cp	6.83 x 10^8
$m(p_{wf})$, psi^2/cp	2.08 x 10^7
T, °R	633.5
x_f , ft	400
y^*, ft	552
No. stages	3

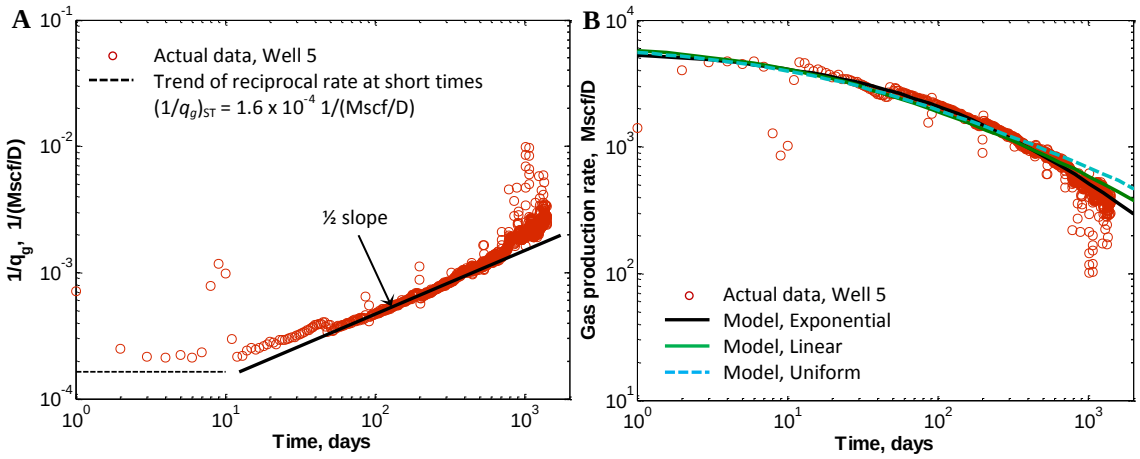

Fig. 2.7—Exponential permeability field provides a better match for Well 5.

Next, we describe the details for the characterization of the permeability distribution with the suggested procedure. For Well 5, the Cartesian slope of $1/q_g$ versus $\sqrt{t}$ is m_c = 4.5x10^{-5} (D/Mscf)/day$^{0.5}$. If we consider the number of main hydraulic fracture planes equal to the number of stages (n_{HF} = 3), then after substituting all the input data from Table 2.1 in field units:

$$k^0_{initial} = \left(\frac{315.1\,T}{n_{HF} x_f h \sqrt{(\phi \mu c_t)_i}\,[m(p_i) - m(p_{wf})]} \frac{1}{m_c} \right)^2 = 1.53x10^{-3}\ md \quad \text{.....(2.5)}$$

The stabilization level at short times of reciprocal rate versus time is $(1/q_g)_{ST}$ = 1.6x10^{-4} D/Mscf. We take a lower stabilization level than the one shown by the actual data because the initial production rates are not only affected by the skin factor, but also by a varying flowing bottomhole pressure, according to field data. Thus, the skin factor predicted by the actual stabilization level represents a maximum value (it could be

smaller). The investigation on how the varying wellbore pressure affects the well performance at short times is presented in sections 3 and 4. Substituting the input data (Table 2.1) in field units:

$$s_{initial} = \frac{n_{HF} k^0_{initial} h[m(p_i) - m(p_{wf})]}{1423T} \left(\frac{1}{q_g}\right)_{ST} = 0.166 \quad \text{.....(2.6)}$$

These are the initial estimations of k^0 and skin factor for the uniform permeability model. Then these values are refined by using an optimization algorithm (Marquardt 1963). A similar procedure is followed for exponential and linear permeability field, where the determination of dimensionless threshold permeability is achieved using the optimization algorithm. The final results are shown in **Fig. 2.8.** We note that, for a given x_f (input data in these examples) the 20-years estimated ultimate recovery (EUR_{20yr}) is affected by the long-time behavior controlled by the stimulation ratio. The 3D view in Fig. 2.8 illustrates that the new approach is an idealized description of the complex fracture network generated in massively stimulated reservoirs, but it is consistent with the observation of more permeability enhancement near the main hydraulic fracture plane. If the maximum permeability estimated in each case (exponential, linear, and uniform) is similar, then the uniform case might over predict the cumulative production, provided that the actual permeability deteriorates as the distance to the hydraulic fracture increases.

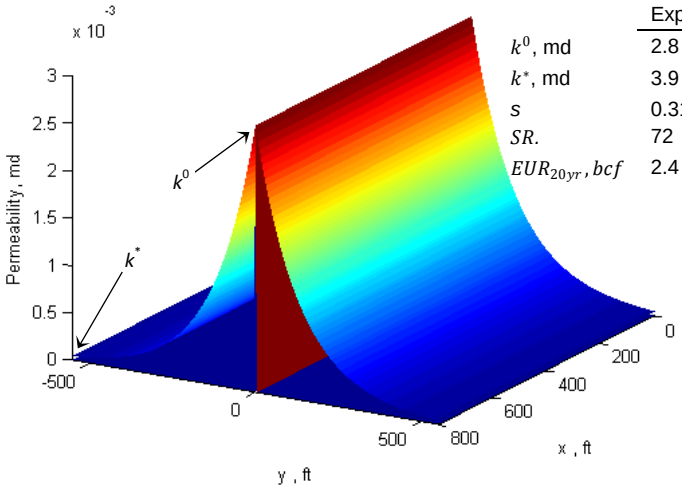

	Exponential	Linear	Uniform
k^0, md	2.8 x 10^{-3}	1.5 x 10^{-3}	1.5 x 10^{-3}
k^*, md	3.9 x 10^{-5}	3.4 x 10^{-5}	1.5 x 10^{-3}
s	0.31	0.15	0.16
$SR.$	72	45	1
EUR_{20yr}, bcf	2.4	2.7	3.0

Fig. 2.8—SRV element in Well 5. The permeability decreases from the highest stimulated value near the fracture face (2.8 x 10^{-3} md) to the threshold permeability at the boundary of the SRV element (3.9 x 10^{-5} md). The distribution corresponds to an exponential function.

The estimation of the maximum and minimum induced permeabilities – if possible – is crucial. Only the knowledge of both can grasp the two important aspects of completion efficiency in unconventional formations: the extent of the stimulated reservoir volume and the intensity of the stimulation within. If the minimum induced permeability is small, the fracture design failed in effectively stimulating the affected volume. If the ratio of the maximum to minimum induced permeabilities is small, it is suspected that the fracture design preferred SRV extension to fracture complexity (Fisher et al. 2005). Thus, the stimulation ratio may be the key to capture this latter aspect. The suggested model (already in its simplest form) may allow production analysis to independently confirm (or negate) the intuitive concepts of SRV size and fracture (network) complexity, originated from microseismic observations (Mayerhofer et al. 2010).

The field data analysis confirms that we can use exponential or linear functions to simulate the permeability field under real conditions. Further efforts need to be done to account for changing viscosity and compressibility effects (Nobakht and Clarkson 2012) in the presence of skin factor. In this work, we focus on the fundamental features of the new model. The key parameters, maximum and minimum induced permeabilities (and as a consequence the stimulation ratio), should be estimated under dynamic conditions; production data represent a substantial (albeit far from ideal) source of information to achieve this goal. The ability of assessing the effectiveness of a fracturing treatment by using induced-permeability-field models is a significant benefit of the proposed approach.

3. THE INDUCED PERMEABILITY FIELD – DOUBLE POROSITY *

3.1. Introduction

Hydraulic fracturing technique in horizontal wells is the common stimulation and completion method to produce shale gas reservoirs. The economic viability of these unconventional reservoirs strongly relies on the permeability enhancement of the natural and induced fracture system. The concept of *induced permeability field* can be used to analyze the behavior of production data of such multi-fractured horizontal wells (section 2). In this work, the concept is extended to represent the complex structure of the stimulated reservoir volume in a dual porosity/dual permeability idealization. In the new model, we treat natural fractures previously existing but possibly enhanced by the intensive fracturing operation together with the induced fractures developed during the treatment. They are considered as the dominant conduit of fluid from the reservoir to the main hydraulic fractures (HFs). We use the terminology *fracture* to describe this secondary porosity system.

---

*Reprinted with permission from Fuentes-Cruz, G., Gildin, E., and Valkó, P.P. 2014. On the Analysis of Production Data: Practical Approaches for Hydraulically Fractured Wells in Unconventional Reservoirs. *Journal of Petroleum Science and Engineering* **119** (0): 54-68. http://dx.doi.org/10.1016/j.petrol.2014.04.012. Copyright [2014] by Elsevier.

The primary porosity system is called *matrix*, it has a constant and small permeability throughout the reservoir and acts as a source of fluid to the fractures. In this model, we do not go to the details of the mechanisms, how this is achieved but remark that the matrix permeability can actually represent a wealth of transport phenomena (Akkutlu and Fathi 2012). Thus, the composite system consisting of primary and secondary porosities can be modeled using the conventional idealizations for naturally fractured reservoirs (Barenblatt et al. 1960; Warren and Root 1963; Kazemi 1969; de Swaan 1976). We use *naturally fractured reservoir* (NFR) or *fractured reservoir* (FR) to refer to the composite system. The FR is connected to the wellbore through the main hydraulic fracture (HF) planes.

In general, natural fractures are folded, bedding-parallel, and planar sub-vertical systems. Based on the analysis of cores and outcrops in the Barnett Shale (north-central Texas), the Woodford Formation (west Texas) and the New Albany Shale (the Illinois Basin), Gale and Holder (2010) suggest that the calcite-sealed sub-vertical fractures, representing the most common type of natural fracture in many reservoirs, may reactivate during the hydraulic fracturing operation because those fractures represent weak planes. They contend that sealed bedding-parallel fractures are of secondary importance because these fractures are typically less abundant than sub-vertical fractures. This observation is important because the original models used to represent NFRs assume bedding-parallel natural fractures (Kazemi 1969; de Swaan 1976). Even when the mathematical formulation for vertical and horizontal orientation is similar (in

the case gravity effects are ignored), the connection between the intrinsic medium properties and the bulk model parameters – as well as the expected range of the bulk parameters – can be greatly affected by the geometry and orientation provided by the geology and petrophysics.

The fundamental assumption in the new approach is that the permeability of the secondary system is non-uniform: as the distance to the HF increases, the permeability deteriorates because the fracture treatment energy dissipates through the fractures normal to the main HF plane. Thus, the failure of weak planes (sealed natural fractures reactivated during the HF treatment) leads to a permeability distribution depending on the distance to the HF, such that the permeability profile follows an exponential or linear function; this is the induced permeability field concept applied to a dual porosity framework.

In this work, we investigate how the induced permeability field, in addition to the parameters related to the double porosity model, controls the performance of wells producing in massively stimulated shale reservoirs. To strengthen the diagnostics based on conventional plots (production rate versus time, production rate versus cumulative production, etc.), we introduce a dimensionless group ($q_w t/G_p = q_{wD} t_D/G_{pD}$) that enables identifying the characteristic signatures of flow regimes in a suitable fashion. The dimensionless group can be interpreted as the ratio between the actual time and the material balance time (Blasingame et al. 1991); these two times are computed from the

same constant wellbore pressure (CWP) solution, implying that the $q_w t/G_p$ group has physical meaning during the transient period and the boundary-dominated state (BDS).

We suggest the new format, given by $q_w t/G_p$ versus logarithm of time or $q_w t/G_p$ versus cumulative production, because it is sensitive to any factor distorting the transient linear or bilinear flow, such as varying wellbore flowing pressure, skin factor effect, and reservoir heterogeneities. We show that the dimensionless group can lead to signatures that might not be evident in the conventional plots.

We also investigate the consequences of the varying bottomhole flowing pressure at early time, a problem almost always distorting data compared to idealized CWP solutions. The CWP inner boundary condition has been used for decades in well modeling, production data analysis, and performance prediction (Hurst 1934; van Everdingen and Hurst 1949; Fetkovich 1980). An inventory of current practices in production data analysis (PDA) is summarized by Clarkson (2013). The common signature of production rate models at CWP with no skin factor is a decreasing trend at short times, irrespective of the reservoir model; the empirical model family of Arps (1944) exhibit similar behavior. In essence, both the analytical and empirical standpoints focus on the reservoir-dominated response. Nevertheless, actual production behavior often shows some increasing trend, because of several possible reasons including fracture cleanup, facilities limitation, and bottomhole flowing pressure variation. We

show how to interpret this *distortion* in terms of a single additional parameter characterizing the stabilization process of the bottomhole pressure.

The analytical solutions with decaying wellbore pressure (DWP) reveal that half-, three-fourths-, and unit-slope straight lines can be present in the increasing part of the production rate at short times. These flow regimes allow us improving the analysis of production data. While it is well-known that the standard CWP solutions can be extended straightforwardly into DWP solutions by using the convolution theorem, the actual consequences will depend on the reservoir model and are far from trivial.

In summary, our practical approach provides two contributions: 1) relaxing the uniform or constant assumption on key parameters, such as fracture permeability and wellbore pressure; and 2) providing alternative tools for diagnostics and analysis, relying on minimum data requirement (production rate, cumulative production, time, and dimensionless group $q_w t/G_p$).

3.2. Nonuniform induced permeability field in fractured reservoirs

The new model is an extension of the induced permeability field concept to the dual porosity idealization, considering transient fluid transfer from matrix to fractures (Kazemi 1969; de Swaan 1976); the pseudosteady fluid transfer (Barenblatt et al. 1960; Warren and Root 1963) can be handled straightforwardly. We consider constant matrix properties and distance-dependent permeability of the natural fractures reactivated

and/or generated by the intensive stimulation. Appendix B presents the mathematical model and solutions in Laplace space as well as closed form analytical approximations in the time domain.

3.2.1. Model description

Fig. 3.1 depicts a hydraulically fractured well producing in a FR. The bulk matrix permeability ($\hat{k}_m$) is constant, and the bulk fracture permeability distribution [$\hat{k}_f(y)$] is a consequence of the fracturing operation as well as the HF itself. The highest induced permeability ($\hat{k}_f^0$) is near each main HF plane (at y=0) and the permeability decreases (following an exponential or linear profile) as the distance to the HF plane increases. The minimum bulk permeability value (called here the *threshold permeability*, $\hat{k}_f^*$), is reached at the boundary of the SRV element (at $y=y^*$ and $y=-y^*$).

We assume that the SRV can be divided into n_{HF} identical elements, such that the total production rate (q_w) is equal to n_{HF} times the production rate coming out the SRV element. Additionally, we assume that there is neither interference between adjacent wellbores nor significant production beyond the SRV because the contribution of the non-induced region is negligible (Mayerhofer et al. 2006; Ozkan et al. 2011). We notice that other definitions of SRV are also possible, but in this work we use it synonym to the drainable volume.

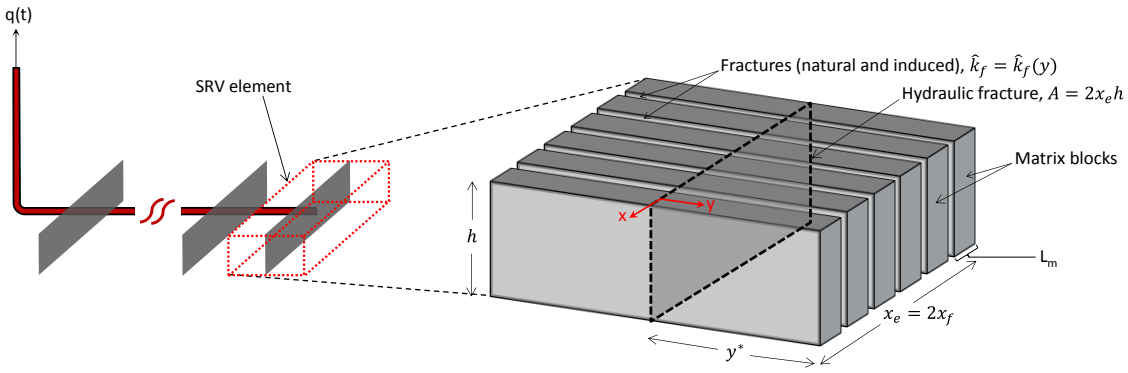

Fig. 3.1—New model for massively stimulated FRs. The non-uniform permeability distribution of the natural and induced fractures depends on the distance to the main HF plane.

The SRV element has a rectangular shape with length $2y^*$, width x_e, and thickness h. The infinite conductivity HF, located at the middle of the SRV element, fully penetrates the reservoir in both height (h) and lateral extent (x_e) such that the HF length ($2x_f$) is equal to the lateral extent of the reservoir ($2x_f = x_e$).

We use the bulk properties to represent the characteristics of the matrix blocks and fractures. The definition of a bulk property ($\hat{\xi}$) in terms of the intrinsic property (ξ) of a medium j (j=matrix or fracture) is $\hat{\xi}_j = \xi_j V_{jt}/V_B$, where V_{jt} is the total volume occupied by the medium j and V_B is the bulk volume of the total system (Brown et al. 2011). If the natural fractures are assumed to be vertical planes as shown in Fig. 3.1 (matrix blocks are vertical slabs), then the bulk property is $\hat{\xi}_j = \xi_j L_{jt}/x_e$, where L_{jt} is the sum of the widths of medium j in the x direction. If we depict the fractures and matrix slabs oriented horizontally (Kazemi 1969; de Swaan 1976), then the bulk property is $\hat{\xi}_{jh} = \xi_j h_{jt}/h$ where h_{jt} is the sum of the widths of medium j in the vertical direction. Either

viewpoint (vertical or horizontal fractures) leads to similar mathematical model. Nevertheless, the vertical fracture orientation is a more consistent conceptualization based on the evidence of cores and outcrops studies, at least in some shale plays (Gale and Holder 2010, Lorenz et al. 2002).

The natural fractures are assumed uniformly distributed through the total bulk volume, such that we can conveniently define a volumetric, areal, or linear fracture density. In the geometry shown in Fig. 3.1, the linear fracture density is $\rho_f = n_f/x_e$ (or $\rho_{fh} = n_f/h$ for horizontal fractures), where n_f represents the total number of fractures in the bulk volume (SRV element). For example, the bulk fracture permeability can be written as $\hat{k}_f = k_f L_{ft}/x_e = k_f \rho_f L_f$, where L_f is the fracture width.

As we can obtain a given bulk property value from different combinations of intrinsic properties that depend on the reservoir characteristics under study, we summarize the equations and results of this work in terms of bulk properties. Moreover, we can compare the results with the pseudosteady-fluid-transfer idealization (Warren and Root 1963) straightforwardly.

3.2.2. Production behavior at constant wellbore pressure

In one-porosity systems, the transient linear flow at short and intermediate times corresponding to exponential and linear permeability fields is the same as the uniform case, provided that the maximum induced permeability is the same in all three

distributions (section 2). In this section, we obtained a similar result for FRs: irrespective of the permeability distribution (exponential or linear) the transient linear flow in the fractures behaves as uniform. In other words, the maximum induced permeability supersedes the constant permeability of the uniform model during the transient linear flow in the fractures. We briefly discuss these results for completeness. If we assume zero skin factor, CWP, and transient linear flow in the fractures, then the short-time approximation of production rate in dimensionless and real variables is:

$$q_{wlD-STA} = \frac{2\sqrt{\omega}}{\pi^{3/2}\sqrt{t_D}} \quad \text{(3.1a)}$$

$$q_{wl-STA} = \frac{2T_{sc}}{\sqrt{\pi}p_{sc}} \frac{n_{HF}h\sqrt{\widehat{\phi_{fi}c_{tfi}}\mu_i}[m(p_i)-m(p_{wf})]}{T} \frac{x_f\sqrt{\hat{k}_f^0}}{\sqrt{t}} \quad \text{(3.1b)}$$

As expected, the production response depends only on the fracture properties. Assuming zero skin factor, CWP, and bilinear flow (transient linear flow in the fractures and matrix blocks), the short-time behavior in dimensionless and real variables is given by:

$$q_{wbD-STA} = \frac{2\sqrt[4]{\lambda(1-\omega)}}{\sqrt[4]{3}\pi\Gamma(3/4)\sqrt[4]{t_D}} \quad \text{(3.2a)}$$

$$q_{wb-STA} = \frac{2\sqrt{2}T_{sc}}{\Gamma(3/4)p_{sc}} \frac{n_{HF}h[m(p_i)-m(p_{wf})]x_f}{T} \sqrt{\frac{\hat{k}_f^0}{L_m}} \left[\frac{t}{\mu_i\hat{k}_m\widehat{\phi_{mi}c_{tmi}}}\right]^{-1/4} \quad \text{(3.2b)}$$

Where *Γ(x)* is the Gamma function. In this flow regime, the fracture and matrix properties control the well performance simultaneously. If there is linear flow as a result of interporosity flow from matrix blocks into the fractures (transient interporosity flow), then the intermediate-time approximation is (no skin factor, CWP):

$$q_{wlD-ITA} = \frac{2y_D^*\sqrt{\lambda(1-\omega)}}{\sqrt{3}\pi^{3/2}\sqrt{t_D}} \quad \text{(3.3a)}$$

$$q_{wl-ITA} = \frac{4T_{sc}}{\sqrt{\pi}p_{sc}} \frac{n_{HF}hy^*[m(p_i)-m(p_{wf})]\sqrt{\mu_i\phi_{mi}\widehat{c_{tmi}}}}{TL_m} \frac{x_f\sqrt{\hat{k}_m}}{\sqrt{t}} \quad \text{(3.3b)}$$

In this case, the matrix transient flow is dominant, leading to the dependence on the matrix properties. We can safely assume that there is a certain component of the total drawdown that is proportional to the well rate. In other words, there is always a positive skin factor, even if it is small by magnitude. In the presence of skin factor, CWP, and linear or bilinear flow in the reservoir, the production rate flattens at short times:

$$q_{wDs-STA} = \frac{1}{s} \quad \text{(3.4a)}$$

$$q_{ws-STA} = \frac{\pi T_{sc}}{p_{sc}} \frac{n_{HF}\hat{k}_f^0 h}{T} \frac{[m(p_i)-m(p_{wf})]}{s} \quad \text{(3.4b)}$$

According to Eq. 3.4b, the production rate is controlled by fracture properties, even in the case of transient bilinear flow in the reservoir that already implies the interaction of the fracture and matrix systems (Eqs. 3.2a and 3.2b). Eqs. 3.4a and 3.4b provide a maximum value of skin factor in real situations because (as we will show in the next subsection) the flattening is also affected by the abrupt change in the flowing bottomhole pressure at short times.

Fig. 3.2 shows the well performance of a well producing in a FR for different values of interporosity flow coefficient (λ). In Fig. 3.2A, we note that Eqs. 3.1a, 3.2a, and 3.3a accurately predict the production behavior depending on the combination of ω and λ; these approximations are similar to those for uniform permeability field (Bello and Wattenbarger 2010).

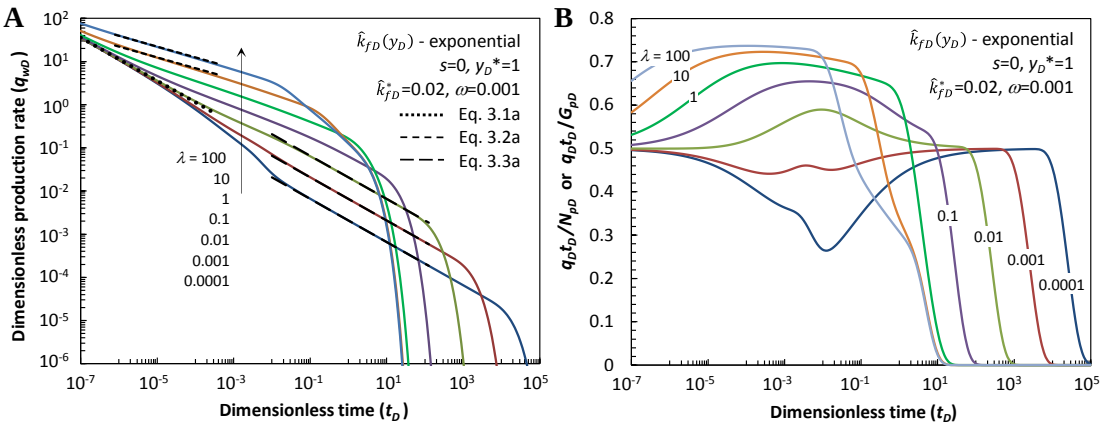

Fig. 3.2—The interporosity flow coefficient (λ) strongly affects the well performance. The dimensionless group $q_w t/N_p$ is equal to 0.75 during the bilinear flow.

According to Eqs. 3.1 through 3.3, the linear and bilinear flow yield to stabilization levels equal to 1/2 and 3/4 in the $q_w t/G_p$ group, respectively, which is verified in Fig. 3.2B, where distinctive signatures are identified depending on the combination of the reservoir parameters. In general, the empirically often-diagnosed transient linear flow is distorted by the fluid transfer between matrix blocks and natural fractures. The departure from the transient linear flow is more evident in the $q_w t/G_p$ plot than in the production rate plot. For example, in Fig. 3.2A the curve corresponding to λ=0.0001 shows a -1/2 slope through 5 logarithmic cycles approximately, interpreted as linear flow; the same case shows a 1/2 stabilization only through 1.5 logarithmic cycles in Fig. 3.2B. In Fig. 3.2A the transition from the transient linear flow in the fractures to the transient interporosity flow might not be evident in the curves corresponding to λ=0.001 and λ=0.01; while the same cases show a minimum and a maximum during the transition in Fig. 3.2B respectively, enabling a clear identification of the transition.

Fig. 3.3 shows a sensitivity analysis of the parameter ω from 0 (negligible storage capacity in the natural fractures) to 1 (homogeneous fracture porosity). Eqs. 3.1a and 3.3a accurately predict the production rate behavior depending on the combination of ω and λ (Fig. 3.3A). The dimensionless group $q_w t/G_p$ shows a complex behavior because the uniform decreasing trend observed in homogeneous systems (ω=1) is distorted in such a way that the curves bend up and down. This behavior is not evident in the popular q_w versus time plot; thus, we suggest using the dimensionless group as an additional diagnostic tool when analyzing field data.

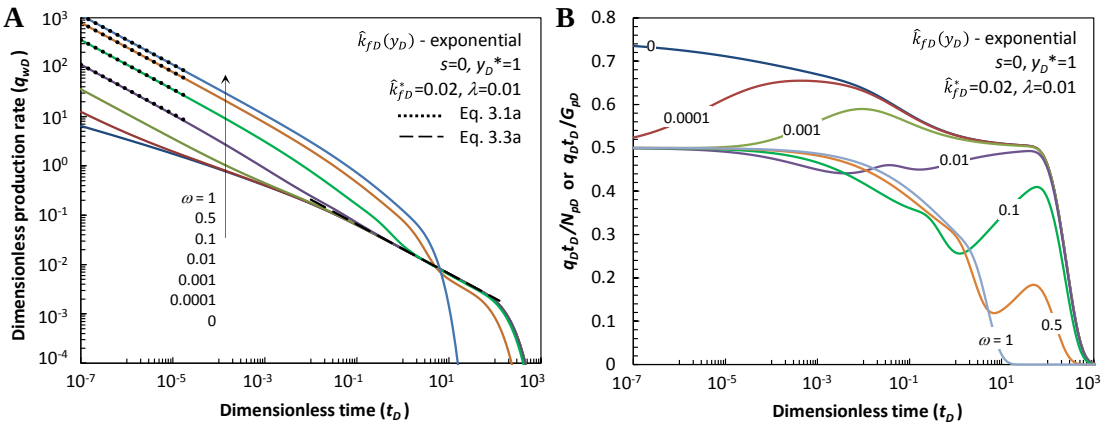

Fig. 3.3—The production rate and $q_w t/N_p$ group decrease uniformly for the homogeneous case (ω=1). In FRs, the $q_w t/N_p$ group bends up and down depending on the value of ω and λ.

Eqs. 3.1 through 3.3 do not involve the parameter $\hat{k}^*_{fD}$. As these equations are the same as in the uniform case (Bello and Wattenbarger 2010), it is reasonable to ask: what are the differences between nonuniform and uniform formulation in FRs? To answer this question we obtained the well performance by varying the parameter $\hat{k}^*_{fD}$ (**Figs. 3.4 and 3.5**). We found that if λ is small (Figs. 3.4A and 3.5A), then the dimensionless threshold permeability controls the transition between the early transient linear flow (Eqs. 3.1a and 3.1b) and the interporosity linear flow (Eqs. 3.3a and 3.3b). Thus, in the late stage of production data, the initial volume of the fractures is utterly depleted and the induced permeability field does not have a particular signature in the production performance.

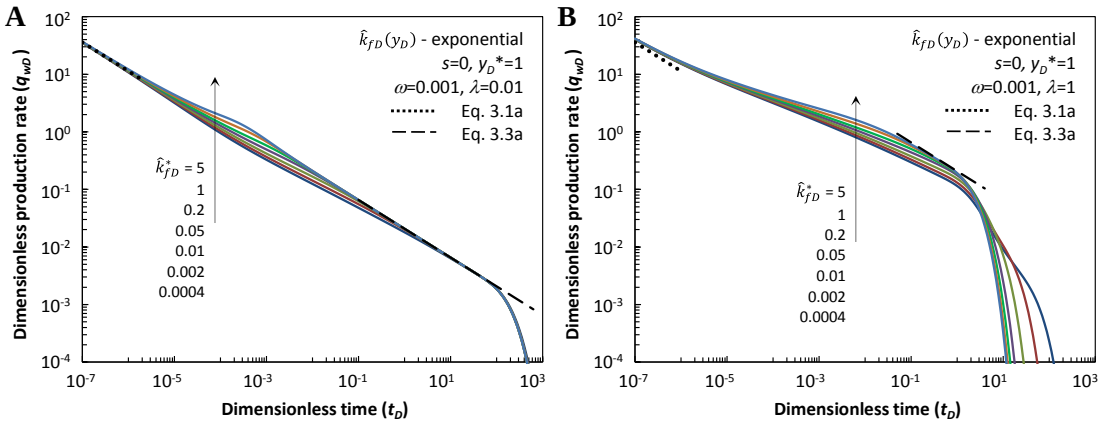

Fig. 3.4—If λ is small, then k_D* controls the transition between the transient linear flow in the fractures and the interporosity linear flow. If λ is large, then k_D* controls the late-transient period and BDS.

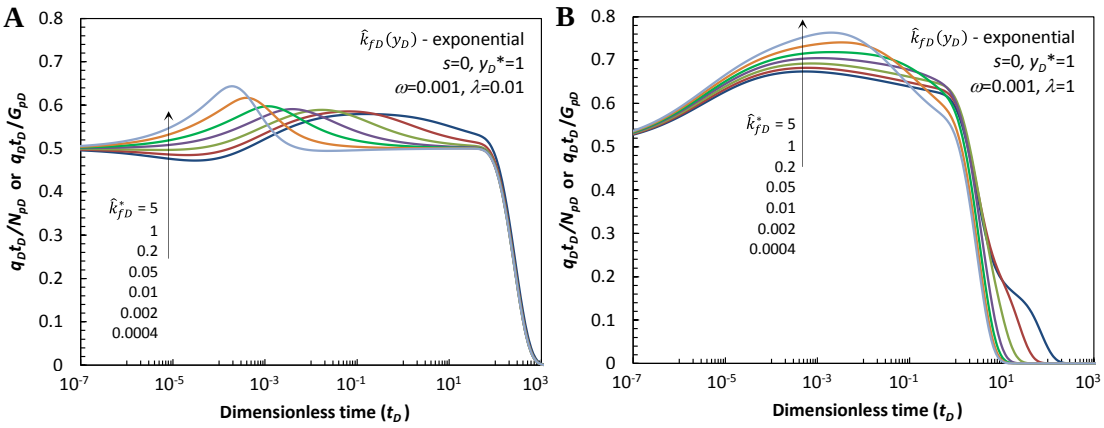

Fig. 3.5—The 0.5 (linear flow) and 0.75 (bilinear flow) stabilizations are altered because of the interporosity flow between matrix blocks and fractures.

If λ is large (Figs. 3.4B and 3.5B), then the dimensionless threshold permeability controls the late-transient period and BDS. In this situation, the fluid transfer from matrix to fractures is favorable and it develops earlier and faster such that the natural fractures deplete, or partially deplete, during the not so long feeding period. As a result,

$\hat{k}_{fD}^{*}$ has a strong impact on the late time behavior of the well performance; this is consistent with the one-porosity findings because the double porosity model converges to the homogeneous system as $\lambda \rightarrow \infty$ (Warren and Root 1963).

In Fig. 3.4, we show six and ten logarithmic cycles in the vertical and horizontal axis respectively, to explain the physics of the model. The departure from the uniform case might not look so significant when λ is small. Nevertheless, field data usually have two or three logarithmic cycles in the vertical direction such that the departure can be significant when plotting in real situations.

The diagnostic plots shown in Fig. 3.5 can be generated using field data in a direct manner because they involve the basic information available in the databases of all oil and gas companies. The dimensionless group calculated with field data can be compared directly to the type curves from simulated data allowing the analyst to have a quick judge not only on the flow regime itself, but also on the departure from it, a difficult task on the typical log-log plot of production rate versus time. The group $q_w t/G_p$ is also useful to identify the skin factor and the varying wellbore pressure effects as it is shown in the next subsection.

3.2.3. Production behavior at decaying wellbore pressure

As noted before, the production behavior from field data shows an increasing trend at the initial stage of production that might originate from the time span taken by the

bottomhole flowing pressure to reach the stabilized value. We can build a suitable wellbore pressure function with an initial value equal to the initial reservoir pressure, having an abrupt pressure change at short times, and reaching the stabilized value ($p_{wf,stab}$) after a time span controlled by the mean halftime (τ) of the decaying function. As a consequence, the zero-time production rate is equal to zero, having an increasing behavior at short times and after reaching a maximum value, the common decline trend is exhibited (**Fig. 3.6**); this novel viewpoint is more consistent than assuming a stabilized flowing pressure since the start of production. We can use any appropriate function to correlate the actual bottomhole flowing pressure, provided that its Laplace transform exists to apply the Convolution theorem straightforwardly (van Everdingen and Hurst 1949) as shown in Appendix C. To the best of our knowledge, this is the first time the varying character of the wellbore pressure is handled in this direction.

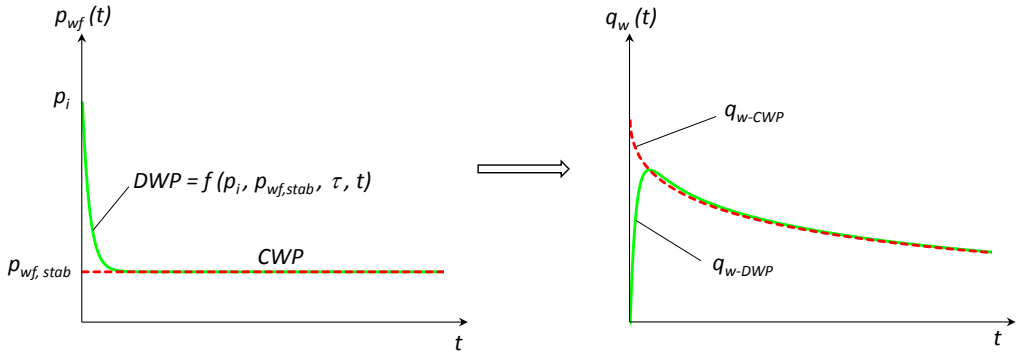

Fig. 3.6—Field data exhibit an abrupt wellbore pressure change at short times that strongly influences the well performance during the initial production stage.

If we assume zero skin factor, DWP, and transient linear flow in the fractures, then the short-time approximation of production rate in dimensionless and real variables is:

$$q_{wlD\tau-STA} = \frac{4\sqrt{\omega}\sqrt{t_D}}{\pi^{3/2}\tau_D} \quad \text{.....(3.5a)}$$

$$q_{wl\tau-STA} = \frac{4T_{sc}}{\sqrt{\pi}p_{sc}} \frac{n_{HF}h\sqrt{\widehat{\phi_{fi}c_{tfi}}\mu_i}[m(p_i)-m(p_{wf})]}{T\tau\mu_i} x_f\sqrt{\hat{k}_f^0 t} \quad \text{.....(3.5b)}$$

Eqs. 3.5a and 3.5b indicate a positive half-slope straight line on the log-log plot of production rate versus time, revealing a new flow regime that results from the combination of transient linear flow in the reservoir and the sharp change in the bottomhole flowing pressure at short times. The product $x_f\sqrt{\hat{k}_f^0}$ can be determined by using the equation for transient linear flow in the reservoir (Eq. 3.1b). In case of high quality production and simultaneous bottomhole flowing pressure data, the parameter λ could be calculated with certainty and then we could estimate the HF half-length by using the slope of equation 3.5b. Unfortunately, short-time production data usually have low quality. Additionally, flowing pressures are not actually measured in most of the cases; they are estimated from surface measurements relying on empirical or mechanistic models.

Assuming zero skin factor, DWP, and bilinear flow in the reservoir, the short-time behavior of production rate is given by:

$$q_{wbD\tau-STA} = \frac{8\sqrt[4]{\lambda(1-\omega)}t_D{}^{3/4}}{3\sqrt[4]{3}\pi\Gamma(3/4)\tau_D} \quad \text{(3.6a)}$$

$$q_{wb\tau-STA} = \frac{2\sqrt{2}T_{sc}}{\Gamma(7/4)p_{sc}} \frac{n_{HF}h[m(p_i)-m(p_{wf})]x_f}{\tau T} \sqrt{\frac{\hat{k}_f^0}{L_m}} \sqrt[4]{\frac{\hat{k}_m\widehat{\phi_{mi}c_{tmi}}}{\mu_i}} t^{3/4} \quad \text{(3.6b)}$$

The product $x_f\sqrt{\hat{k}_f^0}$ also appears in the previous equation, and it can be determined from the transient linear flow (Eq. 3.1b) leading to the possibility to estimate the matrix permeability by using Eq. 3.6b if production rate and bottomhole pressure had high quality at short times. Including skin factor, the DWP approximation at short times is (linear or bilinear flow in the reservoir):

$$q_{wDs\tau-STA} = \frac{t_D}{s\,\tau_D} \quad \text{(3.7a)}$$

$$q_{ws\tau-STA} = \frac{\pi T_{sc}}{s\,p_{sc}} \frac{n_{HF}\hat{k}_f^0 h[m(p_i)-m(p_{wf})]t}{T\tau} \quad \text{(3.7b)}$$

Thus, unit-slope straight line is also present irrespective of the flow regime in the reservoir (linear or bilinear). In general, Eqs. 3.5 through 3.7 reveal that, during the increasing trend of production data, the well performance depends on the flow regime in

the reservoir, fluid properties, HF dimensions, fracture and/or matrix properties, the skin factor, as well as on the wellbore dynamics represented by the varying wellbore pressure.

Under CWP conditions, the short- and intermediate-term behavior in FRs leads to linear or bilinear flow characterized by -1/2 and -1/4 slopes in the log-log plot of production rate versus time. The skin factor effect leads to a flattening in production rate equal to the reciprocal skin factor in dimensionless form (Bello 2009). The inclusion of DWP gives rise to additional flow regimes during the initial increasing trend of production rate. This *wellbore effect*, in combination with the skin factor, is superimposed on the flow regimes in the reservoir leading to a set of new flow regimes presented in **Fig. 3.7;** each one having a distinguishable signature.

According to Fig. 3.7, the impact of the skin factor and the DWP on the production behavior is unfavorable not only because they reduce the production rate, but also because they mask the reservoir response. The DWP in production data analysis is the counterpart of the wellbore storage effect in pressure transient testing in the sense that – together with the skin factor– they can mask reservoir complexity. The parameter τ interacts with the skin effect similarly as the wellbore storage coefficient does in well-testing applications (Agarwal et al. 1970).

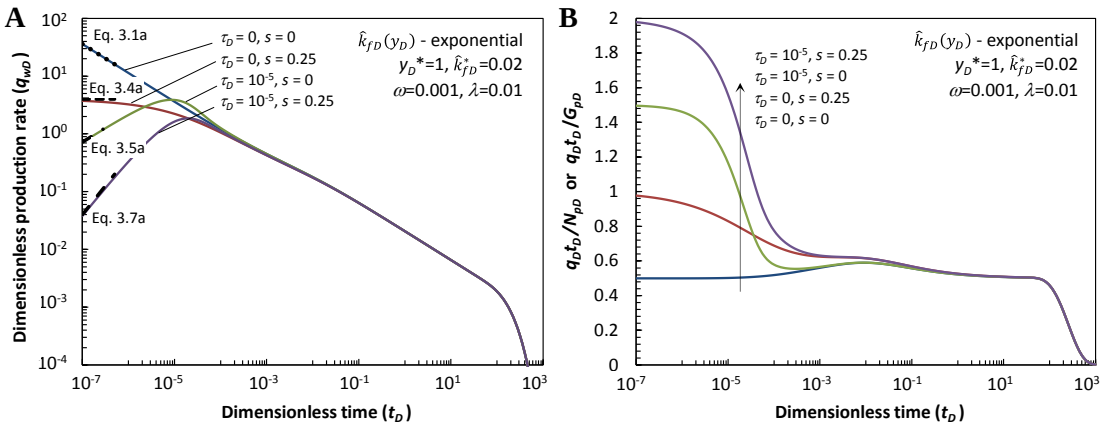

Fig. 3.7—The decaying wellbore pressure has a discernible signature at short times. The combination of the varying wellbore pressure and the skin factor masks the reservoir heterogeneities.

The traditional straight line with -1/2 slope (Eqs. 3.1a and 3.1b) corresponding to transient linear flow in the fractures turns into zero-, half-, and unit-slope straight lines (Eqs. 3.4a, 3.5a, and 3.7a) if skin factor, DWP with no skin factor, and DWP with skin factor are included into the mathematical model, respectively. This is shown in Fig. 3.7A with the dotted and dashed lines that represent the cited equations. These analytical expressions enable identifying the parameters that control the well performance in each scenario.

Similarly, the -1/4 slope (Eqs. 3.2a and 3.2b) of bilinear flow turns into zero, three-fourths, and unit slope if skin factor, DWP with no skin factor, and DWP with skin factor are included, respectively (Eqs. 3.4a, 3.6a, and 3.7a).

It is remarkable that each of these new apparent flow regimes has a characteristic stabilization level in the $q_w t / G_p$ group (**Table 3.1,** Fig. 3.7b). Thus, in addition to the typical diagnostic tools for decline curve or rate-transient analysis (in particular, the log-log plot of production rate versus time), we encourage the use of the ratio between the production time and material balance time because it enables identifying the characteristic signatures of flow regimes straightforwardly, without excessive data manipulation.

Table 3.1—New flow regimes during the early stage of production data

Mean lifetime	$\tau = 0$ (CWP)		$\tau \neq 0$ (DWP)	
Skin factor	s = 0	s > 0	s = 0	s > 0
Flow regime	Slope in log(q_w) versus log(t) plot			
Linear	-1/2	0	1/2	1
Bilinear	-1/4	0	3/4	1
	Stabilization level in ($q_w t/G_p$) plot			
Linear	1/2	1	3/2	2
Bilinear	3/4	1	7/4	2

In Table 3.1, we provide practical criteria to identify different scenarios affecting the data previous to the linear (-1/2 slope) and bilinear (-1/4 slope) flow regimes, that is, at relatively short times. These results can be extended to any flow regime. In general, transient and boundary dominated flow periods can be diagnosed using the dimensionless group, providing a useful addition to procedures relying on conventional plots.

3.3. Field example

This example was analyzed in section 2 using the single porosity formulation of the induced permeability field. The input data was presented in Table 2.1. After the effect of the varying wellbore pressure and the skin factor at short times, a -1/2 slope is observed from 60 days to 600 days approximately (**Fig. 3.8**).

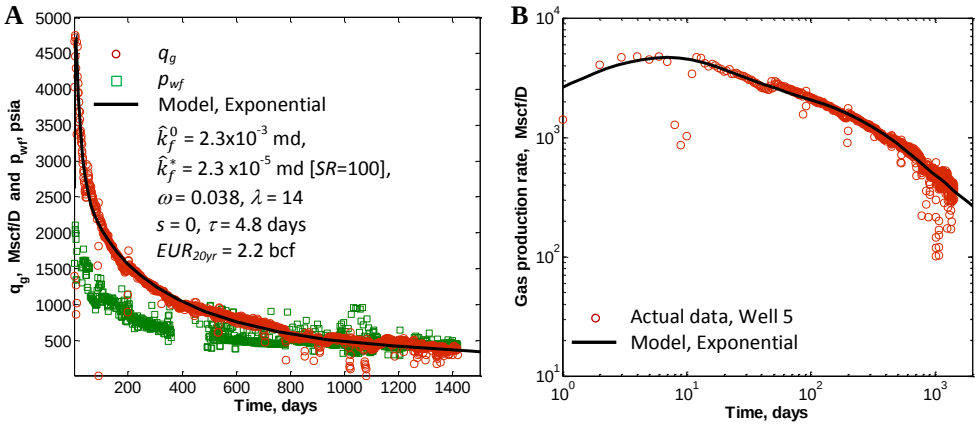

Fig. 3.8—PDA of Well 5 using DWP, NFR, and exponential permeability field. The new approach captures the increasing and decreasing trend of the production history.

The 1/2 stabilization level in the dimensionless group spans in a shorter period (**Fig. 3.9**). It never stabilizes at the 1/2 level corresponding to linear flow; this means that the production data is affected by the skin factor, the varying wellbore pressure, and the permeability deterioration such that the transient linear flow is distorted.

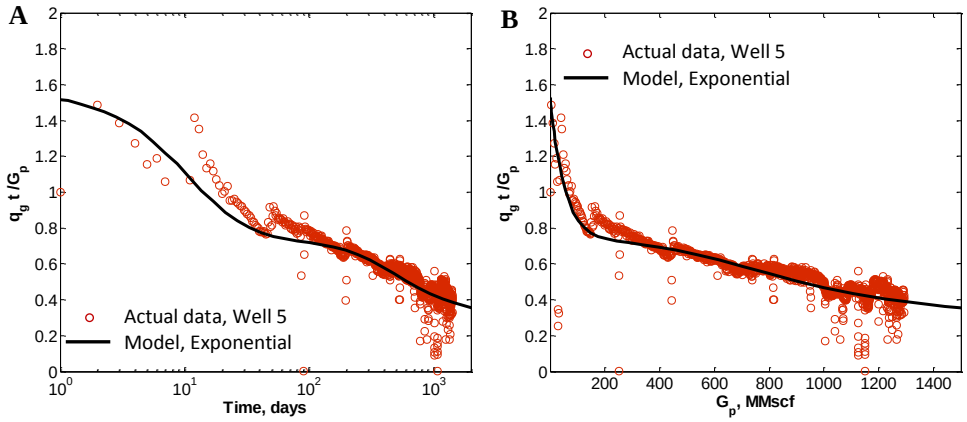

Fig. 3.9—The values between 1 and 2 in the dimensionless group suggests that the production data is affected by the variation in the bottomhole pressure and/or the skin factor.

The results obtained with the single-porosity version of the exponential permeability field are (section 2): k^0=2.8x10^{-3} md, k*=3.9x10^{-5} md (SR=72), s=0.32, and EUR_{20yr} =2.4 bcf. These results were obtained considering constant wellbore pressure. The existence of a positive skin was important to achieve an acceptable curve fit. We used the matrix block properties to evaluate the dimensionless time into the analytical model because t_D can be written in the following form:

$$t_D = \frac{\hat{k}_f^0 t}{(\gamma+1)(\hat{\phi}_m \mu c_{tm})_i x_f^2} \quad \text{.....(3.8)}$$

Where $\gamma = \left(c_{tf}/c_{tm}\right)_i \left(\hat{\phi}_f/\hat{\phi}_m\right)_i$. Thus, we can consider $\gamma << 1$ for practical purposes in Barnett shale.

In this section, we provide the analysis including the effect of the varying wellbore pressure, and fractures (natural and/or induced). We assume $\hat{k}_{fD}^{*}$=0.01 (k_D^{*}=0.014 for the single porosity model). The estimation of the remaining parameters ($\hat{k}_f^0$, ω, λ, s, τ) was performed using the Levenberg-Marquardt algorithm (Marquardt 1963). The results are also shown in Fig. 3.8. We observe a good match not only during the *reservoir dominated* stage, but also during the increasing trend at short times. The match of the increasing production stage was achieved by including the DWP approach. In general, the flattening at short times is controlled by the combined effect of the DWP and skin factor. In some situations, the DWP is enough to capture the increasing and the flattening trends; this is the case for Well 5. The mean lifetimes (τ) estimated with the model and the actual data are equal to 4.8 days and 80 days, respectively. This discrepancy might be due to errors originated by the conversion from surface measurements to bottomhole conditions. Additionally, there might be additional phenomena not captured by the converted bottomhole flowing pressure, such as fracture cleanup – and even particular company policy regarding tubing installation, choke settings, etc.

The maximum and minimum induced permeabilities are similar to those obtained with the single-porosity framework. Nevertheless, the interpretation is quite different: the estimations of this work represent the bulk fracture permeability. We can obtain the intrinsic permeability dividing by the fraction of volume occupied by the fractures into the total system (fractures + matrix blocks). The EUR_{20yr} is similar to that estimated with

single porosity, only 5% relative difference. In addition, the dual porosity parameters are consistent with the shale reservoir characteristics. These parameters can be used to calibrate reservoir modeling studies based on the geological and petrophysical characteristics of the reservoir.

Only few papers in the literature have reported the values of ω and λ in unconventional reservoirs. In Figs. 3.2 through 3.5 we show a broad range of these parameters. In real situations, the range might be constrained according to the values involved in the definition of ω and λ for a specific reservoir. The following analysis enables having a quick reference on the expected ranges of the dual porosity parameters in unconventional reservoirs. If we assume that the intrinsic fracture compressibility is α times the intrinsic matrix compressibility then, from the definition of ω (Eq. B-19):

$$\omega = \frac{\hat{\phi}_{fi}\alpha}{\hat{\phi}_{fi}\alpha+\hat{\phi}_{mi}} \quad \text{.....(3.9)}$$

Where $\alpha = c_{tfi}/c_{tmi}$. **Fig. 3.10A** shows a 3D view of ω by varying the bulk fracture porosity from 0.001 to 0.1 % and α between 1 and 10. If $\hat{\phi}_m$=5%, then minimum and maximum values of ω are 2.0x10^{-4} ($\hat{\phi}_f$=0.001%, α=1) and 0.17 ($\hat{\phi}_f$=0.1%, α=10), respectively. Any ω between these values can be realized by an infinite number of combinations of $\hat{\phi}_{fi}$ and α. We note that a different value of $\hat{\phi}_m$ shifts the plane in the vertical direction.

Fig. 3.10B shows the sensitivity analysis for λ. In this plot, the ratio $\hat{k}_m/\hat{k}_f$ varies from 1x10^{-6} to 1x10^{-3}, and L_m from 1 ft to 100 ft. The plane for a different value of x_f is shifted in the vertical direction as it is shown for x_f =200 ft. We observe that for x_f = 400 ft, the minimum and maximum values of λ are 1.9x10^{-4} ($\hat{k}_m/\hat{k}_f$=1x10^{-6}, L_m=100 ft) and 1900 ($\hat{k}_m/\hat{k}_f$=1x10^{-3}, L_m=1 ft), respectively. Therefore, for Well 5, the sets ($\hat{\phi}_f$, α) and ($\hat{k}_m/\hat{k}_f$, L_m) are constrained to the values defining the black lines in Figs. 3.10A and 3.10B, corresponding to ω=0.038 and λ=14, respectively. Additional sources, such as petrophysical, geological, and experimental (core) data need to be integrated to calibrate the results properly.

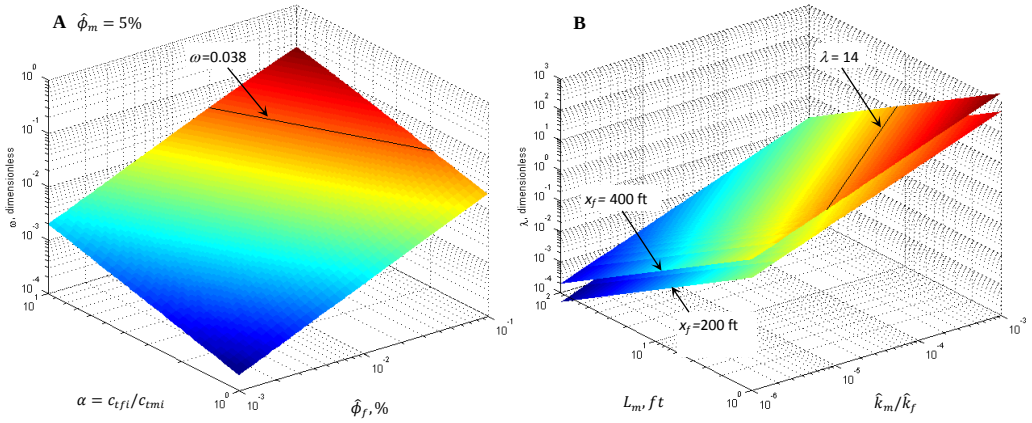

Fig. 3.10—$\omega\alpha\phi$ and λLk 3D plots. Representative ranges of ω and λ depends on the broad variation of the parameters involved in their definitions.

The dimensionless interporosity-flow coefficient is in the same order of magnitude as in conventional reservoirs with radial geometry. We can verify this by writing the parameter λ (Eq. B-28) as follows:

$$\lambda = \frac{12}{L_m^2}\frac{\hat{k}_m}{\hat{k}_f^0} r_w^2 \frac{x_f^2}{r_w^2} = \lambda_{r_w}\left(\frac{x_f}{r_w}\right)^2 \quad \text{.....(3.10)}$$

Eq. 3.10 means that $1.9x10^{-4} \leq \lambda \leq 1900$ maps into $1.1x10^{-10} \leq \lambda_{r_w} \leq 1.1x10^{-3}$ for a typical wellbore radius of 0.3 ft and x_f =400 ft. In general, the ranges of λ_{r_w} (interporosity-flow coefficient based on r_w) and ω are similar to those reported in the petroleum literature for conventional NFRs.

The large number of possible scenarios raises some concerns regarding the applicability of double porosity models for the analysis of production data without simultaneously available bottomhole flowing pressure and external sources of data. It is obvious that many combinations of the parameters can be selected, yielding to an equally acceptable description of available history. While some of the combinations will lead to basically the same production forecast as the single porosity/variable permeability model, others will significantly derail the forecast in an optimistic or pessimistic way.

Dual porosity and the associated key parameters (λ and ω) lead to a rich source of variety in the production rate behavior, but their identification from production history

alone seems to be an inherently ill-conditioned task. The exact knowledge of these parameters requires an interdisciplinary approach gathering microseismic, geology, petrophysics, and laboratory experiments, though the dual porosity formulation might not even be necessary from a production engineering viewpoint. The work of several researchers, many of them possibly from a bit different perspective and many others from a different discipline (Fisher et al. 2005; Gale and Holder 2010; Mullen 2010; Ramurthy et al. 2011), accentuates the importance of integrating information from different knowledge and contributes to the ongoing deliberation related to the effectiveness of shale gas fracturing.

It seems that the induced permeability field concept is a useful addition because it introduces only one additional parameter: $\hat{k}_f^0$, if we consider $\hat{k}_f^*$ as the old parameter inherited from uniform models, or $\hat{k}_f^*$ if we consider $\hat{k}_f^0$ as the inherited parameter. This additional parameter seems to capture the basic effect of the intensive stimulation treatment in unconventional reservoirs. The parameter assigns a numerical factor of quality to the SRV. In our opinion, it might evolve as a metric of the overall effectiveness (success) of the hydraulic fracturing treatment, complementing the obvious primary metric of *initial rate*, *first 3-month production*, etc. With a well-planned horizontal well density and careful selection of fracture placing, the extent of the SRV is basically determined, so it is not a suitable measure of the effectiveness of the completion/stimulation program, rather it is a necessary but not sufficient aspect of it. For the overall success of multi-staged horizontal fracturing the intuitively introduced,

fracture complexity (Fisher et al. 2005) is now respected more, and the ratio of $\hat{k}_f^0/\hat{k}_f^*$ (the stimulation ratio) might be the most important quantifiable effect of fracture complexity showing up in the production decline, affecting the *EUR*. It is clear that increasing $\hat{k}_f^0/\hat{k}_f^*$ will improve initial rates but will lead to faster decline, and hence this parameter may play a key role in optimization of the hydraulic fracture design.

4. THE INDUCED INTERPOROSITY FLOW FIELD *

4.1. Introduction

Multi-fractured horizontal wells have become the standard configuration to produce shale reservoirs. It is well known that the matrix blocks in shale systems have ultra-low to low permeabilities. However, the intensive hydraulic stimulation enables the economic production of hydrocarbons.

In the massively stimulated reservoir, the original geological configuration of the properties is not preserved because the fracturing treatments alter those properties in the stimulated reservoir volume (SRV). It is reasonable to expect that, after the hydraulic fracturing treatments, the characteristic size of the matrix blocks is not uniform.

---

*Reprinted with permission from Fuentes-Cruz, G. and Valkó, P.P. 2014. Revisiting the Dual Porosity–Dual Permeability Modeling of Unconventional Reservoirs: the Induced Interporosity Flow Field. Manuscript submitted to *SPE Journal*. Copyright [2014] by Society of Petroleum Engineers.

The first models for naturally fractured reservoirs assumed fixed block size (Barenblatt et al. 1960; Warren and Root 1963; Kazemi 1969). Reported extensions to multiple matrix-block sizes assume a random distribution of the matrix blocks (Cinco-Ley et al., 1985; Johns and Jalali 1991; Sharifi Haddad et al. 2012; Ranjbar et al. 2012). The common underlying idea in those models is that the representative elementary volume (REV) of the reservoir consists of matrix blocks of various sizes described by a probability density function. Recently, Torcuk et al. (2013) presented a model accounting for multiple block size and corresponding properties.

In this work, we provide a continuum approach: the equations of matrix blocks and fractures are formulated in terms of effective properties taken over an REV, inside of which the matrix blocks have the same size. Uniform matrix block size inside an REV enables considering transient interporosity flow with matrix and fractures coupled via boundary conditions on the block surfaces. According to Saphiro (1987), the REV is not measured in real life for a given field situation; the continuum hypothesis is invoked and the equations describing transport phenomena are developed by assuming that the continuum approach is valid. Only through the comparison of field data and the predictions from the continuum models can the validity of the continuum hypothesis be judged (Saphiro 1987).

We use the term *induced field* to refer to a property distribution characterizing the SRV that fosters the flow of hydrocarbons into the main hydraulic fractures (HFs) compared

to the original state of the formation. We expect the induced field to be nonuniform, because the energy coming from the source during the fracturing treatment dissipates as the distance to the source increases. In this context, we studied in the previous sections the effect of a nonuniform permeability distribution (depending on the distance to the HFs) on well performance (Fuentes-Cruz et al. 2014a, 2014b and 2014c). We referred to this concept as the *induced permeability field* and developed the corresponding models for the single porosity and dual porosity idealizations. The induced permeability field concept, however, does not deal with the physical reasons for the flow enhancement; it just describes the end-result in a suitable way.

The current description of the induced field is depicted by the conceptual notion of the fracture network that should develop to produce shale formations economically (**Fig. 4.1**). The physical model, related to the network propagation depending on the geomechanical properties of the system, is typically described as a complex branching of the natural and artificial fractures. However, the corresponding flow model can be studied as a variable matrix block distribution.

Fig. 4.1—Conceptual model of the induced field. The complex fracture network can be studied as a matrix block distribution with nonuniform size. From http://www.fracfocus.ca (left), http://www.bakerhughes.com (right).

The novelty of the model introduced in this work is in capturing the underlying geophysics of the enhanced flow properties of the SRV, but not descending into the actual modelling of the geomechanical processes during (and after) the treatment. We consider that the intensive fracturing operation creates a nonuniform distribution of micro-fractures such that the highest density of micro-fractures is located near the HF face and, as the distance to the HF increases, the fracture density decreases. Since the fracture density is reciprocally related to the matrix-block size, this means that matrix block size grows as the distance to the HF face increases. In the approach presented in this work, the REV contains matrix blocks having the same size, but this size depends on the distance to the HF face. In our view, an explicit distance-dependent matrix-block size is consistent with the general trend in all microseismic observations indicating more stimulation near the HF and gradually diminishing stimulation towards the boundaries of the SRV.

The variable matrix-block-size distribution can be interpreted as an *induced interporosity-flow field* because the characteristic matrix dimensions control the available area of contact between the matrix blocks and the fracture system. In our approach, the matrix-fracture contact area is the key controlling factor for the flow of fluids from the (ultra-tight to tight) matrix blocks to the network of natural and induced fractures.

In the widely used models for naturally fractured reservoirs (Warren and Root 1963; Kazemi 1969), the well-known dimensionless interporosity-flow coefficient (λ) involves not only the ratio between the matrix and fracture permeabilities, but also the matrix blocks geometry, which in turn relates the volume of the matrix blocks and the surface area available for the transfer of fluids between matrix and fractures. Thus, the parameter λ depends on the distance to the HF planes: a decrease in the characteristic matrix-block dimensions near the HF face corresponds to an increase in the interporosity-flow coefficient (i.e., an enhancement in the ability of the matrix blocks to feed the network).

The objectives of this section are to scrutiny on the effects of the induced interporosity-flow field on the well performance and to introduce the Airy-spline scheme to solve the corresponding differential equation. The results obtained reveal that the new model explains the elongated apparent linear flow period of the well performance by considering the highest density of micro-fractures near the hydraulic fracture faces.

These closely spaced micro-fractures have a strong impact on the well performance, even if their density diminishes towards the outer boundaries of the SRV.

4.2. Variable matrix-block-size (variable interporosity–flow field) model

The mathematical model is the generalization of the classical dual medium models, augmenting them with location dependent interporosity parameters. Using the Laplace transform approach and the Airy-spline scheme developed in this work (Appendix D), the numerical inversion provides the solution in time domain. To our knowledge, a semi-analytical model with distance-dependent matrix-block size has not been solved before.

4.2.1. Model description

We consider the dual porosity/dual permeability reservoir in a continuum framework. The primary porosity system is called the matrix; it has a constant and small permeability throughout the reservoir and acts as a source of fluid to the fractures. For brevity, we use the terminology *fracture* to describe the secondary porosity system: natural fractures enhanced by the intensive fracturing operation together with the induced fractures developed during the treatment. These fractures, with constant permeability, are considered the dominant conduit of fluids from the reservoir to the main HFs. The nonuniform fracture permeability approach (with constant matrix-block size) was studied in section 3. The matrix and fracture systems are referred with the sub-indexes *m* and *f*, respectively. The symbol (^) denotes bulk property.

Fig. 4.2 introduces the conceptual model representing the situation after an intensive hydraulic stimulation treatment in a shale reservoir. The model corresponds to a multi-fractured horizontal well (MFHW) with n_{HF} vertical HFs equally distributed along the horizontal wellbore with a distance $2y^*$ between them. The infinite-conductivity HFs are assumed symmetric with respect to the wellbore intersections (two wings of equal length, x_{HF}), such that the lateral extent of the stimulated reservoir (x_e) is equal to $2x_{HF}$. Also, the HFs fully penetrate the reservoir in height (h). The drainable reservoir is confined to the SRV because the contribution of flow from the non-stimulated region is negligible. Assuming identical HFs, we examine only one representative HF and its drainage.

The configuration depicted in Fig. 4.2 can be studied by selecting one stimulated reservoir element (SRE) in such a way that the total production rate is equal to n_{HF} times the production coming out the SRE. The central assumption in this work is that the characteristic dimensions of the matrix blocks (r_m) depend on the distance to the HF plane in the SRE. Because the stimulation is more effective near the HF, it is reasonable to think that the density of the fractures is higher near the main HF face, leading to smaller matrix blocks.

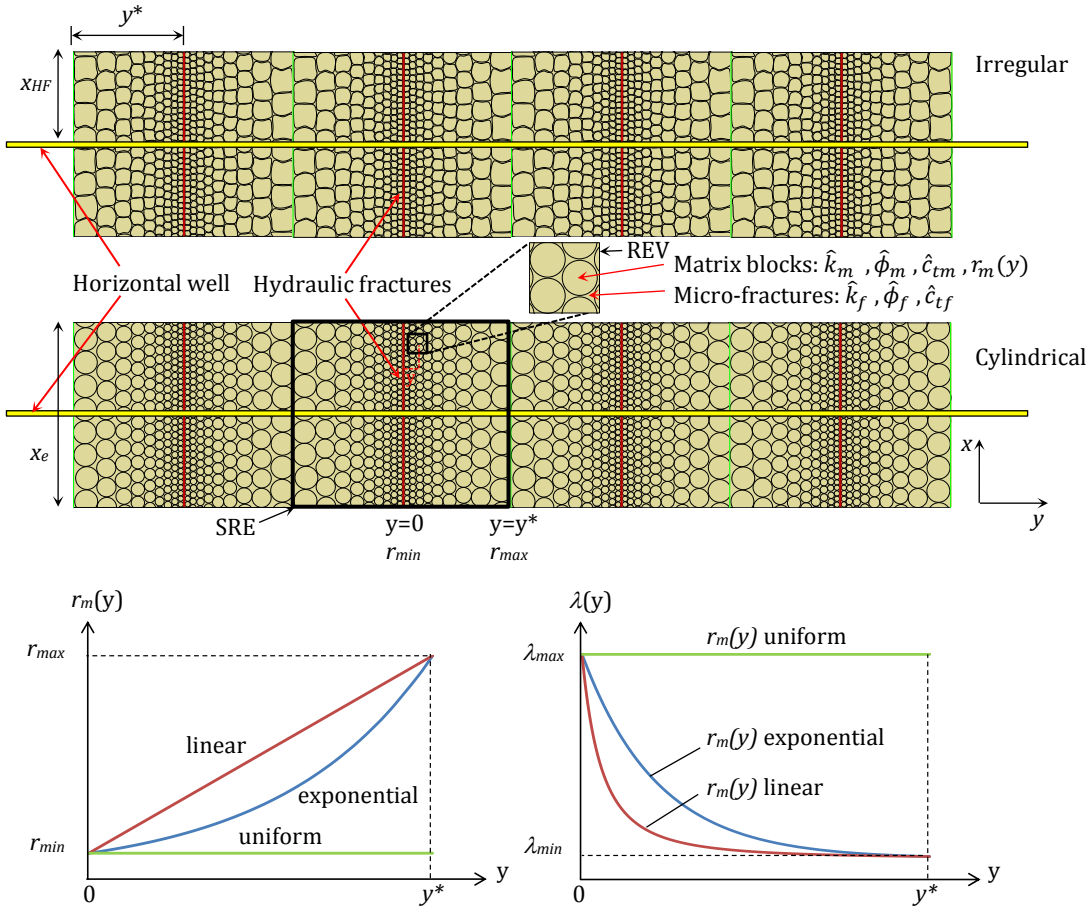

Fig. 4.2—Plain view of an MFHW. In the variable matrix-block size model, the matrix blocks are approximated by cylindrical-shaped blocks. The characteristic size of the matrix blocks gradually increases away from the hydraulic fracture.

Fig. 4.2 shows the linear and exponential dependency of the matrix blocks (in addition to the standard uniform matrix-block size) and the corresponding effect on the parameter λ(y) (see Eqs. D-30a through D-31b). From this qualitative description, we can infer that, for a given geometry, the well productivity in the linear dependency model will be lower than the exponential case because the interporosity-flow coefficient decreases faster (this will be demonstrated in the next subsection). The characteristic length of the

matrix blocks (the interporosity-flow coefficient) goes from $r_{min}[\lambda_{max}]$ at the fracture face ($y = 0$) to $r_{max}[\lambda_{min}]$ at the boundary of the SRE ($y = y^* \; and \; y = -y^*$). The model collapses to the uniform case for $r_{min} = r_{max}[\lambda_{max} = \lambda_{min}]$.

Currently, there is little physical evidence to support a particular functional form for the matrix block-size dependency. Thus, linear and exponential functions are assumed because these are the simplest possible matrix-block size distributions. Further efforts are needed to determine the actual functional form. We note that, in the future, microseismic data interpretation might guide the selection of the appropriate matrix-block size dependency. We emphasize that the Airy-spline scheme developed to solve the mathematical model in the Laplace space (Appendix D) is not restricted to linear and exponential functions. Basically, the linear and exponential cases are only examples. Any monotonically decreasing smooth function can be assumed.

With the above assumptions, in Appendix D we derive the one-dimensional dual porosity/dual permeability model with the induced interporosity flow field:

$$\frac{d^2\bar{p}_{fD}}{dy_D^2} = uf(u, y_D)\bar{p}_{fD} \quad \text{.....(4.1)}$$

where:

$$f(u, y_D) = \omega + \frac{\lambda(y_D)}{4u}\sqrt{\frac{8(1-\omega)u}{\lambda(y_D)}}\frac{I_1\left(\sqrt{\frac{8(1-\omega)u}{\lambda(y_D)}}\right)}{I_0\left(\sqrt{\frac{8(1-\omega)u}{\lambda(y_D)}}\right)} \quad \text{.....(4.2)}$$

The boundary conditions are:

$$\left(\frac{d\bar{p}_{fD}}{dy_D}\right)_{y_D=0} = -\frac{\pi}{2u} \quad \text{.....(4.3)}$$

$$\left(\frac{d\bar{p}_{fD}}{dy_D}\right)_{y_D=y_D{}^*} = 0 \quad \text{.....(4.4)}$$

And zero initial pressure-distribution condition. The model is fundamentally different from the usual dual porosity model because of the explicit dependence of the $f(u, y_D)$ function on the y_D variable.

4.2.2. Approximate formulae in the time domain

We can obtain closed form solutions of production rate in the time domain, corresponding to different flow regimes. These solutions assume zero skin factor and constant wellbore pressure (CWP). The short-time approximation is:

$$q_{wlD-STA} = \frac{2\sqrt{\omega}}{\pi^{3/2}\sqrt{t_D}} \quad \text{.....(4.5a)}$$

In real variables:

$$q_{wl-STA} = \frac{2T_{sc}}{\sqrt{\pi}p_{sc}} \frac{n_{HF}h\sqrt{\widehat{\phi}_{fi}\hat{c}_{tfi}\mu_i}[m(p_i)-m(p_{wf})]}{T} \frac{x_{HF}\sqrt{\hat{k}_f}}{\sqrt{t}} \quad \text{.....(4.5b)}$$

Thus, similar to the constant matrix-block size, the transient linear flow in the fractures is present during the short time. The expression for bilinear flow corresponding to simultaneous transient linear flow in the fractures and matrix blocks is:

$$q_{wbD-STA} = \frac{2^{3/4}}{\pi\Gamma(3/4)} \frac{\sqrt[4]{\lambda_{max}(1-\omega)}}{\sqrt[4]{t_D}} \quad \text{.....(4.6a)}$$

In real variables:

$$q_{wb-STA} = \frac{2\sqrt{2}T_{sc}}{\Gamma(3/4)p_{sc}} \frac{n_{HF}h[m(p_i)-m(p_{wf})]x_{HF}}{T} \sqrt{\frac{\hat{k}_f}{r_{min}}} \left[\frac{t}{\mu_i\hat{k}_m\widehat{\phi}_{mi}\hat{c}_{tmi}}\right]^{-1/4} \quad \text{.....(4.6b)}$$

Where $\Gamma(x)$ is the Gamma function. It is worth noting that Eqs. 4.6a and 4.6b are the same for the uniform, linear and exponential matrix block-size dependency. If there is linear flow as a result of interporosity flow from the nonuniform matrix blocks into the fractures (*induced linear interporosity flow*), then the intermediate-time approximation is ($\lambda_{max} > \lambda_{min}, r_{max} > r_{min}$):

$$q_{wlD-ITA} = \frac{\sqrt{2}y_D^*\sqrt{1-\omega}}{\pi^{3/2}F_\lambda\sqrt{t_D}} \quad \text{.....(4.7a)}$$

In real variables:

$$q_{wl-ITA} = \frac{4T_{sc}}{\sqrt{\pi}p_{sc}} \frac{n_{HF}hy^*[m(p_i)-m(p_{wf})]\sqrt{\mu_i\hat{\phi}_{mi}\hat{c}_{tmi}}}{TF_r} \frac{x_{HF}\sqrt{\hat{k}_m}}{\sqrt{t}} \quad \text{.....(4.7b)}$$

where:

$$F_\lambda = \begin{cases} \frac{1}{\sqrt{\lambda_{eff}}};\ r_{mD}(y_D)\ linear \\ \frac{\sqrt{\lambda_{eff}}}{\lambda_{max}\lambda_{min}};\ r_{mD}(y_D)\ exponential \end{cases} \quad \text{.....(4.8)}$$

$$F_r = \begin{cases} r_{eff}\ ;\ r_m(y)\ linear \\ \frac{r_{min}r_{max}}{r_{eff}}\ ;\ r_m(y)\ exponential \end{cases} \quad \text{.....(4.9)}$$

r_{eff} is the effective matrix-block radius; it is defined as the logarithmic mean of r_{min} and r_{max}:

$$r_{eff} = \begin{cases} \frac{r_{max}-r_{min}}{ln(r_{max}/r_{min})} & r_{max} \neq r_{min} \\ r_{min} & r_{max} = r_{min} \end{cases} \quad \text{.....(4.10)}$$

In Eq. 4.8, λ_{eff} is the effective dimensionless interporosity-flow coefficient based on the effective radius:

$$\lambda_{eff} = \frac{8}{(r_{eff}/x_{HF})^2}\frac{\hat{k}_m}{\hat{k}_f} = \frac{\lambda_{min}\lambda_{max}}{\sqrt{\lambda}_{lm}^2} \quad \text{.....(4.11)}$$

$\sqrt{\lambda}_{lm}$ is the logarithmic mean of $\sqrt{\lambda_{min}}$ and $\sqrt{\lambda_{max}}$. Eqs. 4.7a and 4.7b collapse to the constant matrix-block-size case when $\lambda_{max} = \lambda_{min} = \lambda$,, ($r_{max} = r_{min} = r_m$, linear interporosity flow):

$$q_{wlD-ITA} = \frac{\sqrt{2}y_D^*\sqrt{\lambda}\sqrt{(1-\omega)}}{\pi^{3/2}\sqrt{t_D}} \quad \text{.....(4.12a)}$$

$$q_{wl-ITA} = \frac{4T_{sc}}{\sqrt{\pi}p_{sc}}\frac{n_{HF}hy^*[m(p_i)-m(p_{wf})]\sqrt{\mu_i\hat{\phi}_{mi}\hat{c}_{tmi}}}{Tr_m}\frac{x_{HF}\sqrt{\hat{k}_m}}{\sqrt{t}} \quad \text{.....(4.12b)}$$

Eq. 4.7b reveals a fundamental behavior in massively stimulated reservoirs when λ_{eff} is small: if the matrix-block size distribution is nonuniform, then the linear flow is controlled by a function involving the logarithmic mean. In particular, for the linear matrix-block-size dependency, the linear flow depends on the effective matrix-block dimension, equal to the logarithmic mean of the minimum and maximum matrix-block size. The implications of the logarithmic mean are important because the mean separates the geometric and arithmetic means (Carlson, 1972):

$$\sqrt{r_{min}r_{max}} \leq r_{eff} \leq \frac{r_{min}+r_{max}}{2} \quad (4.13)$$

Moreover, the effective size is closer to the minimum value (r_{min}). Therefore, the high density of micro-fractures near the HF faces has a significant impact on well performance, even when such micro-fractures do not extend throughout the whole reservoir.

According to Eq. 4.7b, by the time the induced linear interporosity flow is observed, the production response already contains information located at the reservoir limits (the maximum matrix-block size is at the external boundary of the SRE, see Fig. 4.2). Hence, by the beginning of this flow regime, the well performance has *detected* the whole reservoir. This observation brings out a conceptual element that should be revisited: if we consider the definition $\partial p/\partial t = f(\vec{r}, t)$ as the condition for transient flow (Dake 1978), then the induced linear interporosity flow is a transient flow regime, but we have to discard the general concept of infinite-acting conditions. There is another linear flow at intermediate time when the interporosity flow coefficient is high:

$$q_{wlD-ITA} = \frac{2}{\pi^{3/2}\sqrt{t_D}} \quad (4.14a)$$

Eq. 4.14a is equivalent to the well-known *total system response* of fractures and matrix blocks, widely reported in the literature of pressure transient testing in conventional

naturally fractured reservoirs (NFRs) with radial geometry (radial flow). In real variables:

$$q_{wl-ITA} = \frac{2T_{sc}}{\sqrt{\pi}p_{sc}} \frac{n_{HF}h\sqrt{(\hat{\phi}_{fi}\hat{c}_{tfi}+\hat{\phi}_{mi}\hat{c}_{tmi})\mu_i}[m(p_i)-m(p_{wf})]}{T} \frac{x_{HF}\sqrt{\hat{k}_f}}{\sqrt{t}} \quad \text{.....(4.14b)}$$

4.2.3. Well performance in reservoirs with uniform properties

According to the standard definition of the interporosity-flow coefficient (λ), its value is controlled by two factors, $\hat{k}_m/\hat{k}_f$ and r_m/x_{HF} (Eq. 4.15):

$$\lambda = \frac{8}{(r_m/x_{HF})^2} \frac{\hat{k}_m}{\hat{k}_f} \quad \text{.....(4.15)}$$

In the case of the uniform matrix-block size and uniform permeability field, high values of λ [$\lambda \gg 2/((1-\omega)y_D^{*2})$] lead to a bilinear flow followed by a long linear flow corresponding to the total system response (blue and red curves in **Fig. 4.3A**). During this linear flow (Eqs. 4.14a and 4.14b) the production behavior corresponds to a homogeneous reservoir with permeability equal to that of the fractures ($\hat{k}_f$) and a storativity equal to that of the total system ($\hat{\phi}_f\hat{c}_{tf} + \hat{\phi}_m\hat{c}_{tm}$). For the existence of the total system response, the pressure signal in the matrix have to reach the center of the matrix blocks before the pressure signal in the fracture system reaches the boundaries of the reservoir. This may be the case in most conventional NFRs because of the relatively high permeability of the matrix system. Regarding unconventional reservoirs, the total

system response is possible when the matrix-to-fracture permeability ratio is high and there is an interconnected micro-fracture network with very small micro-fracture spacing (Tivayanonda et al. 2012; Kanfar et al. 2013). The condition $\lambda \approx 2/((1-\omega)y_D^{*2})]$, usually leads to a bilinear flow with a short duration or no presence of linear flow.

When λ is small [$\lambda \ll 2/((1-\omega)y_D^{*2})]$, the observed long linear flow at intermediate time represents the *linear interporosity flow* (Eqs. 4.12a and 4.12b), in which the pressure signal in the fracture system reaches the boundaries of the reservoir ($-y_D^*$ and y_D^*) before the flow of fluids from the matrix blocks to the fracture system becomes significant. During this linear flow the production behavior corresponds to a reservoir with permeability and storativity equal to those of the matrix blocks ($\hat{k}_m$ and $\hat{\phi}_m\hat{c}_{tm}$). This may be the case in unconventional reservoirs when the matrix-to-fracture permeability ratio is small (ultra-tight matrix blocks and high fracture permeability), leading to small values of λ [see Tivayanonda et al. (2012) for a detailed description of the flow regimes].

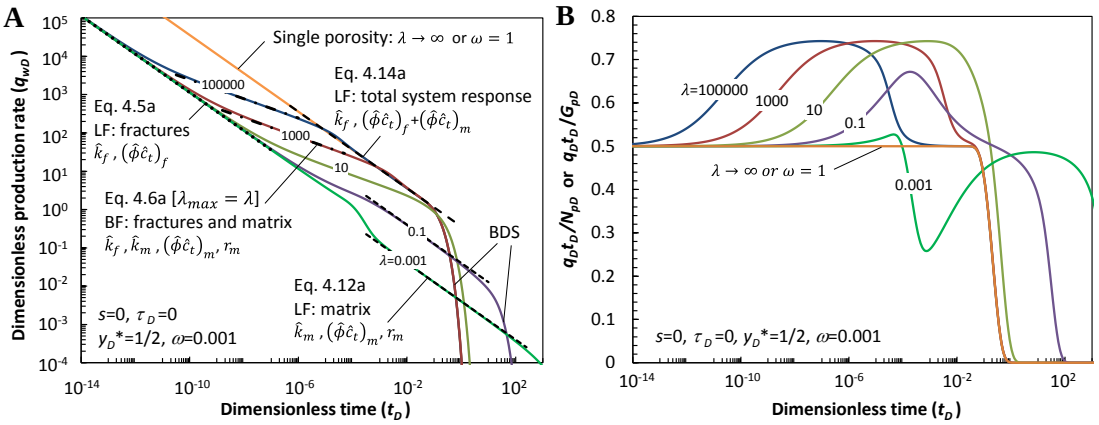

Fig. 4.3—Flow regimes in the well performance of an MFHW producing in an unconventional reservoir with uniform properties. LF: linear flow, BF: bilinear flow. [see also Tivayanonda et al. (2012)]

The linear interporosity flow is not limited to linear geometries, see e.g. Marhaendrajana et al. (2004) and Kuchuk and Biryukov (2014). It can be present in radial geometries (usually conventional reservoirs) when the transfer of fluids between matrix blocks and fractures is poor. In this case, the characteristic equation of a well producing in a closed NFR also depends on the square root of time:

$$q_{wl-ITA-radial} = \frac{\sqrt{\pi} T_{sc}}{p_{sc}} \frac{h(r_e^2 - r_w^2)[m(p_i) - m(p_{wf})]\sqrt{\mu_i \hat{\phi}_{mi} \hat{c}_{tmi}}}{T h_m} \frac{\sqrt{\hat{k}_m}}{\sqrt{t}} \quad \text{.....(4.16)}$$

Where r_e and r_w are the drainage radius and wellbore radius, respectively. The parameter h_m is the width of the matrix blocks (horizontal slabs). Basically, the linear interporosity flow occurs when the pressure signal in the fracture network travels fast, compared to the pressure signal transmission in the matrix blocks.

Fig. 4.3B shows the dimensionless group $q_D t_D / G_{pD}$ versus time. This format is useful for diagnostic purposes; especially to identify a departure from the linear (1/2 level) and bilinear (3/4 level) flows. In this work, we show that the flow regimes identified in a reservoir with uniform properties are also present in the nonuniform matrix-block-size case, but with variants in the parameter interpretations. It seems that small matrix-block size (high density of fractures) is needed to facilitate the transfer of fluids from the (ultra-tight to tight) matrix blocks. However, it is difficult to justify small matrix blocks throughout the whole reservoir, as predicted by the models assuming uniform properties; this observation has been lingering over attempts to describe well performance in unconventional reservoirs. In the following subsection, we investigate the effects of the nonuniform matrix-block distribution on the well performance. When the total system response is present (Eqs. 4.14a and 4.14b), we keep λ_{min} fixed and vary λ_{max}. When the induced linear interporosity *flow* is present (Eqs. 4.7a and 4.7b), we keep λ_{max} fixed and vary λ_{min}, such that λ_{eff} is different in each curve.

4.2.4. Well performance in reservoirs with nonuniform properties

Fig. 4.4 shows the well performance for uniform and nonuniform interporosity flow (uniform and nonuniform matrix-block size) from synthetic data, assuming cylindrical matrix-block shape and linear dependency in the matrix-block dimensions. These simulations verify that the dimensionless production rate during the bilinear flow depends only on λ_{max} when ω is small (Eq. 4.6a). For a given λ_{min}, the beginning of the linear flow corresponding to the total system response is affected by λ_{max} significantly.

For a given $\hat{k}_m/\hat{k}_f$ ratio, the small matrix blocks near the HF faces accelerate the beginning of the transient linear flow, even when the size of the matrix blocks are kept fixed at the outer boundaries of the SRE ($-y_D^*$ and y_D^*). In Fig. 4.4, the linear flow is not well defined when λ_{min}=100, however, the reduction of the matrix blocks towards the vicinity of the HF faces lead to a well-defined linear flow (λ_{max}>100).

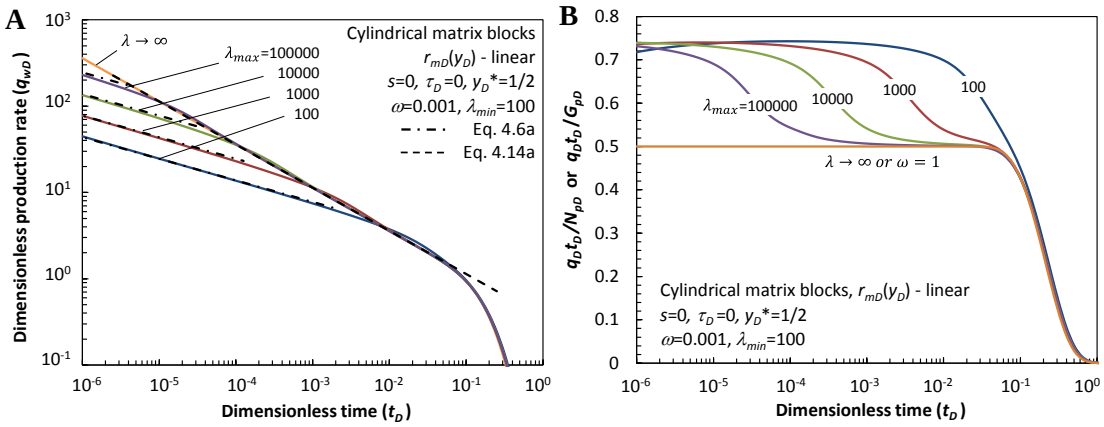

Fig. 4.4—The smaller the matrix-block size near the HF face (larger λ_{max}), the earlier the beginning of the linear flow corresponding to the total system response.

The total system response linear flow is the same as in the uniform case (depicted with $\lambda \to \infty$ in Fig. 4.4). The matrix distribution plays a secondary role, though the smaller matrix blocks control the beginning of the total system response. If only this flow regime is observed, then there is no information related to the matrix-block distribution because the well performance corresponds to that of a homogeneous system with permeability and storativity equal to $\hat{k}_f$ and $(\hat{\phi}_f \hat{c}_{tf} + \hat{\phi}_m \hat{c}_{tm})$, respectively. The total system response

is infinite acting because during this flow regime the pressure signal has not reached the outer boundaries of the SRE ($-y_D^*$ and y_D^*).

We found no significant differences in the production behavior when λ_{max} is kept fixed at 100,000 and λ_{min} is varied from 100,000 to 100.

The following six figures show the well performance when the *induced linear interporosity flow* is present. In **Fig. 4.5A,** the negative half slope appears when λ_{eff} is small even when λ_{max} is not small (this can be interpreted as a high density of micro-fractures near the HF face). The uniform case does not develop a well-defined linear flow (blue curve with $\lambda_{eff} = 1$). According to Fig. 4.5, the occurrence of the induced linear interporosity flow (negative half slope, Eq. 4.7a) increases as λ_{eff} decreases. In general, the well productivity decreases as λ_{eff} decreases because of the reduction in the area of contact between the matrix blocks and the fracture network; this observation is similar to the uniform matrix-block behavior. However, the uniform case suggests low fractures density (based on the linear interporosity flow interpretation). Thus, the spatial dependence of $\lambda(y)$ may be the key to resolving the observation related to more stimulation near the HFs.

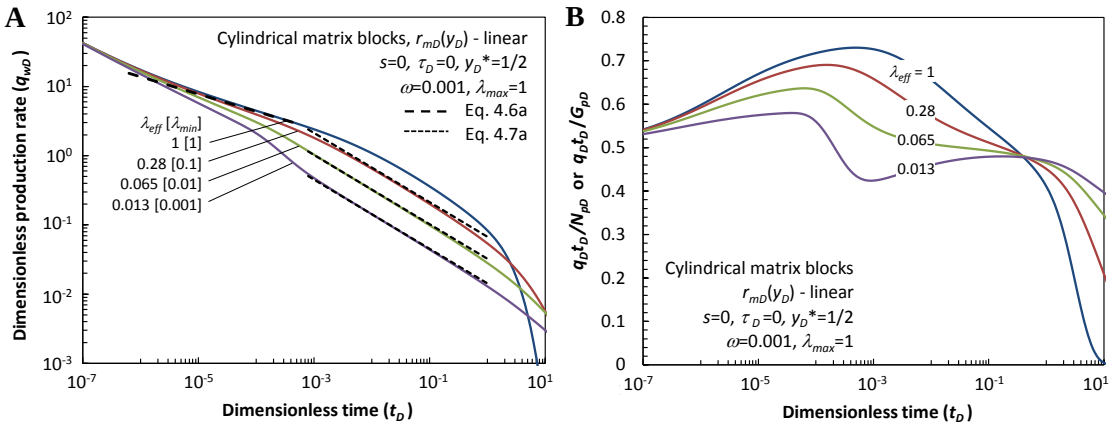

Fig. 4.5—The occurrence of the negative half slope (induced linear interporosity flow) increases as λ_{eff} decreases, even when λ_{max} is not small.

In the exponential matrix-block-size dependency (**Fig. 4.6**), the effect of λ_{eff} is less severe than in the linear case because $\lambda(y)$ does not decrease sharply (see Fig. 4.2).

If there is no bilinear flow before the induced linear interporosity flow, then the pressure disturbance in the fracture system reaches the reservoir boundaries before the matrix blocks feed the fracture system significantly, in such a way that the well performance responds to the effective matrix-block size (r_{eff}) during the induced linear interporosity flow. If there is a bilinear flow, then the matrix blocks feed the fracture system before the pressure signal in the fracture system reaches the limits. In general, the early linear flow in the fractures and the bilinear flow, when present, are both transient and infinite acting. However, the induced linear interporosity flow is transient, except infinite acting.

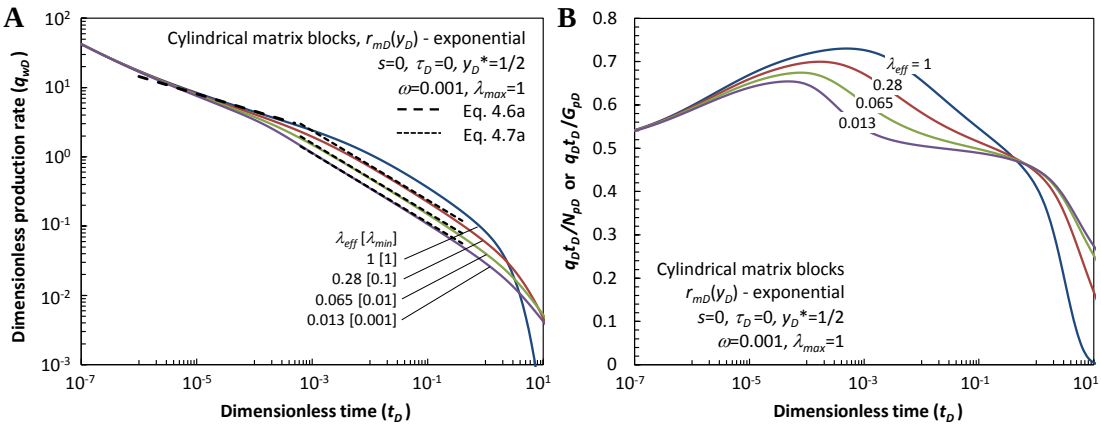

Fig. 4.6—Irrespective of the functional form of the matrix-block size (linear or exponential dependency), the linear flow appears as a characteristic signature of the well performance.

Fig. 4.7 shows a comparison between uniform, linear, and exponential dependency of the matrix-block size. One order of magnitude between the maximum and minimum matrix-block size strongly reduces the productivity of the MFHW compared to the uniform distribution with λ_{eff} =λ_{max} =1. As depicted in Fig. 4.2, the interporosity flow coefficient of the linear distribution decreases faster than in the exponential case, as the distance to the HF increases, leading to a stronger reduction of the well performance in the linear case. The bilinear flow is fully developed in the uniform case when λ_{eff} is relatively high (λ_{eff} =λ_{max} =1). On the other hand, the linear flow is fully developed in the linear, exponential, and uniform distributions when λ_{eff} =0.065. Thus, the variable interporosity flow approach is consistent with both the common signature of unconventional reservoirs (linear flow) and with the common intuition that effective treatments establish high-density of microfractures near the HFs. Moreover, this comparison highlights the importance of high density of micro-fractures and their

penetration into the stimulated volume. In this case, the fracturing fluids should be pervasive to increase the well productivity.

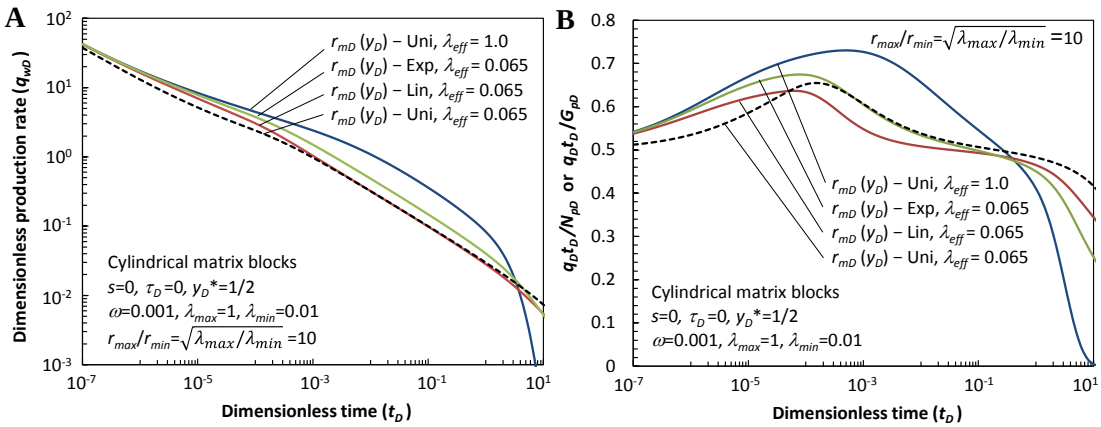

Fig. 4.7—During the induced linear interporosity flow, the well productivity of the linear-dependency case is smaller than the exponential because the interporosity flow of the linear case reduces sharply.

The transient linear flow in the micro-fractures (Eq. 4.5a) is present during the short time, as shown in **Fig. 4.8.** In this example, the highest value of λ_{eff} is small enough $[\lambda_{eff} \ll 2/((1-\omega)y_D^{*2})]$ to fully develop the linear interporosity flow in the uniform matrix-block case (Fig. 4.8, $\lambda_{eff} = 0.1$). In some cases, the long linear flow can theoretically last much more than average the productive life of the well. When $\lambda_{eff} \ll 2/((1-\omega)y_D^{*2})]$, the main signature of the variable matrix block model is a long induced linear interporosity flow with a smooth transition towards the boundary-dominated state (BDS). The smooth transition happens because the pressure signal reaches first the center of the smaller matrix blocks while in those with bigger sizes the pressure signal is still in transient conditions. Thus, the matrix depletion is gradual.

Conversely, in the constant matrix-block-size case, all the matrix blocks deplete simultaneously, leading to a less gradual transition from the linear interporosity flow to the BDS.

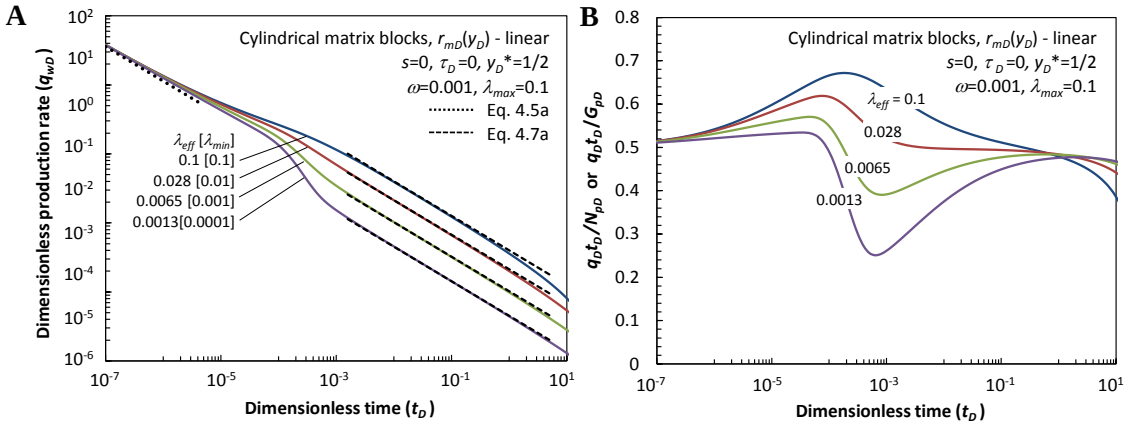

Fig. 4.8—Similar to the constant matrix block size, the transient linear flow in the fractures is present during the short time. Long induced linear interporosity flow with a smooth transition towards the BDS is the main signature of the variable matrix block model.

In **Figs. 4.9 and 4.10** we show how the well performance is affected by the skin factor and the decaying wellbore pressure (DWP), respectively. We showed (Fuentes-Cruz et al. 2014a, 2014b and 2014c) that the dimensionless group $(q_D t_D/G_{pD})$ approaches the value of one in the presence of the skin factor (Fig. 4.9B), corresponding to a flattening at short times in the log-log plot of production rate versus time (Fig. 4.9A). On the other hand, the dimensionless group $(q_D t_D/G_{pD})$ approaches the value of two in the presence of the skin factor and DWP (Fig. 4.10B), corresponding to the increasing trend at short times in Fig. 4.10A. The analytical DWP function is used to account for an abrupt

change of the wellbore pressure at short time; it is characterized by the parameter τ. These two effects (skin factor and DWP) can mask the signature of the early response of the fracture system.

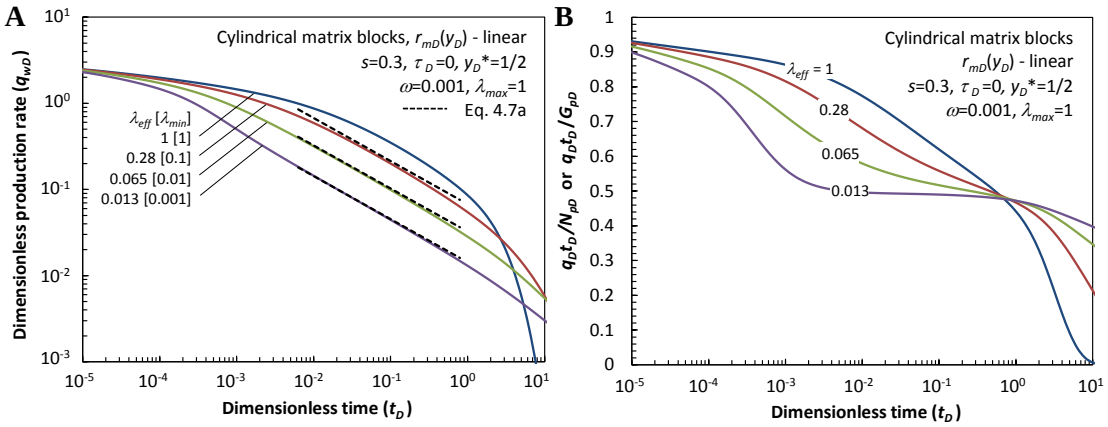

Fig. 4.9—The skin factor causes a flattening of production rate at short time which masks the signature of the early response of the fracture system. The dimensionless group $q_D t_D/G_{pD}$ approaches a value of one during the short time.

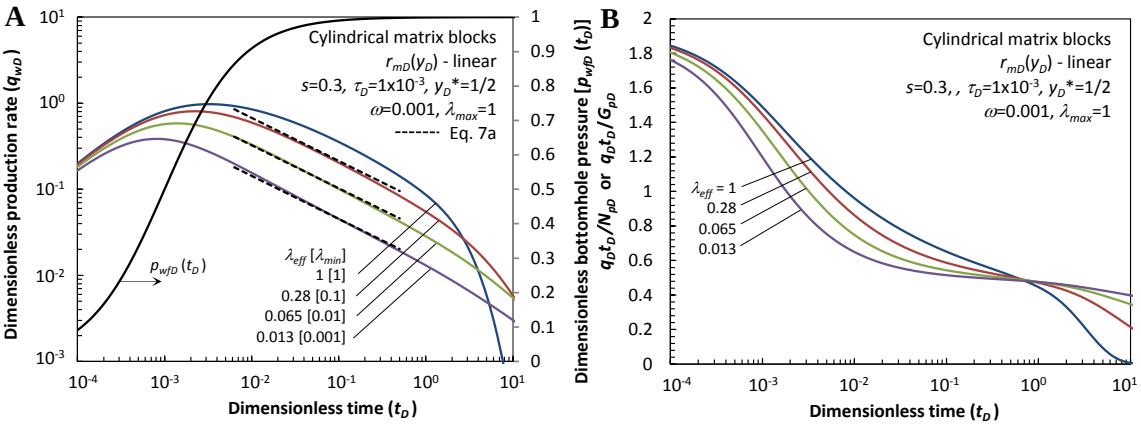

Fig. 4.10—The variable bottomhole flowing pressure leads to an increasing trend of production rate at short times. The dimensionless group $q_D t_D/G_{pD}$ approaches a value of two at short times.

The response predicted by the dual porosity/dual permeability model under ideal conditions (no skin factor and CWP) is complex (Figs. 4.3B through 4.8B), but the early history of this behavior can be masked by the combination of the variable bottomhole flowing pressure and the skin factor, leading to a continuous decreasing trend in the dimensionless group as shown in Figs. 4.9B and 4.10B. In other words, after the peak of production rate (or flattening response) is reached we usually observe a linear flow and then the transition to the BDS.

A similar analysis can be performed when the total system response linear flow is present. It can be shown that the variable wellbore pressure and the skin factor can mask the information related to the transfer of fluids between the matrix blocks and the fracture system.

Fig. 4.11 summarizes our findings: the two possible types of dominant linear flow, induced interporosity type and total system response type, are affected by the matrix-block-size distribution in different degree. The well performance is shown for two different values of the effective interporosity flow coefficient (λ_{eff} =0.01 and 500, though λ_{eff} is meaningless during the total system response linear flow). The induced linear interporosity flow is present when λ_{eff} =0.01, however, the departure from the -1/2 slope is earlier in the nonuniform case, leading to a gradual transition to the BDS. On the other hand, the total system response linear flow is present when λ_{eff} =500. As expected, the beginning of the -1/2 slope (total system response) is earlier in the nonuniform case

because $\lambda_{max}>\lambda_{eff}$. Fig. 4.11A also shows, qualitatively, the time window of real production data corresponding to the total system response linear flow (vertical red bars) and to the induced linear interporosity flow (vertical green bars). Both cases have a chance to have long linear flow with consistent interpretations depending on the values of the matrix and fractures permeabilities.

In summary, the transient linear flow in the fractures, present at very short times, corresponds to a homogeneous system with permeability and storativity equal to $\hat{k}_f$ and $\hat{\phi}_f\hat{c}_{tf}$ respectively. The transient bilinear flow, whose beginning and ending are affected by the interporosity flow coefficient near the HF faces, is controlled by $\hat{k}_f$, $\hat{k}_m$, $\hat{\phi}_m\hat{c}_{tm}$ and r_{min}. The total system response linear flow, present at intermediate time (long time in real variables) when the minimum interporosity flow coefficient is high, corresponds to that of a homogeneous system with permeability and storativity equal to $\hat{k}_f$ and $(\hat{\phi}_f\hat{c}_{tf}+\hat{\phi}_m\hat{c}_{tm})$, respectively. The induced linear interporosity flow, present at intermediate time when the effective interporosity flow coefficient is low, is controlled by $\hat{k}_m$, $\hat{\phi}_m\hat{c}_{tm}$ and r_{eff}.

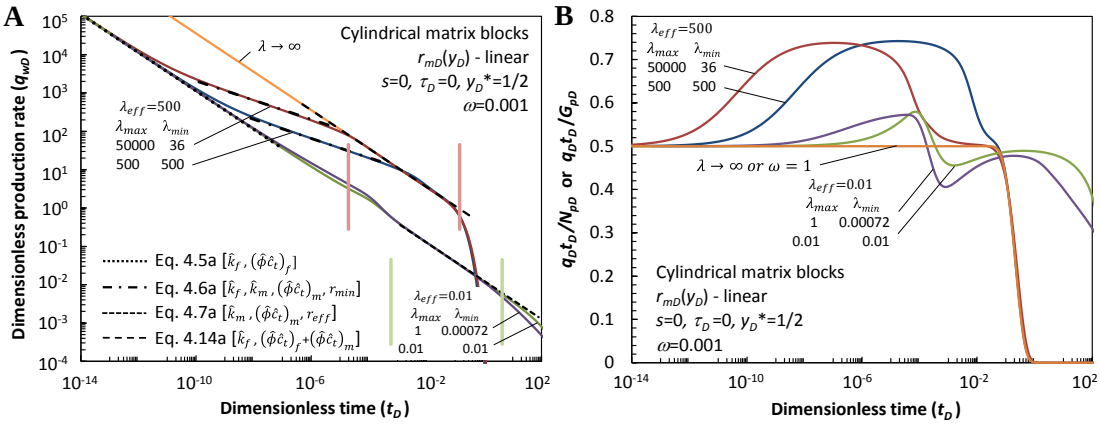

Fig. 4.11—Two different scenarios (*total system response* or *induced linear interporosity flow*) can describe the well performance in unconventional reservoirs. The impact of the nonuniform matrix block distribution is different in each case.

Tables 4.1 and 4.2 present the input data used to simulate the production history shown in **Fig. 4.12,** assuming cylindrical matrix-block shape and linear dependency of matrix size. This example was set to generate the induced linear interporosity flow (a similar procedure can be used to analyze the total system response). We used bulk properties and fracture characteristics that may represent the Barnett shale. In this example, the MFHW is producing through 14 main HF planes separated by a distance of 300 ft. The half-length of the HFs is 300 ft ($y_D^* = y^*/x_{HF} = 1/2$). We keep r_{min} fixed, and vary r_{max}, such that r_{eff} is different in each curve.

Table 4.1—Well and reservoir data. Synthetic example	
h, ft	300
$\hat{k}_f$, md	2.5×10^{-3}
$\hat{k}_m$, md	1.0×10^{-8}
$\hat{\phi}_{fi}\hat{c}_{tfi}$, psi^{-1}	1.26×10^{-8}
$\hat{\phi}_{mi}$, fraction	0.05
$\hat{c}_{tmi}$, psi^{-1}	2.51×10^{-4}
μ_i, cp	0.018
p_i, psia	3115
$p_{wf,stab}$, psia	500
$m(p_i)$, psi^2/cp	6.83×10^{8}
$m(p_{wf,stab})$, psi^2/cp	2.07×10^{7}
T, °R	633.5
x_{HF}, ft	300
y*, ft	150
n_{HF}, -	14
s, -	0.30
τ, days	1.30
r_{min}, ft	1.70

Table 4.2—Gas properties	
γ_g, -	0.5774
CO_2, %	1.858
H_2S, %	0
N_2, %	0.898

The log-log and semi-log plots of gas production rate versus time show that the effective size of the matrix blocks controls the production performance in unconventional reservoirs with ultra-tight matrix system significantly (Fig. 4.12). The early response corresponding to the transient linear flow in the fractures is masked by the combination of the skin factor and the DWP; the uniform matrix-block case does not develop the linear flow ($r_{eff} = 1.70$ ft). However, the induced linear interporosity flow is present when $r_{eff} \geq 3.19$ ft, but the matrix-block size is still 1.70 ft near the HF planes.

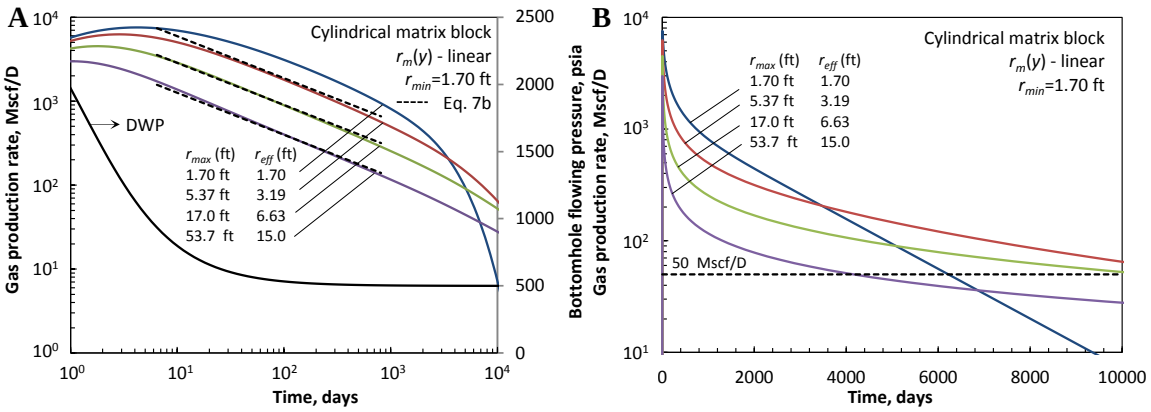

Fig. 4.12—Simulation of the pressure-production history for a typical MFHW producing in a shale reservoir. The effective matrix-block size strongly influences the production performance.

We can use the Cartesian slope of the straight line of the reciprocal production rate versus squared-root-of-time plot (m_c) to retrieve the effective matrix-block dimension. In field units:

$$r_{eff} = \frac{n_{HF} h y^* [m(p_i) - m(p_{wf})] \sqrt{\mu_i \hat{\phi}_{mi} \hat{c}_{tmi} x_f \sqrt{\hat{k}_m}}}{157\, T} m_c \quad \text{.....(4.17)}$$

Table 4.3 shows the effective radii corresponding to the three cases showing linear flow in Fig. 4.12A. There is good agreement between the input data and the estimated values using Eq. 4.17. Given the quality of the real production data, we can also match Eq. 4.7b directly on the log-log plot of production rate versus time, to estimate r_{eff}.

The values of minimum and maximum radii cannot be determined simultaneously; one of these parameters should be estimated from external data to have a full description of

the matrix-block-size distribution. For a fixed value of r_{min}, the estimated ultimate recovery at 20 years (EUR_{20yr}) and the time to reach the economic limit ($q_{lim} = 50$ Mscf/D) decrease as r_{eff} increases.

Table 4.3—Estimation of parameters from synthetic data

r_{max}(input), ft	r_{eff}(input), ft	m_c , (D/Mscf)/D$^{0.5}$	r_{eff}(from Eq. 4.17), ft	t_{qlim}, year	EUR_{20yr}, bcf
5.37	3.19	5.71x10^{-5}	3.42	32.9	2.3
17.0	6.63	1.18x10^{-4}	7.06	29.0	1.3
53.7	15.0	2.65x10^{-4}	15.8	11.4	0.6

4.3. Field example

We present a field example corresponding to a gas well producing in the Barnett shale. The bottomhole flowing pressure and production history is shown in **Fig. 4.13.** The early response of production rate, characterized by the increasing trend and the maximum, is influenced by the variation of the bottomhole flowing pressure and the skin factor. The -1/2 slope in the log-log plot of production rate versus time, observed from approximately 80 days until the end of the production history, corresponds to the induced linear interporosity flow if $\hat{k}_m/\hat{k}_f$ is low or to the total system response if $\hat{k}_m/\hat{k}_f$ is high.

As a first analysis, we consider that the linear flow observed in Fig. 4.13A is represented by the induced linear interporosity flow. We matched Eq. 4.7b with linear dependency (dashed straight line in Fig. 4.13A) to the actual data in the log-log plot and obtained an effective radius (r_{eff}) equal to 5.25 ft by using the input data in **Table 4.4.**

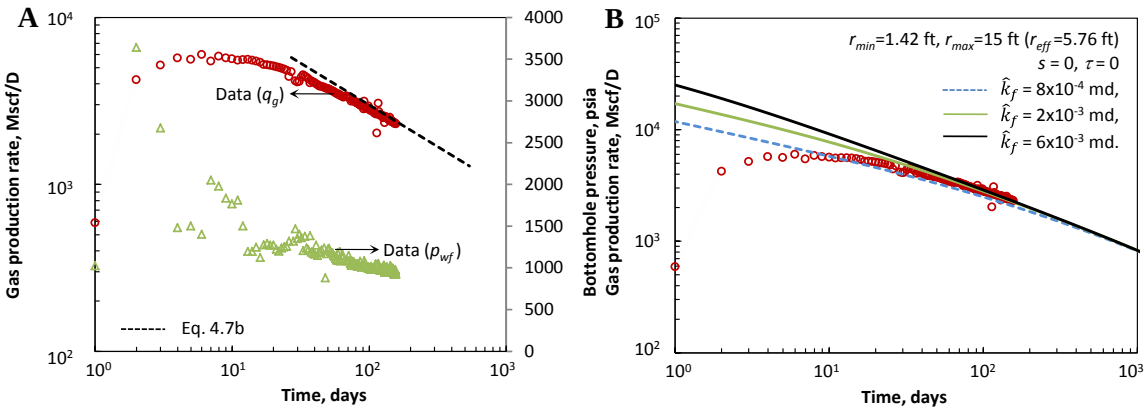

Fig. 4.13—Field data of a gas well producing in Barnett shale. The information corresponding to the fracture system is masked by the variable bottomhole pressure and the skin factor. However, we can estimate a threshold value of fracture permeability.

Table 4.4—Well and reservoir data. Field example	
h, ft	356
$\hat{k}_m$, md	1.0x10^{-8}
$\hat{\phi}_{mi}$, fraction	0.069
$\hat{c}_{tmi}$, psi^{-1}	1.92x10^{-4}
μ_i, cp	0.0192
p_i, psia	3693
$p_{wf,stab}$, psia	980
$m(p_i)$, psi^2/cp	9.07x10^8
$m(p_{wf,stab})$, psi^2/cp	7.64x10^7
T, °R	652.8
x_{HF}, ft	400
y*, ft	370
n_{HF}, -	8

Fig. 4.13B shows a sensitivity analysis of the fracture permeability ($\hat{k}_f$) using a slightly higher value of effective radius (5.76 ft) and $\hat{\phi}_{fi}\hat{c}_{tfi} = 1.33x10^{-8}$ psi^{-1}. In this analysis, we assume ideal conditions (zero skin factor and CWP) by using Eq. D-49. The information regarding the fracture system is masked by the combined effect of skin factor and the variable bottomhole pressure in the actual data, such that it is not possible

to estimate a specific value of $\hat{k}_f$. However, assuming $\hat{k}_f$ below 2x10^{-3} md underestimates the gas production rate during the linear flow (dashed line on Fig. 4.13B). We can use this observation to conclude that $\hat{k}_f \geq 2x10^{-3}$ md (for the set of data given in Table 4.4). The EUR_{20yr} for $\hat{k}_f$= 2x10^{-3} md, 6x10^{-3} md, and 1 md are 4.13 bcf, 4.15 bcf, and 4.16 bcf, respectively. Thus, high values of fracture permeability lead to the same production extrapolation with no significant effect on the EUR_{20yr}, yet the production rate is different at early times.

Fig. 4.14A presents the match of the pressure-production history by considering $\hat{k}_f = 2.0x10^{-3}$ md, $r_{eff} = 5.4$ ft and $\hat{\phi}_{fi}\hat{c}_{tfi} = 1.33x10^{-8}$ psi^{-1}. In this case, we kept a fixed value of the effective matrix-block size, but varied the minimum and maximum radius of the matrix blocks to quantify the effect on the production forecast. We also adjusted the skin factor and the parameter τ to match the early response on the production history. We used the *hill-shaped* function (Eq. C-5) to match the trend of the botomhole flowing pressure. The value of the parameter τ obtained from the analysis is in good agreement with the input data. The parameter $p_{wf,stab}$ shown in Table 4.4 corresponds to the last trend in the actual data (Fig. 4.14a); the value used in the hill-shaped function to fit the actual pressure data is 900 psia, with τ=3.4 days.

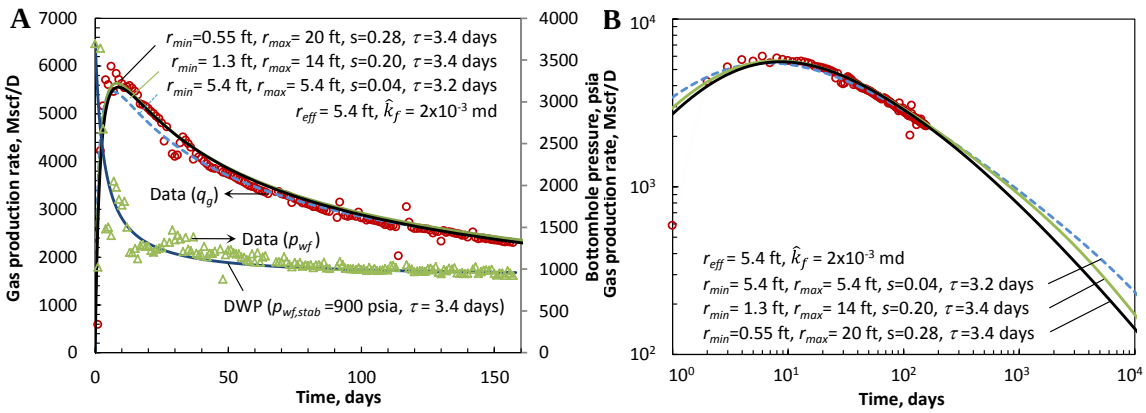

Fig. 4.14—Pressure-production analysis of the field example. Even if the effective matrix-block size is the same, the minimum and maximum values of the matrix size strongly influences the well performance.

Table 4.5 shows the EUR_{20yr} estimated from each case. Even when the effective radius in the three cases is the same, the minimum and maximum radius strongly influences the well productivity (Fig. 4.14B). The effective matrix-block size controls the well performance during the induced linear interporosity flow, but the departure from it depends on r_{min} and r_{max}.

Table 4.5—*EUR_{20yr}* for different minimum and maximum radius and same effective radius.

r_{min}, ft	r_{max}, ft	EUR_{20yr}, bcf
0.55	20	3.67
1.3	14	4.24
5.4	5.4	4.65

As a second analysis, the linear flow observed in Fig. 4.13A is considered as the total system response (Eqs. 4.14a and 4.14b) in a reservoir with uniform properties. In this case, $\hat{k}_f = 1.5x10^{-4}$ md and $\lambda \geq 10000$ match the linear flow period and lead to the

same production extrapolation assuming s=0 and τ=0 (**Fig. 4.15A**) and using Eq. D-49. The differences in production behavior at short time are masked by the variable bottomhole pressure and the skin factor effect. Fig. 4.15B shows the match and production extrapolation with $\hat{k}_f = 1.5x10^{-4}$ md, $\lambda = 10000$, s=0.03 and τ=1.7 days, leading to EUR_{20yr} = 4.74 bcf. If we assume $\hat{k}_m/\hat{k}_f$ equal to 0.0001 and 1, then r_m is equal to 0.11 ft and 11 ft, respectively. Higher values of the parameter λ lead to smaller matrix-block size.

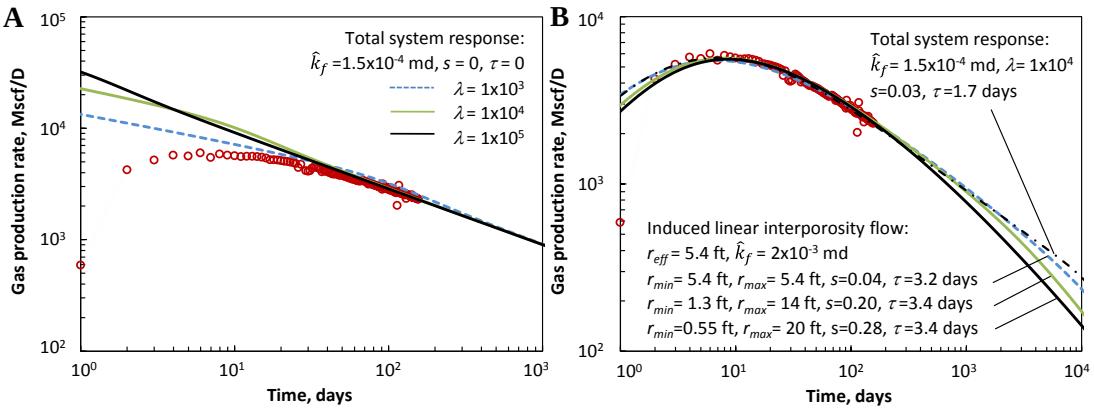

Fig. 4.15—If the linear flow corresponds to the total system response, then the fracture permeability (smaller than that obtained using the induced linear interporosity flow) controls the well performance.

For a given stimulated reservoir geometry, the differences between the *induced linear interporosity flow* and the *total system response* are not only related to the well performance but also to the medium that controls the flow of fluids during the linear flow. In the induced linear interporosity flow, controlled by the matrix block properties, the fracture permeability plays a secondary role above a threshold value; in this case, the

matrix-to-fracture permeability ratio is low (ultra-low matrix permeability and high fracture permeability). In addition, the matrix permeability together with the matrix-block-size distribution, are the determinant features in the well performance. In the total system response, controlled by both fractures (permeability) and matrix blocks (storativity), the fracture permeability is the dominant parameter that influences the flow of fluids in the reservoir; in this case, the matrix-to-fracture permeability ratio is high (low matrix permeability and low fracture permeability).

We can conclude that the quality of the stimulated reservoir depends strongly on the matrix block-size distribution. The impact of the matrix block-size distribution depends on the flow regime, whose presence or absence is determined by the reservoir properties and the geometry of the stimulated volume. The overall well performance depends not only on the effective matrix-block size, but also on the specific values of r_{min} and r_{max}. It is reasonable to assume that r_{max} is mostly determined by the original reservoir state (before the stimulation treatment), and r_{min} is a more direct consequence of the stimulation treatment itself. Additional efforts are needed to infer the value of r_{min} and the shape of the matrix-block size dependence, possibly from microseismic and other fracture diagnostic data.

Because of the general behavior of production data in unconventional reservoirs (possible increasing trend at short time, flattening, transient linear flow, late transient linear flow, and possible BDS), the same reservoir signature can be reproduced with

different models, including other dual porosity models (even those with fixed block size) and even single porosity systems with built-in heterogeneities. However, the well performance extrapolation can be affected by the model chosen, leading to different estimated ultimate recoveries. The screening criteria to select a representative model must rely on an interdisciplinary approach gathering microseismic, geological, petrophysical, geomechanical, laboratory experiments, reservoir engineering, and other sources of information providing quantitative and qualitative description of the reservoir.

The current conceptualization enables us quantifying the effect of a consistent nonuniform matrix block distribution (after the fracturing treatment) with the minimum additional parameters. The new approach contributes to the understanding of production (and pressure) behavior of unconventional reservoirs to characterize the quality of the stimulated reservoir.

5. DESORPTION AND NON–LINEARITY CAUSED BY GAS FLOW *

5.1. Introduction

Many of the storage and flow mechanisms involved in unconventional reservoirs, such as adsorption, diffusion, slippage, natural fractures, spatially composite reservoir models and flow of real gases, have been already successfully incorporated into the traditional petroleum engineering toolkit.

Thus, several problems have been revisited with the advent of unconventional reservoirs. Many of them are old solutions that raised its importance because of the low permeability of the system. In this section, we address two important issues with the intent to provide a simple, yet clear understanding of the effect of desorption and non-linearity caused by flow of gases on the production performance in shale gas reservoirs.

---

*Part of this section is reprinted with permission from Fuentes-Cruz, G., Gildin, E., and Valkó, P.P. 2014. Capturing the Essence of Flow from Unconventional Reservoirs. *Hydraulic Fracturing Quarterly* **1** (01): 39–53. Copyright [2014] by Hydraulic Fracturing Quarterly journal.

5.2. Non-linearity caused by gas flow

The application of semi-analytical models in production data analysis is very common. Nevertheless, the underlying partial differential equation is non-linear, and several approaches have been proposed to linearize it. The common linearization technique is the use of pseudo-time, involving additional assumptions when applied to real cases, such as the square-root of time dependence of the distance of investigation.

For the single porosity idealization, the partial differential equation (PDE) of gas flow in real variables can be written as:

$$\nabla \cdot [k(y)\nabla \cdot m(p)] = \phi(\mu c_t)\frac{\partial m(p)}{\partial t} \quad \text{.....(5.1)}$$

Where the pseudopressure function is defined as (Al-Hussainy et al., 1966):

$$m(p) = 2\int_{p_{base}}^{p}\frac{p}{\mu z}dp \quad \text{.....(5.2)}$$

In pressure transient testing of gas reservoirs, where the duration of the tests is not usually long to reach pseudosteady state or in cases where the pressure drop p_i-p_{wf} is not high, the use of pseudopressure is enough for practical purposes.

The standard procedure in pressure transient testing and production data analysis is to evaluate the product (μc_t) at the initial reservoir pressure. Fraim and Wattenbarger

(1987) showed that the product (μc_t) can have a strong influence during the BDS; to overcome this issue, they suggested the use of the normalized time (or pseudo-time, Eq. 5.3), which transforms the non-linear PDE (Eq. 5.1) into a linear PDE (Eq. 5.4):

$$t_n = (\mu c_t)_i \int_0^t \frac{dt}{\mu(\tilde{p})c_t(\tilde{p})} \quad \text{.....(5.3)}$$

$$\nabla \cdot [k(y)\nabla \cdot m(p)] = \phi(\mu c_t)_i \frac{\partial m(p)}{\partial t_n} \quad \text{.....(5.4)}$$

Fraim and Wattenbarger (1987) suggested evaluating the integrand of the pseudo-time (Eq. 5.3) on the average reservoir pressure. Later, Anderson and Mattar (2007) suggested evaluating the integrand in the average pressure of the region of influence, to linearize the PDE not only during the BDS but also during the transient period.

Recently, Chen and Raghavan (2013) showed that if the product (μc_t) is evaluated at $0.6(p_i + p_w)$, then the analytical solution [linear, Eq. 5.1 with constant (μc_t)] and numerical solution (non-linear, Eq. 5.1) are in agreement during the linear flow (and well beyond the linear-flow period). We found that, for practical purposes, the product (μc_t) (or $\phi\mu c_t$) can be evaluated at the pressure corresponding to the arithmetic mean of $m(p_i)$ and $m(p_w)$. This pressure, denoted as p_{am}, is a good approximation of the average pressure in the region of influence during the transient linear flow.

In this section we investigate in detail four cases with the input data shown in **Tables 5.1 and 5.2**. The gas properties are the same as the synthetic example shown in Table 4.2 (section 4).

Table 5.1—Well and reservoir data. Synthetic cases	
k^0, md	1 x 10^{-3}
h, ft	306
ϕ_i , fraction	0.048
S_w , -	0.169
c_f , psi^{-1}	1 x 10^{-6}
p_i , psia	3115
p_{wf} , psia	500
$m(p_i)$, psi^2/cp	6.83 x 10^8
$m(p_{wf})$, psi^2/cp	2.08 x 10^7
T, °R	633.5
x_f , ft	400
y^*, ft	400
No. stages	3

Table 5.2—Data for synthetic cases 1 – 4			
	Skin factor	SR	Desorption
Case 1	0	1	No
Case 2	0.05	100	No
Case 3	0	100	Yes
Case 4	0.05	100	Yes

The numerical solutions presented in this work were obtained with an in-house numerical simulator; this is a 1D single porosity simulator with closed boundaries that solves equations 5.5 and 5.6 (field units) in a finite difference scheme:

$$\frac{\partial}{\partial y}\left[\frac{6.328x10^{-6}k(y)}{\mu B_g}\frac{\partial p}{\partial y}\right] = \frac{\partial(\phi S_g/B_g)}{1000\partial t} + \frac{\phi c_d}{1000B_g}\frac{\partial p}{\partial t} - q^*_{gsc} \quad \text{.....(5.5)}$$

$$0 = \frac{\partial(\phi S_w/B_w)}{1000\partial t} \quad (5.6)$$

Where B_f is the formation volume factor (f=gas, water) in rcf/scf, S_f if the phase saturation (f=gas, water), and q^*_{gsc} is the gas production rate at standard conditions per unit of rock volume (1000/D). The parameter c_d is the desorption compressibility (psi^{-1}):

$$c_d = \frac{\rho_B}{32.037}\frac{B_g V_m p_L}{\phi(p_L+p)^2} \quad (5.7)$$

where ρ_B is the matrix density (gm/cc), V_m is the Langmuir storage capacity (scf/ton), and p_L is Langmuir pressure (psia). The skin factor was added using Eq. 5.8 (field units):

$$q_{gsc} = \frac{n_{HF}k^0 h}{1423T}\frac{[m(p_b)-m(p_w)]}{\left[\frac{\pi}{2}\left(\frac{\Delta y - w_{HF}}{2x_f}\right)+s\right]} \quad (5.8)$$

where:

$$s = \frac{n_{HF}k^0 h}{1423T}\frac{[m(p_{wfideal})-m(p_w)]}{q_{gsc}} \quad (5.9)$$

p_b is the HF block pressure, p_w is the bottomhole pressure, Δy is the HF block width (in the y direction), w_{HF} is the HF width (assumed equal to zero). The HF block is the block (cell) of the mesh (in the finite difference scheme) that contains the hydraulic fracture.

The difference $\left[m(p_{wfideal}) - m(p_{wf})\right]$ is the additional pseudopressure drop characterized by a linear dependence on production rate. The remaining parameters in Eqs. 5.5 through 5.9 have been defined in section 2. Additionally, we use the following dimensionless variables:

$$q_{wD} = \frac{1423T}{n_{HF}k^0h[m(p_i)-m(p_{wf})]}q_{gsc} \quad \text{.....(5.10)}$$

$$t_D = \frac{0.006328k^0t}{(\phi\mu c_t)_{ref}x_f^2} \quad \text{.....(5.11)}$$

$$y_D^* = y^*/x_f \quad \text{.....(5.12)}$$

$$G_{pD} = \frac{9.004T}{n_{HF}(\phi\mu c_t)_{ref}x_f^2h[m(p_i)-m(p_{wf})]}G_p \quad \text{.....(5.13)}$$

The product $(\phi\mu c_t)_{ref}$ in Eqs. 5.11 and 5.13 will be evaluated at a specific pressure: the initial pressure (p_i) or the pressure corresponding to the arithmetic mean of $m(p_i)$ and $m(p_w)$ (denoted as p_{am}). **Fig. 5.1** compares the production behavior for the simulation case 1 (zero skin factor and uniform permeability field). The curves in Fig. 5.1A denote the following:

1. The analytical response coming from the solutions described in Appendix A (dotted line). This assumes that the product $(\phi\mu c_t)$ in Eq. 5.1 is

constant. The dimensionless variables are defined in Eqs. 5.10 through 5.12 (arbitrary reservoir properties).

2. The numerical solution: no assumptions made on $(\phi\mu c_t)$. The dimensionless production rate is plotted versus dimensionless pseudo-time [defined in Eq. 5.11, substituting t by t_n and taking $(\phi\mu c_t)$ at p_i]. The pseudo-time is calculated as suggested by Anderson and Mattar (2007): using the average pressure in the region of influence (Eq. 5.3).
3. Numerical solution. The dimensionless production rate is plotted versus dimensionless time. The product $(\phi\mu c_t)$ in Eq. 5.11 is evaluated at p_{am}.
4. Numerical solution. The dimensionless production rate is plotted versus dimensionless time. The product $(\phi\mu c_t)$ in Eq. 5.11 is evaluated at the initial reservoir pressure.

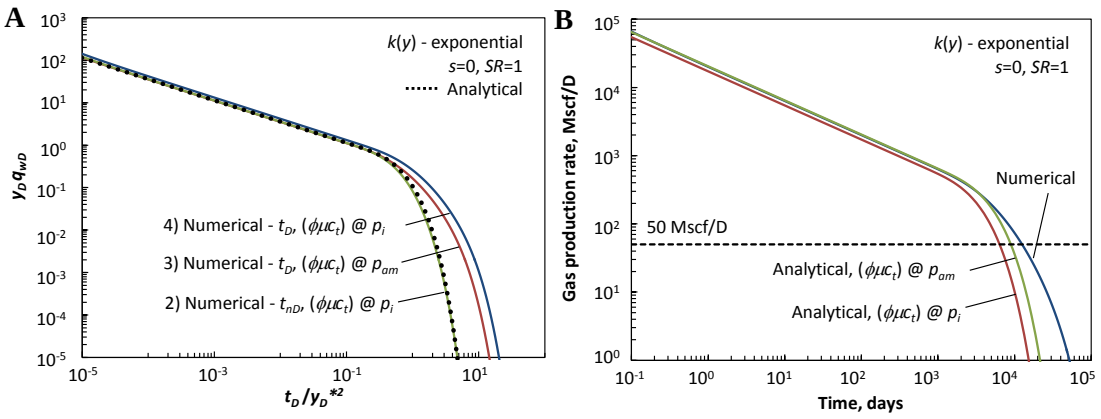

Fig. 5.1—Case 1. The differences between the analytical and the numerical solution are substantial in the BDS.

In Fig. 5.1A we observe that the numerical solution with pseudo-time collapses with the analytical solution in both, transient and BDS. The numerical solution as a function of time with $\phi\mu c_t \,@\, p_{am}$ is in good agreement with the analytical solution, but it departs from the analytical solution in the BDS. Additionally, the numerical solution versus time with $(\phi\mu c_t) \,@\, p_i$ is shifted during the transient period with respect to the analytical solution; it also departs from the analytical solution in the BDS. In Fig. 5.1B, we verify, in real variables, that the evaluation of $(\phi\mu c_t)$ at p_{am} is good enough during the transient and late transient period. These results are consistent with those found by Chen and Raghavan (2013).

As pointed out by Nobakht and Clarkson (2012) and Chen and Raghavan (2013), the average reservoir pressure in the region of influence is constant during the linear flow. According to the results in **Fig. 5.2** (case 1), during the transient linear flow (TLF) the average pressure in the area of influence ($p_{avg,ai}$) is constant and it collapses to the average pressure (p_{avg}) when a significant pressure drop occurs at the boundary of the SRV, leading to the BDS. Fig. 5.2B shows the dimensionless pseudo-pressure and dimensionless pressure evaluated at the average pressure in the region of influence (Eqs. 5.14 and 5.15):

$$m_D(p_{avg,ai}) = \frac{m(p_i) - m(p_{avg,ai})}{m(p_i) - m(p_{wf})} \quad \text{.....(5.14)}$$

$$p_{avg,aiD} = \frac{p_i - p_{avg,ai}}{p_i - p_{wf}} \quad \text{.....(5.15)}$$

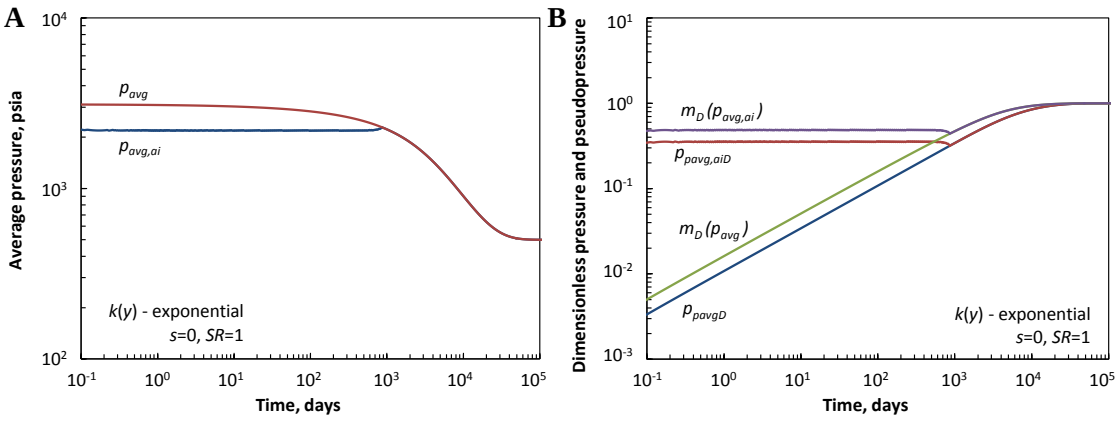

Fig. 5.2—Case 1. The average pressure in the area of influence is constant during the transient linear flow. During this flow period, the dimensionless pseudopressure at $p_{avg,ai}$ is equal to 0.5.

We note that $m_D(p_{avg,ai})$ is equal to 0.5 (Fig. 5.2B) during the TLF, with some variations around this value for different reservoir properties [for example, if we increase the initial pressure from 3115 psia to 7115 psia, then $m_D(p_{avg,ai}) = 0.44$]; this is valid if the skin factor is zero. In Eq. 5.16, α denotes the constant value of $m_D(p_{avg,ai})$ during the TLF:

$$m(p_{avg,ai}) = m(p_i) - \alpha[m(p_i) - m(p_{wf})] \quad \text{.....(5.16)}$$

If we take α=0.5, then $m(p_{avg,ai})$ is equal to the arithmetic mean between $m(p_i)$ and $m(p_w)$. This observation can be used to evaluate the product $(\phi\mu c_t)$ in Eq. 5.11 at the

pressure corresponding to the arithmetic mean of $m(p_i)$ and $m(p_w)$ when the analytical solution is used. This pressure, p_{am}, can be used as an approximation for $p_{avg,ai}$.

Fig. 5.3A shows the comparison between the analytical and numerical solutions for the simulation case 2 (non-zero skin factor and nonuniform permeability field). We observe that the numerical solution with pseudo-time follows the analytical solution. Also, the numerical solution as a function of the dimensionless time evaluated at p_{am} is in good agreement with the analytical response, showing a departure in the BDS. In this case, the permeability decreases with the distance to the HF in such a way that the time to reach a reasonable economic limit (50 Mscf/D) is beyond 10,000 days. This means that, during the productive life of this well, the difference between the analytical and numerical solutions is small as shown in Fig. 5.3B.

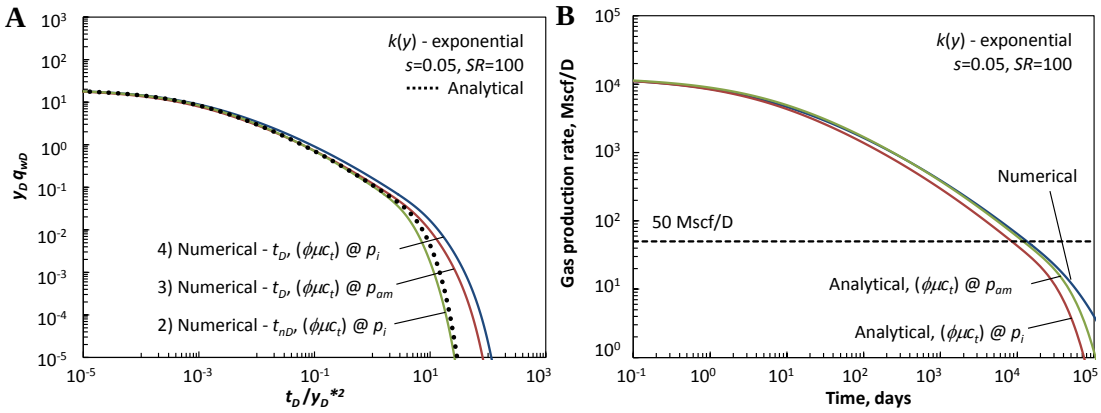

Fig. 5.3—Case 2. Numerical and analytical responses of nonuniform reservoirs with skin factor. These solutions are in agreement during the productive life of wells producing in shale-gas reservoirs.

In relation to case 2, **Fig. 5.4A** shows that the average pressure in the region of influence ($p_{avg,ai}$) is no longer constant during the transient period: at short times, it tends to the average pressure (i.e., to the initial reservoir pressure) because of skin factor effects; in the late transient period it shows a decreasing trend because of the effects of the nonuniform permeability field. Then, it collapses with the average pressure (p_{avg}) when the boundary is reached. In this case, the dimensionless pseudopressure and the dimensionless pressure are not constant (Fig. 5.4B), yet the analytical solution with ($\phi\mu c_t$) at p_{am} provides good accuracy to approach the numerical solution as we already verified in Fig. 5.3B.

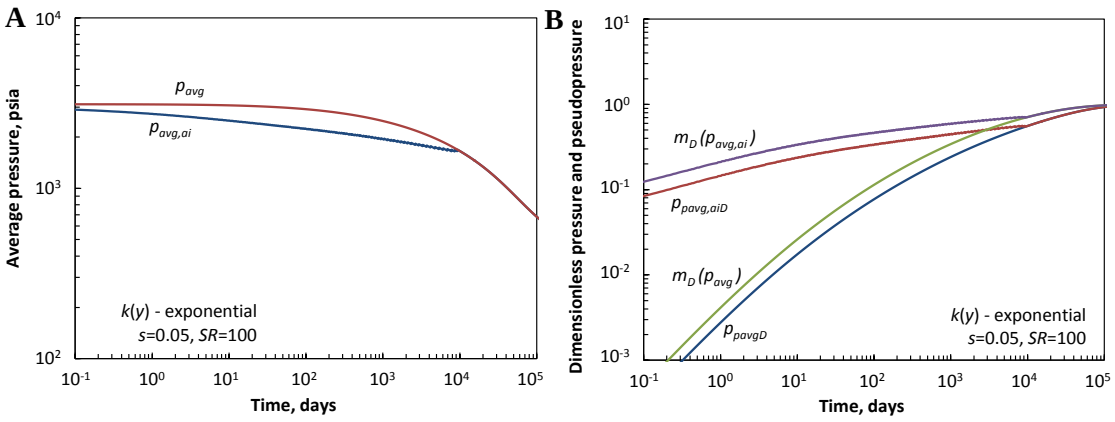

Fig. 5.4—Case 2. The average pressure in the area of influence is no longer constant during the transient period. At short times, it tends to the initial pressure because of skin factor effects. In the late transient period, it is not constant because of nonuniform permeability effects. Even in these circumstances, the analytical solution with ($\phi\mu c_t$) at p_{am} offers a good approximation.

In Figs. 5.1 through 5.4, the average pressure in the region (area) of influence was calculated from the data generated in the simulation process; we calculated the region inside of which there is more than some fraction of the total pressure drop:

$$\frac{p_i - p(y_{influence}, t)}{p_i - p_{wf}} > \xi \quad \text{.....(5.17)}$$

We considered ξ=0.08 in the simulations shown in this work. The depth of investigation (d_{inv}) is the maximum distance to the HF that fulfills Eq. 5.17 for a given time. In other words, it is half-length (in the *y* direction) of the area of influence in the SRV element (Fig. 2.1). The relative depth of investigation is defined as:

$$d_{inv(rel)} = \frac{d_{inv}}{y^*} \quad \text{.....(5.18)}$$

Fig. 5.5A shows that the relative depth of investigation depends on the square-root of time only during the transient linear flow. For zero skin factor and uniform permeability (10^{-3} md) the pressure takes around 12 days to influence 10% of the SRV element, and around 350 days to influence 50%. It takes 860 days to reach the boundary. This is an optimistic case because the permeability does not deteriorate; it keeps the same (relatively high) value throughout the SRV. If we consider zero skin factor and *SR*=100, then the times to reach 10, 50, and 100% of the SRV are 15, 820, and 9200 days,

respectively. More than 25 years to reach the BDS; this might exceed the economic life of the well.

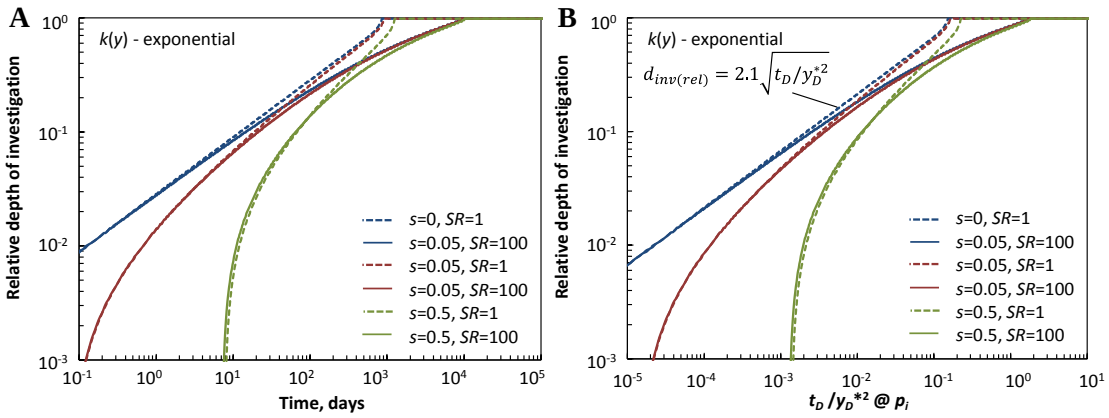

Fig. 5.5—The depth of investigation is proportional to the square-root of time only during the transient linear flow. The presence of skin factor destroys the square-root-of-time relation.

For constant pressure production, the skin factor affects the pressure profile and the average reservoir pressure in the area of influence (Fig. 5.4A). As a result, the depth of investigation is influenced by the skin factor and the square-root-of-time relation is no longer valid, as it is shown in Fig 5.5. Some methodologies that use the concept of pseudo-time during the transient period assume that the square-root of time relation is valid. Thus, the analyst should be cautious when applying pseudo-time techniques in transient conditions because field data usually show evidence of skin factor in the production performance.

In Fig. 5.5B we show the same data of Fig. 5.5A, but now as a function of dimensionless time with properties evaluated at the initial pressure.

Based on several simulations, we found that the following relation keeps for the relative depth of investigation during the transient linear flow in uniform reservoirs:

$$d_{inv(rel)} = 2.1\sqrt{\frac{t_D @ p_i}{y_D^{*2}}} \quad \text{.....(5.19)}$$

The depth of investigation in real variables is (field units):

$$d_{inv} = 0.17\sqrt{\frac{k^0 t}{(\phi\mu c_t)_{p_i}}} \quad \text{.....(5.20)}$$

This relation is in agreement with the standard equation of distance of investigation (El-Banbi and Wattenbarger, 1998).

5.3. Desorption

The common way to add desorption is by using the Langmuir isotherm:

$$V_a = \frac{\rho_B}{32.037}\frac{V_m p}{p_L + p} \quad \text{.....(5.21)}$$

From mass conservation, Bumb and McKee (1988) showed that desorption translates as an additional compressibility:

$$c_d = \frac{\rho_B}{32.037}\frac{B_g V_m p_L}{\phi(p_L+p)^2} \quad \text{.....(5.22)}$$

Thus, desorption compressibility should be added to the total compressibility. In this work, we tested the following expression of compressibility to compare the results using the analytical solution to the numerical simulation results:

$$c_t = S_g c_g + S_w c_w + c_d + c_r, @\, p_{am} \quad \text{.....(5.23)}$$

The terms depending on pressure (c_g, c_w, c_d) are evaluated at p_{am} (c_r is considered constant). The dominant terms in Eq. 5.23 are $S_g c_g$ and c_d. We considered the following Langmuir parameters for Barnett shale (Mengal and Wattenbarger, 2011): V_m=96 scf/ton, ρ_B=2.38 gm/cc, and p_L=650 psi.

Fig. 5.6 shows case 3 (zero skin factor, nonuniform reservoir, desorption included) in log-log and semi-log format to highlight the good approach of the analytical solution at short and long times, provided that the total compressibility is evaluated at p_{am}. We note that desorption process does not destroy the linear signature in unconventional reservoirs. The significant differences evolve during the BDS, but reaching this stage can take a long time because of the low permeability in shale and its deterioration.

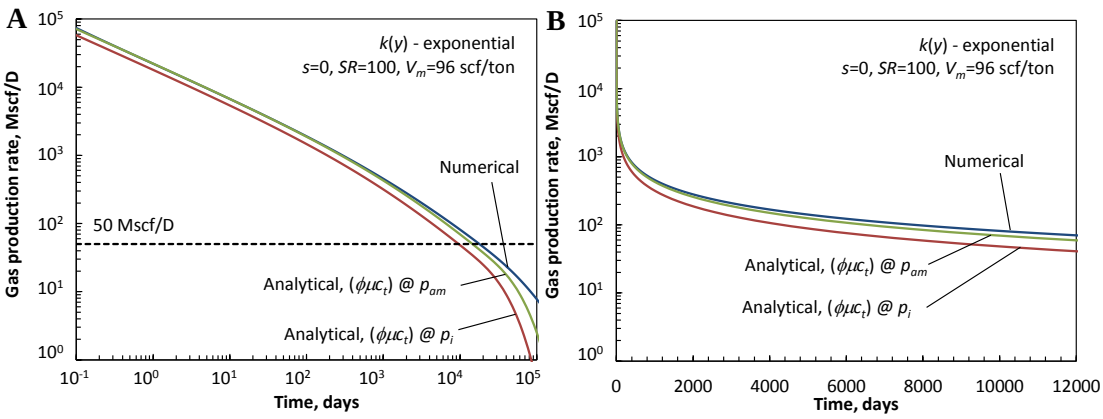

Fig. 5.6—Case 3. The analytical solution approaches the numerical solution when desorption is included, provided that the total compressibility (in the analytical solution) is evaluated at p_{am}.

Even in the presence of skin factor (case 4 in **Fig. 5.7A**); the analytical solution represents a good approximation to the numerical solution. If we look closer to the short time behavior of Fig. 5.7A, the analytical solution that collapses with the numerical solution is the one with $(\phi\mu c_t)$ at p_i (Fig. 5.7B). This is because, as shown in Fig. 5.4A of case 2, in the presence of skin factor the average pressure in the area of influence tends to the average pressure at short times, which is equal to the initial pressure at the beginning of production. After this short period, the numerical solution tends to the analytical solution with $(\phi\mu c_t)$ at p_{am}. This fact is not of significant consequences because it happens at short times and the differences are small compared to the common scattering of real production data.

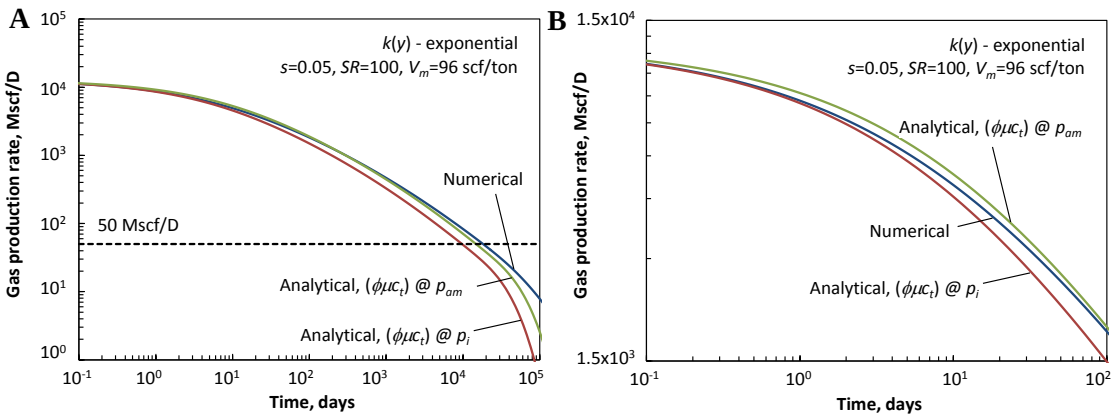

Fig. 5.7—Case 4. In the presence of skin factor, the analytical solution is also a good approximation to the numerical response, provided that the total compressibility (in the analytical solution) is evaluated at p_{am}. At very short time, the numerical response collapses with the analytical solution with $(\phi\mu c_t)$ at p_i.

5.4. Analysis of field data

This example, Well 5, was analyzed in section 2 with the single porosity formulation of the induced permeability field using the analytical models and taking the product $(\phi\mu c_t)$ at p_i in the definition of dimensionless time. The general data were shown in table 2.1 and the fluid properties in Table 4.2.

Fig. 5.8 shows that the model with induced permeability field (exponential dependency) fits very well the production history, even in the initial increasing trend of production rate versus time, corresponding to the values between 1 and 2 in the dimensionless group. **Table 5.3** shows that the maximum induced permeability (k^0) is less than the one obtained using the product $(\phi\mu c_t)$ at p_i. The overestimation of permeability [when using $(\phi\mu c_t)$ at p_i] has been reported in the literature (Ibrahim and Wattenbarger 2006). The estimation of the stimulation ratio (and therefore the threshold permeability) is strongly

affected by the $(\phi\mu c_t)$ product; it is more than 6 times greater than that obtained when $(\phi\mu c_t)$ is evaluated at the initial pressure, leading to a smaller threshold permeability ($4x10^{-6}$ md). These results indicate that the permeability in the boundary of the SRV element can be in the same order of magnitude as the formation or matrix permeability.

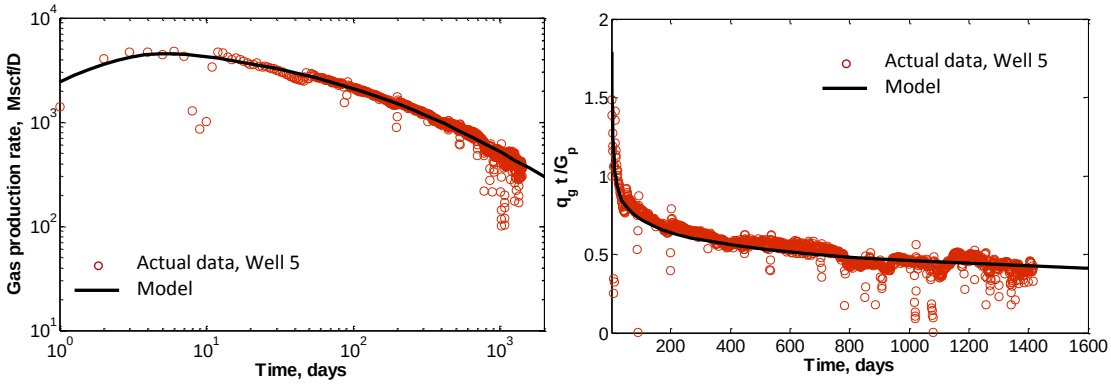

Fig. 5.8—Production data analysis of Well 5 using the induced permeability field concept (exponential dependency). The model offers a good match throughout the overall production history.

Table 5.3—Comparison of results obtained with $(\phi\mu c_t)$ at p_{am} and p_i

	$(\phi\mu c_t)$ @ p_{am}	$(\phi\mu c_t)$ @ p_i
k^0, md	$1.9x10^{-3}$	$2.8x10^{-3}$
k^*, md	$4.0x10^{-6}$	$3.9x10^{-05}$
SR	480	72
skin	0.22	0.31
τ	1.7	1.7
EUR_{20yr},bcf	2.4	2.4

The skin factor is less than the one using p_i as a consequence of the reduction of the maximum permeability. The mean lifetime (τ) was not affected by the $(\phi\mu c_t)$ correction.

Even when we have an estimation of the HF half-length from other sources, we can consider a sensitivity analysis to the HF half-length and compare the consistency with other sources of data. For example, if x_f is assumed 300 ft, then k^0=0.0034 md, k*=3.3x10^{-5} md (SR=102), and s=0.385.

The main observation from analyzing field data is that the TLF and BDS are not separated sharply. Instead, we have a *slowing down* of ever increasing actual drained volume, filling out the physically available space more and more but never perfectly. In some respect this can be considered as the very essence of flow from unconventional reservoirs, while all the other significant conditions/phenomena, such as double porosity medium, desorption, slippage, non-linearity of gas flow, drainage geometry determined by the multiple fractures intersecting the horizontal well, choke effect at the fracture-well intersection, non-Darcy flow at bottleneck locations, etc. have been already identified and modeled in more traditional settings.

6. CONCLUSIONS AND FUTURE RESEARCH

The following conclusions are derived from the study of the induced permeability field in the one-porosity idealization:

- Production decline curves for fracture-stimulated reservoirs with induced nonuniform permeability differ significantly from the uniform case, reflecting an often neglected additional effect of the hydraulic fracture treatment.
- The new approach justifies the use of the uniform permeability model during the transient linear flow even if the permeability field is nonuniform (exponential or linear dependency). It also emphasizes the uncertain departure from the transient linear flow at intermediate and late times, and hence alerts to use caution in the production forecast and SRV characterization.
- Field data analyses indicate that the induced permeability distribution can be described as an exponential or linear function of the distance to the fracture plane, with only moderate difference in the final conclusions. The maximum and minimum induced permeabilities may provide the key to evaluate overall completion efficiency in unconventional formations, where the extent and quality of the SRV are equally significant.
- The new model generalizes the analogous ones for uniform permeability and explains commonly occurring production characteristics of today's intensively stimulated (and mostly unconventional) reservoirs.

- Because most of the recoverable hydrocarbon is produced under transient conditions in shale systems, the based-time analytical solutions can be used to perform the production data analysis, provided that the product $(\phi\mu c_t)$ is evaluated at the pressure corresponding to the arithmetic mean between $m(p_i)$ and $m(p_{wf})$.

Based on the discussion on the decaying wellbore pressure approach and the induced permeability field in the double-porosity/double-permeability idealization, we conclude the following:

- The new approach generalizes the induced permeability field concept to the dual-porosity idealization to account for a nonuniform fracture permeability distribution that originates from the intensive stimulation treatment.
- If the interporosity flow coefficient (λ) is small, then the dimensionless threshold permeability ($\hat{k}_{fD}^{*}$) affects the transition between the transient linear flow in the fractures and the interporosity linear flow. If λ is large, then $\hat{k}_{fD}^{*}$ controls the late-transient period and BDS.
- The common behavior of the bottomhole flowing pressure observed in unconventional reservoirs can be modeled analytically by using the concept of decaying wellbore pressure, which confirms that the diagnostic of flow regimes can be performed in the log-log plot of production rate versus time.

- The inclusion of the decaying wellbore pressure approach (in the single and double porosity/double permeability models) enables characterizing new flow regimes during the increasing trend of production rate at short times, leading to a set of straight lines whose slopes depend on flow regime in the reservoir, fluid and reservoir properties, skin factor, and the mean lifetime of the bottomhole flowing pressure decay.
- The ratio between the production time and material balance time ($q_w t/G_p$) enables identifying the characteristic signatures of flow regimes in a practical manner, avoiding excessive manipulation of data. It is especially useful in identifying the departure from the transient linear and bilinear flows.
- It seems that a simple characterization of the non-uniform permeability field ($\hat{k}_f^0/\hat{k}_f^*$) within the single porosity framework provides already the most useful information regarding the effectiveness of the stimulation of the unconventional reservoir.

The following conclusions are made from the study of the induced interporosity-flow field:

- The new approach generalizes the uniform matrix-block-size model to account for a nonuniform matrix-block distribution whose size depends on the distance to the main hydraulic fracture planes. In this approach, the matrix blocks are not

distributed randomly because they do not represent the original geologic setting; they are altered by the massive stimulation treatment.

- The new model preserves the typical signature (linear flow) of commonly observed production behavior of unconventional shale reservoirs by accounting for a high density of micro-fractures near the HFs. The closely spaced micro-fractures have a strong impact on well performance, even when they do not propagate throughout the whole stimulated reservoir.
- A high density of micro-fractures, interpreted as small matrix-block dimensions, leads to a high matrix-fracture contact area, the key controlling factor that enhances the transfer of fluids from the (ultra-tight to tight) matrix blocks to the fracture network.
- The general linear flow observed in unconventional reservoirs is affected by the matrix-block distribution depending on the type of linear flow: the total system response (high matrix-to-fracture permeability ratio) or the induced linear interporosity flow (small matrix-to-fracture permeability ratio).
- During the total system response, the smallest matrix-block size controls not only the starting time of the linear flow but also the bilinear flow previous to it. Once the linear flow starts, the block-size distribution plays a secondary role.
- During the induced linear interporosity flow, the matrix-block distribution strongly affects the well performance, which is controlled by the logarithmic mean of the minimum and maximum matrix-block sizes.

Based on the results obtained in this research, the following future work is suggested:

- Probabilistic inversion of a well-production model for Shale gas developments. A probabilistic description of a vector of parameters required to predict production on a shale gas well can be retrieved by the use of the Bayesian paradigm and production data. The quantification of the uncertainties corresponding to the effects of determinant properties can be performed by using a probabilistic approach.
- Calibrate the results from numerical simulation with the semi-analytical models to include complex geometry and multi-phase conditions, such as the simultaneous production of gas, oil, and water.
- Investigate the power-law dependency in linear geometries of multi-fractured horizontal wells. Power law-functions are commonly related to fractal theory (the use of concepts of diffusion on fractal-like structures that leads to anomalous diffusion). The fractal models work well when the permeability cross-sectional area product experienced by a fluid mass is decreasing as the fluid approaches the well. However, after the fracturing treatment, the fluid mass experiences increasing permeability cross-sectional area product while approaching the hydraulic fracture.

NOMENCLATURE

Variables:

B	formation volume factor, RB/Mscf
c	compressibility, psi^{-1}
d_{inv}	depth of investigation, ft
$d_{inv(rel)}$	relative depth of investigation, dimensionless
EUR_{20yr}	20-years estimated ultimate recovery, bcf
G_p	cumulative gas, MMscf
h	formation thickness, ft
k^0	maximum induced permeability, md
k^*	threshold permeability, md
$\hat{k}_f$	bulk-facture permeability, md
$\hat{k}_f^0$	maximum induced bulk-facture permeability, md
$\hat{k}_f^*$	threshold bulk-fracture permeability, md
$\hat{k}_m$	bulk-matrix permeability, md
$k(y)$	permeability function, md
L_j	width of medium *j* (*j*=*f* or *m*), ft
λ	dimensionless interporosity-flow coefficient
λ_{r_w}	dimensionless interporosity-flow coefficient based on r_w

$\lambda(y)$	dimensionless interporosity-flow-coefficient function
$m(p)$	pseudopressure, psi^2/cp
n_f	number of fractures (natural and induced)
n_{HF}	number of main hydraulic-fracture planes
N_p	cumulative oil, STB
p	pressure, psi
p_L	Langmuir pressure, psia
p_{wf}	bottomhole flowing pressure, psi
$p_{wf,stab}$	stabilized bottomhole flowing pressure, psi
q	production flowrate, Mscf/D or STB/D
r_m	radius of matrix block, ft
$r_m(y)$	matrix-block radius function, ft
ρ_B	matrix density, gm/cc
ρ_f	linear fracture density, #fractures/ft
s	skin factor, dimensionless
S	saturation, fraction
SR	stimulation ratio, dimensionless
σ	matrix shape factor, ft^{-2}
t	time, days
T	absolute temperature, °R
τ	mean lifetime, days
u	Laplace-space variable

x_e	effective reservoir width, ft
x_f (= x_{HF})	effective hydraulic-fracture half-length, ft
y^*	half-length of SRV element, ft
μ	viscosity, cp
ϕ	porosity, fraction
$\hat{\phi}$	bulk porosity, fraction
V	volume, ft^3
V_a	adsorbed gas content, scf/rcf
V_m	Langmuir storage capacity, scf/ton
ω	dimensionless fracture storativity

Subscripts:

avg	average
avg,ai	average in the area (region) of influence
b	bilinear
cp	constant wellbore pressure
cr	constant wellbore rate
d	desorption
D	dimensionless
eff	effective
f	fractures

g	gas
i	initial
ITA	intermediate-time approximation
l	linear
m	matrix
n	normalized
M	match (from type curve matching)
max	maximum
min	minimum
r	rock
ref	reference
sc	standard conditions
ST	short time
STA	short-time approximation
t	total
w	well or water
wf	flowing pressure

Abbreviations:

BDS	boundary-dominated state
CWP	constant wellbore pressure

DWP	decaying wellbore pressure
FR	fractured reservoirs
HF	hydraulic fracture
MFHW	multi-fractured horizontal well
NFR	naturally fractured reservoirs
PSS	pseudosteady state
REV	representative elementary volume
SRE	stimulated reservoir element
SRV	stimulated reservoir volume
TLF	transient linear flow

REFERENCES

Abdassah, D. and Ershaghi, I. 1986. Triple-Porosity Systems for Representing Naturally Fractured Reservoirs. *SPE Formation Evaluation* **1** (2): 113-127. http://dx.doi.org/10.2118/13409-PA.

Agarwal, R.G., Al-Hussainy, R., and Ramey, H.J., Jr. 1970. An Investigation of Wellbore Storage and Skin Effect in Unsteady Liquid Flow: I. Analytical Treatment. *SPE Journal* **10** (03): 279 - 290. http://dx.doi.org/10.2118/2466-PA.

Ajani, A.A. and Kelkar, M.G. 2012. Interference Study in Shale Plays. Paper SPE 151045 presented at the SPE Hydraulic Fracturing Technology Conference, The Woodlands, Texas, USA, 6-8 February. http://dx.doi.org/10.2118/151045-MS.

Akkutlu, I.Y. and Fathi, E. 2012. Multiscale Gas Transport in Shales with Local Kerogen Heterogeneities. *SPE Journal* **17** (04): 1002 - 1011. http://dx.doi.org/10.2118/146422-PA.

Al-Hussainy, R., Ramey H.J. Jr., and Crawford, P.B. 1966. The Flow of Real Gases through Porous Media. *Journal of Petroleum Technology* **18** (5): 624-636. http://dx.doi.org/10.2118/1243-A-PA.

Al Rbeawi, S.J.H. and Tiab, D. 2012. Productivity Index and Inflow Performance of Hydraulically Fractured Formations. Paper SPE 159687 presented at the SPE Annual Technical Conference and Exhibition, San Antonio, Texas, USA, 8-10 October. http://dx.doi.org/10.2118/159687-MS.

Anderson, D.M. and Mattar, L. 2007. An Improved Pseudo-Time for Gas Reservoirs with Significant Transient Flow. *Journal of Canadian Petroleum Technology* **46** (07): 49-54. http://dx.doi.org/10.2118/07-07-05.

Arps, J.J. 1944. Analysis of Decline Curves. *Trans., AIME* **160**: 228-247.

Barenblatt, G.I., Zheltov, I.P., and Kochina, I.N. 1960. Basic Concepts on the Theory of Seepage of Homogeneous Liquids in Fissured Rocks (Strata). *PMM* **24** (5): 852-864.

Barker, J.A. 1988. A Generalized Radial Flow Model for Hydraulic Tests in Fractured Rock. *Water Resources Research* **24** (10): 1796-1804. http://dx.doi.org/10.1029/WR024i010p01796.

Beier, R.A. 1994. Pressure-Transient Model for a Vertically Fractured Well in a Fractal Reservoir. *SPE Formation Evaluation* **9** (2): 122-128. http://dx.doi.org/10.2118/20582-PA.

Bello, R.O. 2009. Transient Analysis in Shale Gas Reservoirs with Transient Linear Behavior. PhD Dissertation, Texas A&M University, College Station, Texas, May.

Bello, R.O. and Wattenbarger, R.A. 2010. Multi-Stage Hydraulically Fractured Horizontal Shale Gas Well Rate Transient Analysis. Paper SPE 126754 presented at the North Africa Technical Conference and Exhibition, Cairo, Egypt, 14-17 February. http://dx.doi.org/10.2118/126754-MS.

Blasingame, T.A., McCray, T.L., and Lee, W.J. 1991. Decline Curve Analysis for Variable Pressure Drop/Variable Flowrate Systems. Paper SPE 21513 presented at the SPE Gas Technology Symposium, Houston, Texas, USA, 22-24 January. http://dx.doi.org/10.2118/21513-MS.

Bohacs, K.M., Passey, Q.R., Rudnicki, M. et al. 2013. The Spectrum of Fine-Grained Reservoirs from 'Shale Gas' to 'Shale Oil'/Tight Liquids: Essential Attributes, Key Controls, Practical Characterization. Paper IPTC 16676 presented at the International Petroleum Technology Conference, Beijing, China, 26-28 March. http://dx.doi.org/10.2523/16676-MS.

Brown, M., Ozkan, E., Raghavan, R. et al. 2011. Practical Solutions for Pressure-Transient Responses of Fractured Horizontal Wells in Unconventional Shale

Reservoirs. *SPE Reservoir Evaluation & Engineering* **14** (06): 663 - 676. http://dx.doi.org/10.2118/125043-PA.

Bumb, A.C. and McKee, C.R. 1988. Gas-Well Testing in the Presence of Desorption for Coalbed Methane and Devonian Shale. *SPE Formation Evaluation* **3** (01): 179 - 185. http://dx.doi.org/10.2118/15227-PA.

Camacho Velazquez, R., Fuentes-Cruz, G., and Vasquez-Cruz, M.A. 2008. Decline-Curve Analysis of Fractured Reservoirs with Fractal Geometry. *SPE Reservoir Evaluation & Engineering* **11** (3): 606-619. http://dx.doi.org/10.2118/104009-PA.

Carlson, B.C. 1972. The Logarithmic Mean. *The American Mathematical Monthly* **79** (6): 615-618. http://www.jstor.org/stable/2317088.

Chang, J. and Yortsos, Y.C. 1990. Pressure-Transient Analysis of Fractal Reservoirs. *SPE Formation Evaluation* **5** (1): 31-38. http://dx.doi.org/10.2118/18170-PA.

Chen, C. and Raghavan, R. 2013. On the Liquid-Flow Analog to Evaluate Gas Wells Producing in Shales. *SPE Reservoir Evaluation & Engineering* **16** (02): 209 - 215. http://dx.doi.org/10.2118/165580-PA.

Cinco-Ley, H., Samaniego V, F., and Kucuk, F. 1985. The Pressure Transient Behavior for Naturally Fractured Reservoirs with Multiple Block Size. Paper SPE 14168 presented at the SPE Annual Technical Conference and Exhibition, Las Vegas, Nevada, USA, 22-26 September. http://dx.doi.org/10.2118/14168-MS.

Cipolla, C.L., Lolon, E., and Mayerhofer, M.J. 2009. Resolving Created, Propped, and Effective Hydraulic-Fracture Length. *SPE Production & Operations* **24** (4): 619-628. http://dx.doi.org/10.2118/129618-PA.

Clarkson, C.R. 2013. Production Data Analysis of Unconventional Gas Wells: Review of Theory and Best Practices. *International Journal of Coal Geology* **109–110** (0): 101-146. http://dx.doi.org/10.1016/j.coal.2013.01.002.

Clarkson, C.R. and Williams-Kovacs, J. 2013. Modeling Two-Phase Flowback of Multifractured Horizontal Wells Completed in Shale. *SPE Journal* **18** (04): 795 - 812. http://dx.doi.org/10.2118/162593-PA.

Dake, L.P. 1978. *Fundamentals of Reservoir Engineering*. Elsevier. ISBN: 978-0-444-41830-2.

de Swaan O., A. 1976. Analytic Solutions for Determining Naturally Fractured Reservoir Properties by Well Testing. *SPE Journal* **16** (3): 117-122. http://dx.doi.org/10.2118/5346-PA.

Dershowitz, W. and Miller, I. 1995. Dual Porosity Fracture Flow and Transport. *Geophysical Research Letters* **22** (11): 1441-1444. DOI: 10.1029/95gl01099.

Doublet, L.E., Pande, P.K., McCollum, T.J. et al. 1994. Decline Curve Analysis Using Type Curves--Analysis of Oil Well Production Data Using Material Balance Time: Application to Field Cases. Paper SPE 28688 presented at the International Petroleum Conference and Exhibition of Mexico, Veracruz, Mexico, 10-13 October. http://dx.doi.org/10.2118/28688-MS.

El-Banbi, A., H. and Wattenbarger, R.A. 1998. Analysis of Linear Flow in Gas Well Production. Paper SPE 39972 presented at the SPE Gas Technology Symposium, Calgary, Alberta, Canada, 15-18 March. http://dx.doi.org/10.2118/39972-MS.

Fetkovich, M.J. 1980. Decline Curve Analysis Using Type Curves. *SPE Journal of Petroleum Technology* **32** (6): 1065-1077. http://dx.doi.org/10.2118/4629-PA.

Fisher, M.K., Wright, C.A., Davidson, B.M. et al. 2005. Integrating Fracture Mapping Technologies to Improve Stimulations in the Barnett Shale. *SPE Production & Facilities* **20** (02): 85 - 93. http://dx.doi.org/10.2118/77441-PA.

Fraim, M.L. and Wattenbarger, R.A. 1987. Gas Reservoir Decline-Curve Analysis Using Type Curves with Real Gas Pseudopressure and Normalized Time. *SPE Formation Evaluation* **2** (4): 671-682. http://dx.doi.org/10.2118/14238-PA.

Fu, P., Johnson, S.M., and Carrigan, C.R. 2013. An Explicitly Coupled Hydro-Geomechanical Model for Simulating Hydraulic Fracturing in Arbitrary Discrete Fracture Networks. *International Journal for Numerical and Analytical Methods in Geomechanics* **37** (14): 2278-2300. http://dx.doi.org/10.1002/nag.2135.

Fuentes-Cruz, G., Camacho Velazquez, R., and Vasquez-Cruz, M.A. 2010. A Unified Approach for Falloff and Buildup Tests Analysis Following a Short Injection/Production Time. Paper SPE 133539 presented at the SPE Western Regional Meeting, Anaheim, California, USA, 27-29 May. http://dx.doi.org/10.2118/133539-MS.

Fuentes-Cruz, G., Gildin, E., and Valkó, P.P. 2014a. Analyzing Production Data from Hydraulically Fractured Wells: The Concept of Induced Permeability Field. SPE

Reservoir Evaluation & Engineering **17** (02): 220 - 232. http://dx.doi.org/10.2118/163843-PA.

Fuentes-Cruz, G., Gildin, E., and Valkó, P.P. 2014b. Capturing the Essence of Flow from Unconventional Reservoirs. *Hydraulic Fracturing Quarterly* (now *Hydraulic Fracturing Journal*) **1** (01): 39 – 53.

Fuentes-Cruz, G., Gildin, E., and Valkó, P.P. 2014c. On the Analysis of Production Data: Practical Approaches for Hydraulically Fractured Wells in Unconventional Reservoirs. *Journal of Petroleum Science and Engineering* **119** (0): 54-68. http://dx.doi.org/10.1016/j.petrol.2014.04.012.

Gale, J.F.W. and Holder, J. 2010. Natural Fractures in Some US Shales and Their Importance for Gas Production. *Geological Society, London, Petroleum Geology Conference Series* **7**: 1131-1140. http://dx.doi.org/10.1144/0071131.

Gale, J.F.W., Reed, R.M., and Holder, J. 2007. Natural Fractures in the Barnett Shale and Their Importance for Hydraulic Fracture Treatments. *AAPG Bulletin* **91** (04): 603-622. http://dx.doi.org/10.1306/11010606061.

Ge, J. and Ghassemi, A. 2011. Permeability Enhancement in Shale Gas Reservoirs after Stimulation by Hydraulic Fracturing. Paper ARMA-11-514 presented at the 45th

U.S. Rock Mechanics/Geomechanics Symposium, San Francisco, CA, USA, 26-29 June. 11-514.

Gu, H., Weng, X., Lund, J.B. et al. 2011. Hydraulic Fracture Crossing Natural Fracture at Non-Orthogonal Angles, a Criterion, Its Validation and Applications. Paper SPE 139984 presented at the SPE Hydraulic Fracturing Technology Conference, The Woodlands, Texas, USA, 24-26 January. http://dx.doi.org/10.2118/139984-MS.

Hagoort, J. 2011. Semisteady-State Productivity of a Well in a Rectangular Reservoir Producing at Constant Rate or Constant Pressure. *SPE Reservoir Evaluation & Engineering* **14** (6): 677-686. http://dx.doi.org/10.2118/149807-PA.

Helmy, M.W. and Wattenbarger, R.A. 1998. New Shape Factors for Wells Produced at Constant Pressure. Paper SPE 39970 presented at the SPE Gas Technology Symposium, Calgary, Alberta, Canada, 15-18 March. http://dx.doi.org/10.2118/39970-MS.

Hummel, N. and Shapiro, S.A. 2013. Nonlinear Diffusion-Based Interpretation of Induced Microseismicity: A Barnett Shale Hydraulic Fracturing Case Study. *Geophysics* **78** (5): B211-B226. http://dx.doi.org/10.1190/geo2012-0242.1.

Hurst, W. 1934. Unsteady Flow of Fluids in Oil Reservoirs. *Physics* **5** (1): 20-30.

Ibrahim, M. and Wattenbarger, R.A. 2006. Rate Dependence of Transient Linear Flow in Tight Gas Wells. *Journal of Canadian Petroleum Technology* **45** (10): 18-20. http://dx.doi.org/10.2118/06-10-TN2.

Jeffrey, R.G., Zhang, X., and Thiercelin, M.J. 2009. Hydraulic Fracture Offsetting in Naturally Fractures Reservoirs: Quantifying a Long-Recognized Process. Paper SPE 119351 presented at the SPE Hydraulic Fracturing Technology Conference, The Woodlands, Texas, USA, 19-21 January. http://dx.doi.org/10.2118/119351-MS.

Johns, R.T. and Jalali, Y. 1991. Comparison of Pressure-Transient Response in Intensely and Sparsely Fractured Reservoirs. *SPE Formation Evaluation* **6** (04): 513 - 518. http://dx.doi.org/10.2118/18800-PA.

Kanfar, M., Alkouh, A.B., and Wattenbarger, R.A. 2013. Modeling Guidelines for Analyzing and Forecasting Shale Well Performance. Paper SPE 165698 presented at the SPE Eastern Regional Meeting, Pittsburgh, Pennsylvania, USA, 20-22 August. http://dx.doi.org/10.2118/165698-MS.

Kazemi, H. 1969. Pressure Transient Analysis of Naturally Fractured Reservoirs with Uniform Fracture Distribution. *SPE Journal* **9** (4): 451-462. http://dx.doi.org/10.2118/2156-A.

King, G.E. 2010. Thirty Years of Gas Shale Fracturing: What Have We Learned? Paper SPE 133456 presented at the SPE Annual Technical Conference and Exhibition, Florence, Italy, 19-22 September. http://dx.doi.org/10.2118/133456-MS.

King, G.R. and Ertekin, T. 1991. State-of-the-Art Modeling for Unconventional Gas Recovery. *SPE Formation Evaluation* **6** (01): 63 - 71. http://dx.doi.org/10.2118/18947-PA.

Kuchuk, F. and Biryukov, D. 2014. Pressure-Transient Behavior of Continuously and Discretely Fractured Reservoirs. *SPE Reservoir Evaluation & Engineering* **17** (01): 82 - 97. http://dx.doi.org/10.2118/158096-PA.

Larsen, L. and Hegre, T.M. 1991. Pressure-Transient Behavior of Horizontal Wells with Finite-Conductivity Vertical Fractures. Paper SPE 22076 presented at the International Arctic Technology Conference, Anchorage, Alaska, 29-31 May. http://dx.doi.org/10.2118/22076-MS.

Lorenz, J.C., Sterling, J.L., Schechter, D.S. et al. 2002. Natural Fractures in the Spraberry Formation, Midland Basin, Texas: The Effects of Mechanical Stratigraphy on Fracture Variability and Reservoir Behavior. *AAPG Bulletin* **86** (3): 505-524. http://dx.doi.org/10.1306/61EEDB20-173E-11D7-8645000102C1865D.

Marhaendrajana, T., Blasingame, T.A., and Rushing, J.A. 2004. Use of Production Data Inversion to Evaluate Performance of Naturally Fractured Reservoirs. Paper SPE 90013 presented at the SPE Annual Technical Conference and Exhibition, Houston, Texas, USA, 26-29 September. http://dx.doi.org/10.2118/90013-MS.

Marquardt, D. 1963. An Algorithm for Least-Squares Estimation of Nonlinear Parameters. *Journal of the Society for Industrial and Applied Mathematics* **11** (2): 431-441. http://dx.doi.org/10.1137/0111030.

Maxwell, S.C., Urbancic, T.I., Steinsberger, N. et al. 2002. Microseismic Imaging of Hydraulic Fracture Complexity in the Barnett Shale. Paper SPE 77440 presented at the SPE Annual Technical Conference and Exhibition, San Antonio, Texas, USA, 29 September-2 October. http://dx.doi.org/10.2118/77440-MS.

Mayerhofer, M.J., Lolon, E., Warpinski, N.R. et al. 2010. What Is Stimulated Reservoir Volume? *SPE Production & Operations* **25** (1): 89-98. http://dx.doi.org/10.2118/119890-PA.

Mayerhofer, M.J., Lolon, E.P., Youngblood, J.E. et al. 2006. Integration of Microseismic-Fracture-Mapping Results with Numerical Fracture Network Production Modeling in the Barnett Shale. Paper SPE 102103 presented at the SPE

Annual Technical Conference and Exhibition, San Antonio, Texas, USA, 24-27 September. http://dx.doi.org/10.2118/102103-MS.

Mengal, S.A. and Wattenbarger, R.A. 2011. Accounting for Adsorbed Gas in Shale Gas Reservoirs. Paper SPE 141085 presented at the SPE Middle East Oil and Gas Show and Conference, Manama, Bahrain, 25-28 September. http://dx.doi.org/10.2118/141085-MS.

Meyer, B.R., Bazan, L.W., Jacot, R.H. et al. 2010. Optimization of Multiple Transverse Hydraulic Fractures in Horizontal Wellbores. Paper SPE 131732 presented at the SPE Unconventional Gas Conference, Pittsburgh, Pennsylvania, USA, 23-25 February. http://dx.doi.org/10.2118/131732-MS.

Mirzaei, M. and Cipolla, C.L. 2012. A Workflow for Modeling and Simulation of Hydraulic Fractures in Unconventional Gas Reservoirs. Paper SPE 153022 presented at the SPE Middle East Unconventional Gas Conference and Exhibition, Abu Dhabi, UAE, 23-25 January. http://dx.doi.org/10.2118/153022-MS.

Mohaghegh, S.D. 2013. Reservoir Modeling of Shale Formations. *Journal of Natural Gas Science and Engineering* **12** (0): 22-33. http://dx.doi.org/10.1016/j.jngse.2013.01.003.

Mukherjee, H. and Economides, M.J. 1991. A Parametric Comparison of Horizontal and Vertical Well Performance. *SPE Formation Evaluation* **6** (02): 209 - 216. http://dx.doi.org/10.2118/18303-PA.

Mullen, J. 2010. Petrophysical Characterization of the Eagle Ford Shale in South Texas. Paper SPE 138145 presented at the Canadian Unconventional Resources and International Petroleum Conference, Calgary, Alberta, Canada, 19-21 October. http://dx.doi.org/10.2118/138145-MS.

Nobakht, M. and Clarkson, C.R. 2012. A New Analytical Method for Analyzing Linear Flow in Tight/Shale Gas Reservoirs: Constant-Flowing-Pressure Boundary Condition. *SPE Reservoir Evaluation & Engineering* **15** (03): 370 - 384. http://dx.doi.org/10.2118/143989-PA.

Nobakht, M. and Mattar, L. 2012. Analyzing Production Data from Unconventional Gas Reservoirs with Linear Flow and Apparent Skin. *Journal of Canadian Petroleum Technology* **51** (01): 52 - 59. http://dx.doi.org/10.2118/137454-PA.

Olson, J.E. and Taleghani, A.D. 2009. Modeling Simultaneous Growth of Multiple Hydraulic Fractures and Their Interaction with Natural Fractures. Paper SPE 119739 presented at the SPE Hydraulic Fracturing Technology Conference, The Woodlands, Texas, USA, 19-21 January. http://dx.doi.org/10.2118/119739-MS.

Ozkan, E., Brown, M.L., Raghavan, R. et al. 2011. Comparison of Fractured-Horizontal-Well Performance in Tight Sand and Shale Reservoirs. *SPE Reservoir Evaluation & Engineering* **14** (02): 248 - 259. http://dx.doi.org/10.2118/121290-PA.

Palmer, I.D., Moschovidis, Z.A., and Cameron, J.R. 2007. Modeling Shear Failure and Stimulation of the Barnett Shale after Hydraulic Fracturing. Paper SPE 106113 presented at the SPE Hydraulic Fracturing Technology Conference, College Station, Texas, USA, 29-31 January. http://dx.doi.org/10.2118/106113-MS.

Poon, D. 1995. Transient Pressure Analysis of Fractal Reservoirs. Paper PETSOC-95-34 presented at the 46th Annual Technical Meeting of CIM, Banff, Alberta, Canada, June 7 - 9. http://dx.doi.org/10.2118/95-34.

Raghavan, R.S., Chen, C.-C., and Agarwal, B. 1997. An Analysis of Horizontal Wells Intercepted by Multiple Fractures. *SPE Journal* **02** (03): 235-245. http://dx.doi.org/10.2118/27652-PA.

Ramurthy, M., Barree, R.D., Kundert, D.P. et al. 2011. Surface-Area Vs. Conductivity-Type Fracture Treatments in Shale Reservoirs. *SPE Production & Operations* **26** (04): 357 - 367. http://dx.doi.org/10.2118/140169-PA.

Ranjbar, E., Hassanzadeh, H., and Chen, Z. 2012. One-Dimensional Matrix-Fracture Transfer in Dual Porosity Systems with Variable Block Size Distribution. *Transport in Porous Media* **95** (1): 185-212. http://dx.doi.org/10.1007/s11242-012-0039-4.

Renshaw, C.E. and Pollard, D.D. 1995. An Experimentally Verified Criterion for Propagation Across Unbounded Frictional Interfaces in Brittle, Linear Elastic Materials. *International Journal of Rock Mechanics and Mining Sciences & Geomechanics Abstracts* **32** (3): 237-249. http://dx.doi.org/10.1016/0148-9062(94)00037-4.

Shapiro, A.M. 1987. Transport Equations for Fractured Porous Media. *Advances in Transport Phenomena in Porous Media*, NATO ASI Series: Springer Netherlands **128**: 405-471. http://dx.doi.org/10.1007/978-94-009-3625-6_10.

Sharifi Haddad, A., Hassanzadeh, H., and Abedi, J. 2012. Advective–Diffusive Mass Transfer in Fractured Porous Media with Variable Rock Matrix Block Size. *Journal of Contaminant Hydrology* **133** (0): 94-107. http://dx.doi.org/10.1016/j.jconhyd.2012.02.008.

Suarez-Rivera, R., Chertov, M., Willberg, D.M. et al. 2012. Understanding Permeability Measurements in Tight Shales Promotes Enhanced Determination of Reservoir

Quality. Paper SPE 162816 presented at the SPE Canadian Unconventional Resources Conference, Calgary, Alberta, Canada, 30 October-1 November. http://dx.doi.org/10.2118/162816-MS.

Tivayanonda, V., Apiwathanasorn, S., Economides, C. et al. 2012. Alternative Interpretations of Shale Gas/Oil Rate Behavior Using a Triple Porosity Model. Paper SPE 159703 presented at the SPE Annual Technical Conference and Exhibition, San Antonio, Texas, USA, 8-10 October. http://dx.doi.org/10.2118/159703-MS.

Torcuk, M.A., Kurtoglu, B., Alharthy, N. et al. 2013. Analytical Solutions for Multiple Matrix in Fractured Reservoirs: Application to Conventional and Unconventional Reservoirs. *SPE Journal* **18** (05): 969 - 981. http://dx.doi.org/10.2118/164528-PA.

Valkó, P.P. and Abate, J. 2004. Comparison of Sequence Accelerators for the Gaver Method of Numerical Laplace Transform Inversion. *Computers & Mathematics With Applications* **48** (3–4): 629-636. http://dx.doi.org/10.1016/j.camwa.2002.10.017.

Van Everdingen, A.F. and Hurst, W. 1949. The Application of the Laplace Transformation to Flow Problems in Reservoirs. *Trans., AIME* **186**: 305-324. http://dx.doi.org/10.2118/949305-G.

Wang, J. and Liu, Y. 2011. Simulation Based Well Performance Modeling in Haynesville Shale Reservoir. Paper SPE 142740 presented at the SPE Production and Operations Symposium, Oklahoma City, Oklahoma, USA, 27-29 March. http://dx.doi.org/10.2118/142740-MS.

Warpinski, N.R., Mayerhofer, M., Agarwal, K. et al. 2013. Hydraulic-Fracture Geomechanics and Microseismic-Source Mechanisms. *SPE Journal* **18** (4): 766-780. http://dx.doi.org/10.2118/158935-PA.

Warpinski, N.R. and Teufel, L.W. 1987. Influence of Geologic Discontinuities on Hydraulic Fracture Propagation. *Journal of Petroleum Technology* **39** (02): 209 - 220. http://dx.doi.org/10.2118/13224-PA.

Warren, J.E. and Root, P.J. 1963. The Behavior of Naturally Fractured Reservoirs. *SPE Journal* **3** (3): 245-255. http://dx.doi.org/10.2118/426-PA.

Wattenbarger, R.A., El-Banbi, A.H., Villegas, M.E. et al. 1998. Production Analysis of Linear Flow into Fractured Tight Gas Wells. Paper SPE 39931 presented at the SPE Rocky Mountain Regional/Low-Permeability Reservoirs Symposium, Denver, Colorado, 5-8 April 1998. http://dx.doi.org/10.2118/39931-MS.

Wolfram Research, Inc. 2012. *Mathematica,* Version 9.0, Champaign, Illinois.

Wuestefeld, A., Urbancic, T.I., Baig, A. et al. 2012. A Decade Monitoring Shale Gas Plays Using Microseismicity: Advances in the Understanding of Hydraulic Fracturing. Paper SPE 159892 presented at the SPE Annual Technical Conference and Exhibition, San Antonio, Texas, USA, 8-10 October. http://dx.doi.org/10.2118/159892-MS.

Zhou, J., Chen, M., Jin, Y. et al. 2008. Analysis of Fracture Propagation Behavior and Fracture Geometry Using a Tri-Axial Fracturing System in Naturally Fractured Reservoirs. *International Journal of Rock Mechanics and Mining Sciences* **45** (7): 1143-1152. http://dx.doi.org/10.1016/j.ijrmms.2008.01.001.

APPENDIX A

INDUCED PERMEABILITY FIELD MODEL – 1ϕ

Solution for constant production rate

Fig. A-1 shows the conceptual model in dimensionless notation:

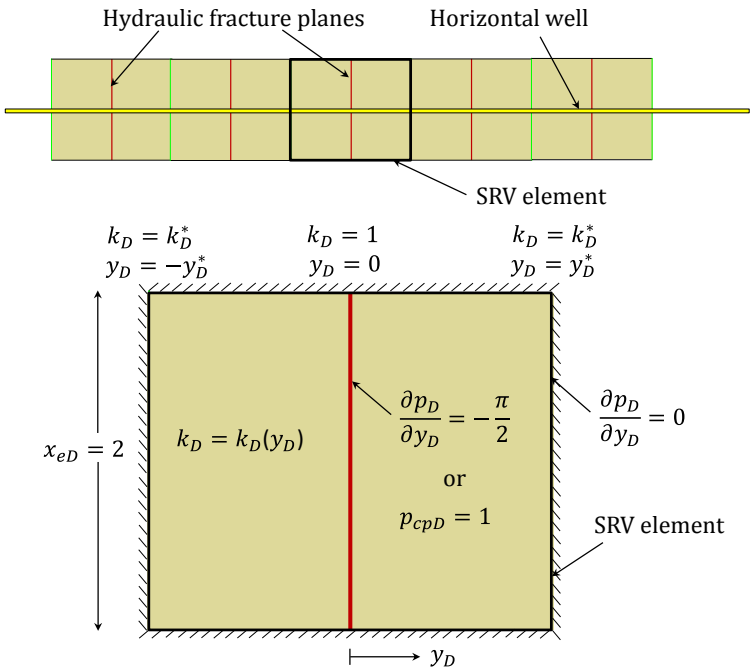

Fig. A-1—Plain view of a fracture-stimulated reservoir. Induced permeability field in the single-porosity idealization.

The mathematical model in terms of dimensionless variables reads:

$$\frac{\partial}{\partial y_D}\left[k_D(y_D)\frac{\partial p_D}{\partial y_D}\right] = \frac{\partial p_D}{\partial t_D}; 0 \le y_D \le y_D^* \quad \text{(A-1)}$$

$$p_D(y_D, t_D = 0) = 0 \quad \text{(A-2)}$$

$$\left(\frac{\partial p_D}{\partial y_D}\right)_{y_D=0} = -\frac{\pi}{2} \quad \text{(A-3)}$$

$$\left(\frac{\partial p_D}{\partial y_D}\right)_{y_D=y_D{}^*} = 0 \quad \text{(A-4)}$$

where:

$$p_D = \frac{\pi n_{HF} T_{sc} k^0 h[m(p_i) - m(p)]}{q_w p_{sc} T} : gas \quad \text{(A-5a)}$$

$$p_D = \frac{2\pi n_{HF} k^0 h(p_i - p)}{q_w B \mu} : oil \quad \text{(A-5b)}$$

$$t_D = \frac{k^0 t}{(\phi \mu c_t)_i x_f^2} : gas \quad \text{(A-6a)}$$

$$t_D = \frac{k^0 t}{\phi \mu c_t x_f^2} : oil \quad \text{(A-6b)}$$

$$y_D = y/x_f \quad \text{(A-7)}$$

$$k_D(y_D) = k(y)/k^0 = k_D^{*(y_D/y_D^*)} = e^{(lnk_D^*) y_D / y_D^*} : exponetial \quad \text{(A-8)}$$

$$k_D(y_D) = k(y)/k^0 = 1 + (k_D^* - 1)(y_D/y_D^*): linear \quad \text{(A-9)}$$

$$k_D^* = k^*/k^0 \quad \text{(A-10)}$$

$m(p)$ is the pseudopressure function (Al-Hussainy et al. 1966). The wellbore pressure solution in Laplace space for exponential permeability field is:

$$\bar{p}_{wD} = \frac{\delta\pi}{2u\sqrt{u}}\left[\frac{I_1\left(\frac{2y_D^*\sqrt{u}}{ln(\xi)}\right)K_0\left(\frac{2y_D^*}{ln(\xi)}\sqrt{\frac{u}{k_D^*}}\right)+I_0\left(\frac{2y_D^*}{ln(\xi)}\sqrt{\frac{u}{k_D^*}}\right)K_1\left(\frac{2y_D^*\sqrt{u}}{ln(\xi)}\right)}{I_0\left(\frac{2y_D^*\sqrt{u}}{ln(\xi)}\right)K_0\left(\frac{2y_D^*}{ln(\xi)}\sqrt{\frac{u}{k_D^*}}\right)-I_0\left(\frac{2y_D^*}{ln(\xi)}\sqrt{\frac{u}{k_D^*}}\right)K_0\left(\frac{2y_D^*\sqrt{u}}{ln(\xi)}\right)}\right] \quad \text{(A-11)}$$

If $k_D^* < 1, \delta = -1$ and $\xi = 1/k_D^*$; if $k_D^* > 1, \delta = 1$ and $\xi = k_D^*$. The corresponding pressure solution for linear permeability field is:

$$\bar{p}_{wD} = \frac{\delta\pi}{2u\sqrt{u}}\left[\frac{I_1\left(\frac{2y_D^*\sqrt{k_D^*u}}{|k_D^*-1|}\right)K_0\left(\frac{2y_D^*\sqrt{u}}{|k_D^*-1|}\right)+I_0\left(\frac{2y_D^*\sqrt{u}}{|k_D^*-1|}\right)K_1\left(\frac{2y_D^*\sqrt{k_D^*u}}{|k_D^*-1|}\right)}{I_1\left(\frac{2y_D^*\sqrt{k_D^*u}}{|k_D^*-1|}\right)K_1\left(\frac{2y_D^*\sqrt{u}}{|k_D^*-1|}\right)-I_1\left(\frac{2y_D^*\sqrt{u}}{|k_D^*-1|}\right)K_1\left(\frac{2y_D^*\sqrt{k_D^*u}}{|k_D^*-1|}\right)}\right] \quad \text{(A-12)}$$

If $k_D^* < 1, \delta = -1$; if $k_D^* > 1, \delta = 1$. For uniform permeability ($k_D^* = 1$):

$$\bar{p}_{wD} = \frac{\pi}{2u\sqrt{u}}coth(y_D^*\sqrt{u}) \quad \text{(A-13)}$$

Where I_ν and K_ν are the modified Bessel functions of first and second kind, respectively ($\nu = 0,1$). $\bar{p}_{wD}$ is the Laplace transform of p_{wD} and u is the Laplace variable of t_D. The definition of dimensionless PI (constant wellbore rate) is:

$$J_{crD} = \frac{1}{p_{wD} - 2\pi t_D \left(\frac{1/4}{y_D^*}\right)} \quad \text{(A-14)}$$

Solution for constant wellbore flowing pressure

The mathematical model for constant wellbore pressure is similar to Eqs. A-1 through A-10, except the inner boundary condition:

$$p_{cpD}(y_D = 0, t_D) = 1 \quad \text{(A-15)}$$

Where p_{cpD} is the dimensionless pseudopressure (or pressure):

$$p_{cpD} = \frac{m(p_i) - m[p(y,t)]}{m(p_i) - m(p_{wf})} : gas \quad \text{(A-16a)}$$

$$p_{cpD} = \frac{p_i - p(y,t)}{p_i - p_{wf}} : oil \quad \text{(A-16b)}$$

By using the Convolution theorem (van Everdingen and Hurst 1949), the dimensionless production rate is:

$$\bar{q}_{wD} = \frac{1}{u^2 \bar{p}_{wD}} \quad \text{(A-17)}$$

Where $\bar{q}_{wD}$ is the Laplace transform of production rate (constant wellbore pressure) and $\bar{p}_{wD}$ is the wellbore pressure (constant rate solution, Eqs. A-11 through A-13). The definitions of dimensionless production rate, cumulative production, and dimensionless PI (constant wellbore pressure) are:

$$q_{wD} = \frac{p_{sc}T}{\pi n_{HF} T_{sc} k^0 h[m(p_i) - m(p_{wf})]} q_g : gas \quad \text{(A-18a)}$$

$$q_{wD} = \frac{B\mu}{2\pi n_{HF} k^0 h(p_i - p_{wf})} q_o : oil \quad \text{(A-18b)}$$

$$G_{pD} = \frac{p_{sc}T}{\pi n_{HF} T_{sc} (\phi \mu c_t)_i x_f^2 h[m(p_i) - m(p_{wf})]} G_p : gas \quad \text{(A-19a)}$$

$$N_{pD} = \frac{B}{2\pi n_{HF} \phi c_t x_f^2 h(p_i - p_{wf})} N_p : oil \quad \text{(A-19b)}$$

$$J_{cpD} = \frac{q_{wD}}{\left(1 - \frac{\pi G_{pD}}{2y_D^*}\right)} : gas \quad \text{(A-20a)}$$

$$J_{cpD} = \frac{q_{wD}}{\left(1 - \frac{\pi N_{pD}}{2y_D^*}\right)} : oil \quad \text{(A-20b)}$$

Asymptotic approximations for production rate and PI

Short-time approximation for production rate (exponential, linear, and uniform model):

$$q_{wD-STA} = \frac{2}{\pi}\sqrt{\frac{1}{\pi t_D}} \quad \text{(A-21)}$$

Total recoverable hydrocarbon:

$$N_{pD-MAX} = \frac{2y_D^*}{\pi} \quad \text{(A-22)}$$

Long-time approximation of dimensionless PI when the well is flowing at constant wellbore pressure ($J_{cpD-BDS}$). For exponential permeability field, $J_{cpD-BDS}$ is the first root of:

$$J_1\left(\frac{\sqrt{2\pi y_D^* J_{cpD-BDS}}}{ln(\xi)}\right)Y_0\left(\frac{\sqrt{2\pi y_D^* J_{cpD-BDS}/k_D^*}}{ln(\xi)}\right) -$$

$$J_0\left(\frac{\sqrt{2\pi y_D^* J_{cpD-BDS}/k_D^*}}{ln(\xi)}\right)Y_1\left(\frac{\sqrt{2\pi y_D^* J_{cpD-BDS}}}{ln(\xi)}\right) = 0 \quad \text{(A-23)}$$

Where $\xi = 1/k_D^* \ if \ k_D^* < 1$; $\xi = k_D^* \ if \ k_D^* > 1$. J_ν and Y_ν are the Bessel functions of first and second kind, respectively ($\nu = 0,1$). $J_{cpD-BDS}$ for linear permeability field is the first root of:

$$J_1\left(\frac{\sqrt{2\pi k_D^* y_D^* J_{cpD-BDS}}}{|1-k_D^*|}\right)Y_0\left(\frac{\sqrt{2\pi y_D^* J_{cpD-BDS}}}{|1-k_D^*|}\right)-$$

$$J_0\left(\frac{\sqrt{2\pi y_D^* J_{cpD-BDS}}}{|1-k_D^*|}\right)Y_1\left(\frac{\sqrt{2\pi k_D^* y_D^* J_{cpD-BDS}}}{|1-k_D^*|}\right)=0 \quad \text{(A-24)}$$

$J_{cpD-BDS}$ for uniform permeability field:

$$J_{cpD-BDS}=\frac{\pi}{2y_D^*} \quad \text{(A-25)}$$

Long-time approximation of dimensionless PI when the well is flowing at constant wellbore rate ($J_{crD-PSS}$). For exponential permeability field:

$$J_{crD-PSS}=\frac{2k_D^* ln^3(k_D^*)}{\pi y_D^*(2k_D^*+k_D^* ln^2(k_D^*)-2k_D^* ln(k_D^*)-2)} \quad \text{(A-26)}$$

$J_{crD-PSS}$ for linear permeability field:

$$J_{crD-PSS}=\frac{4(k_D^*-1)^3}{\pi y_D^*(-3{k_D^*}^2+2{k_D^*}^2 ln(k_D^*)+4k_D^*-1)} \quad \text{(A-27)}$$

$J_{crD-PSS}$ for uniform permeability field:

$$J_{crD-PSS} = \frac{6}{\pi y_D^*} \quad \text{(A-28)}$$

Solutions including skin factor

The convolution theorem (van Everdingen and Hurst 1949) facilitates inclusion of the skin factor effect in Laplace space:

$$\bar{p}_{wDs} = \bar{p}_{wD} + s/u \quad \text{(A-29)}$$

Where $\bar{p}_{wDs}$ is the pressure solution (constant production rate) including skin factor and $\bar{p}_{wD}$ is the zero-skin solution (Eqs. A-11 through A-13). The corresponding production rate (constant wellbore pressure) in Laplace space is:

$$\bar{q}_{wDs} = \frac{1}{u^2 \bar{p}_{wDs}} \quad \text{(A-30)}$$

Thus, the short-time approximation of production rate in time domain is (s > 0) (Bello 2009):

$$q_{wDs-STA} = \frac{1}{s} \quad \text{(A-31)}$$

APPENDIX B

INDUCED PERMEABILITY FIELD MODEL – 2ϕ (CWP)

Fracture and matrix equations

The model description is presented in **Fig. B-1:**

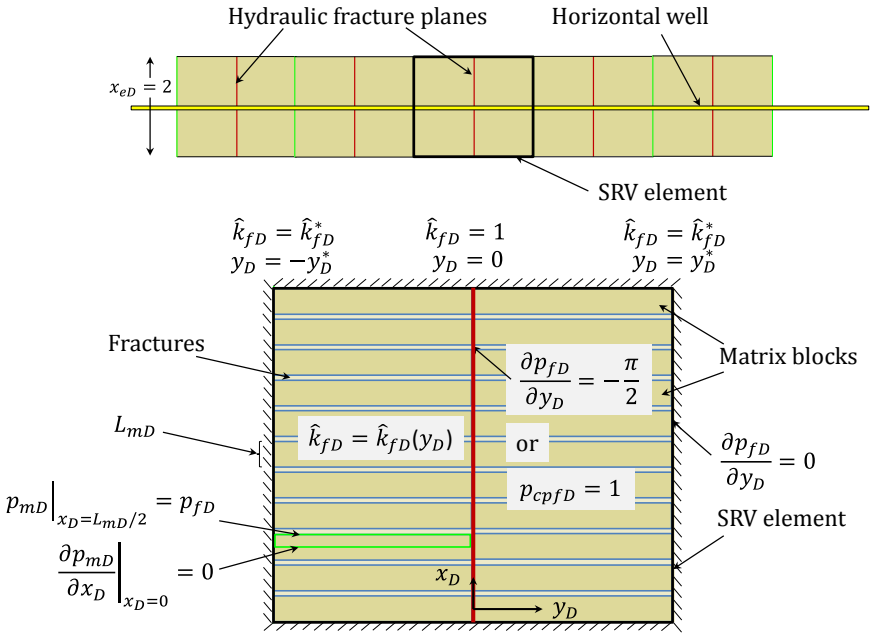

Fig. B-1—Plain view of a massively-stimulated FR. Induced permeability field in the double-porosity/double permeability idealization.

The mathematical model for the fracture system and matrix blocks reads:

$$\frac{\partial}{\partial y_D}\left[\hat{k}_{fD}(y_D)\frac{\partial p_{fD}}{\partial y_D}\right] - q_{mfD} = \omega\frac{\partial p_{fD}}{\partial t_D}; 0 < y_D < y^*_D \quad \text{(B-1)}$$

$$p_{fD}(y_D, t_D = 0) = 0 \quad \text{(B-2)}$$

$$\left(\frac{\partial p_{fD}}{\partial y_D}\right)_{y_D=0} = -\frac{\pi}{2} \quad \text{(B-3)}$$

$$\left(\frac{\partial p_{fD}}{\partial y_D}\right)_{y_D=y_D{}^*} = 0 \quad \text{(B-4)}$$

$$\frac{\partial^2 p_{mD}}{\partial x_D^2} = \alpha^2 \frac{\partial p_{mD}}{\partial t_D}; 0 < x_D < L_{mD}/2 \quad \text{(B-5)}$$

$$p_{mD}(x_D, t_D = 0) = 0 \quad \text{(B-6)}$$

$$\left(\frac{\partial p_{mD}}{\partial x_D}\right)_{x_D=0} = 0 \quad \text{(B-7)}$$

$$p_{mD}(L_{mD}/2, t_D) = p_{fD} \quad \text{(B-8)}$$

where:

$$p_{jD} = \frac{\pi n_{HF} T_{sc} \hat{k}_f^0 h[m(p_i) - m(p_j)]}{q_w p_{sc} T} : gas; (\, j = f \; or \; m) \quad \text{(B-9a)}$$

$$p_{jD} = \frac{2\pi n_{HF} \hat{k}_f^0 h(p_i - p_j)}{q_w B \mu} : oil; \;\; (\, j = f \; or \; m) \quad \text{(B-9b)}$$

$$t_D = \frac{\hat{k}_f^0 t}{(\widehat{\phi_f c_{tf}} + \widehat{\phi_m c_{tm}})_i \mu_i x_f^2} = \frac{\hat{k}_f^0 t}{(\hat{\phi}_f c_{tf} + \hat{\phi}_m c_{tm})_i \mu_i x_f^2} : gas \quad \text{(B-10a)}$$

$$t_D = \frac{\hat{k}_f^0 t}{(\widehat{\phi_f c_{tf}} + \widehat{\phi_m c_{tm}})\mu x_f^2} = \frac{\hat{k}_f^0 t}{(\hat{\phi}_f c_{tf} + \hat{\phi}_m c_{tm})\mu x_f^2} : oil \quad \text{(B-10b)}$$

$$y_D = y/x_f \quad \text{(B-11)}$$

$$y_D^* = y^*/x_f \quad \text{(B-12)}$$

$$x_D = x/x_f \quad \text{(B-13)}$$

$$L_{mD} = L_m/x_f \quad \text{(B-14)}$$

$$\hat{k}_{fD}(y_D) = \hat{k}_f(y)/\hat{k}_f^0 = \hat{k}_{fD}^{*\,(y_D/y_D^*)} = e^{\left(ln\hat{k}_{fD}^*\right)y_D/y_D^*} : exponetial \quad \text{(B-15)}$$

$$\hat{k}_{fD}(y_D) = \hat{k}_f(y)/\hat{k}_f^0 = 1 + \left(\hat{k}_{fD}^* - 1\right)(y_D/y_D^*) : linear \quad \text{(B-16)}$$

$$\hat{k}_{fD}^* = \hat{k}_f^*/\hat{k}_f^0 \quad \text{(B-17)}$$

$$q_{mfD} = \frac{2\pi x_f^2 h q_{mf}^*}{q_w B} \quad \text{(B-18)}$$

$$\omega = \frac{\widehat{\phi_{fi} c_{tfi}}}{\widehat{\phi_{fi} c_{tfi}} + \widehat{\phi_{mi} c_{tmi}}} = \frac{\hat{\phi}_{fi} c_{tfi}}{\hat{\phi}_{fi} c_{tfi} + \hat{\phi}_{mi} c_{tmi}} \quad \text{(B-19)}$$

$$\alpha^2 = (1 - \omega) \frac{\hat{k}_f^0}{\hat{k}_m} \quad \text{(B-20)}$$

$m(p)$ is the pseudopressure function (Al-Hussainy et al. 1966). q_{mf}^* is the volumetric rate of fluid from matrix to natural fractures per unit of bulk volume. Thus,

$$q_{mfD} = \frac{2\hat{k}_m}{L_{mD} \hat{k}_f^0} \left(\frac{\partial p_{mD}}{\partial x_D} \right)_{x_D = L_{mD}/2} \quad \text{(B-21)}$$

The matrix equation and boundary conditions in Laplace space are:

$$\frac{d^2 \bar{p}_{mD}}{dx_D^2} = \alpha^2 u \bar{p}_{mD}; 0 < x_D < L_{mD}/2 \quad \text{(B-22)}$$

$$\left(\frac{d\bar{p}_{mD}}{dx_D} \right)_{x_D = 0} = 0 \quad \text{(B-23)}$$

$$\bar{p}_{mD}(L_{mD}/2) = \bar{p}_{fD} \quad \text{(B-24)}$$

In Eq. B-22 we assume that the initial distribution of matrix pressure is uniform. $\bar{p}_{jD}$ is the Laplace transform of p_{jD} ($j = f, m$) and u is the Laplace variable of t_D. The solution of Eqs. B-22 through B-24 is:

$$\bar{p}_{mD}(x_D) = \frac{cosh(\sqrt{u}\alpha x_D)}{cosh(\sqrt{u}\alpha L_{mD}/2)}\bar{p}_{fD}(y_D) \quad \text{(B-25)}$$

Hence,

$$\left(\frac{d\bar{p}_{mD}}{dx_D}\right)_{x_D=L_{mD}/2} = \sqrt{u}\ \alpha\ tanh\left(\frac{L_{mD}}{2}\alpha\sqrt{u}\right)\bar{p}_{fD}(y_D) \quad \text{(B-26)}$$

Substituting Eq. B-20 into B-26:

$$\left(\frac{d\bar{p}_{mD}}{dx_D}\right)_{x_D=L_{mD}/2} = \frac{L_{mD}}{2}\frac{k_f^0}{k_m}\sqrt{\frac{\lambda(1-\omega)u}{3}}tanh\left(\sqrt{\frac{3(1-\omega)u}{\lambda}}\right)\bar{p}_{fD}(y_D) \quad \text{(B-27)}$$

where:

$$\lambda = \frac{12}{L_m^2}\frac{\hat{k}_m}{\hat{k}_f^0}x_f^2 \quad \text{(B-28)}$$

Substituting Eq. B-27 into the Laplace transform of B-21:

$$\bar{q}_{mfD} = \sqrt{\frac{\lambda(1-\omega)u}{3}}\, tanh\left(\sqrt{\frac{3(1-\omega)u}{\lambda}}\right)\bar{p}_{fD}(y_D) \quad \text{(B-29)}$$

Substituting Eq. B-29 into the Laplace transform of B-1 and rearranging:

$$\frac{d}{dy_D}\left[\hat{k}_{fD}(y_D)\frac{d\bar{p}_{fD}}{dy_D}\right] = uf(u)\bar{p}_{fD} \quad \text{(B-30)}$$

where:

$$f(u) = \omega + \sqrt{\frac{\lambda(1-\omega)}{3u}}\, tanh\left(\sqrt{\frac{3(1-\omega)u}{\lambda}}\right) \quad \text{(B-31)}$$

In Eq. B-30 we assume that the initial distribution of the fracture pressure is uniform. For pseudosteady fluid transfer, *f(u)* is given by:

$$f_{pss}(u) = \frac{\lambda_{pss}+\omega(1-\omega)u}{\lambda_{pss}+(1-\omega)u} \quad \text{(B-32)}$$

where:

$$\lambda_{pss} = \sigma\frac{\hat{k}_m}{\hat{k}_f^0}x_f^2 \quad \text{(B-33)}$$

The definition of ω is the same as Eq. B-19. The parameter σ is the matrix shape factor, equal to $12/L_m^2$ for the geometry shown in Fig 3.1.

Solution for constant production rate (transient fluid transfer from matrix to natural fractures)

The mathematical model for the fracture system in Laplace space reads:

$$\frac{d}{dy_D}\left[\hat{k}_{fD}(y_D)\frac{d\bar{p}_{fD}}{dy_D}\right] = uf(u)\bar{p}_{fD} \quad \text{(B-30)}$$

$$\left(\frac{d\bar{p}_{fD}}{dy_D}\right)_{y_D=0} = -\frac{\pi}{2} \quad \text{(B-34)}$$

$$\left(\frac{d\bar{p}_{fD}}{dy_D}\right)_{y_D=y_D{}^*} = 0 \quad \text{(B-35)}$$

The wellbore pressure solution in Laplace space for exponential permeability field is:

$$\bar{p}_{fwD} = \frac{\delta\pi}{2u\sqrt{uf(u)}}\left[\frac{I_1\left(\frac{2y_D^*\sqrt{uf(u)}}{ln(\xi)}\right)K_0\left(\frac{2y_D^*}{ln(\xi)}\sqrt{\frac{uf(u)}{\hat{k}_D^*}}\right)+I_0\left(\frac{2y_D^*}{ln(\xi)}\sqrt{\frac{uf(u)}{\hat{k}_D^*}}\right)K_1\left(\frac{2y_D^*\sqrt{uf(u)}}{ln(\xi)}\right)}{I_0\left(\frac{2y_D^*\sqrt{uf(u)}}{ln(\xi)}\right)K_0\left(\frac{2y_D^*}{ln(\xi)}\sqrt{\frac{uf(u)}{\hat{k}_D^*}}\right)-I_0\left(\frac{2y_D^*}{ln(\xi)}\sqrt{\frac{uf(u)}{\hat{k}_D^*}}\right)K_0\left(\frac{2y_D^*\sqrt{uf(u)}}{ln(\xi)}\right)}\right] \quad \text{(B-36)}$$

If $\hat{k}_D^* < 1, \delta = -1$ and $\xi = 1/\hat{k}_D^*$; if $\hat{k}_D^* > 1, \delta = 1$ and $\xi = \hat{k}_D^*$. The term *massively stimulated* implies that $\hat{k}_D^* < 1$. The corresponding wellbore pressure solution for linear permeability field is:

$$\bar{p}_{fwD} = \frac{\delta\pi}{2u\sqrt{uf(u)}} \left[\frac{I_1\left(\frac{2y_D^*\sqrt{\hat{k}_D^* uf(u)}}{|\hat{k}_D^*-1|}\right)K_0\left(\frac{2y_D^*\sqrt{uf(u)}}{|\hat{k}_D^*-1|}\right)+I_0\left(\frac{2y_D^*\sqrt{uf(u)}}{|\hat{k}_D^*-1|}\right)K_1\left(\frac{2y_D^*\sqrt{\hat{k}_D^* uf(u)}}{|\hat{k}_D^*-1|}\right)}{I_1\left(\frac{2y_D^*\sqrt{\hat{k}_D^* uf(u)}}{|\hat{k}_D^*-1|}\right)K_1\left(\frac{2y_D^*\sqrt{uf(u)}}{|\hat{k}_D^*-1|}\right)-I_1\left(\frac{2y_D^*\sqrt{uf(u)}}{|\hat{k}_D^*-1|}\right)K_1\left(\frac{2y_D^*\sqrt{\hat{k}_D^* uf(u)}}{|\hat{k}_D^*-1|}\right)} \right] \quad \text{(B-37)}$$

If $\hat{k}_D^* < 1, \delta = -1$; if $\hat{k}_D^* > 1, \delta = 1$. The term *massively stimulated* implies that $\hat{k}_D^* < 1$. For uniform permeability ($\hat{k}_D^* = 1$):

$$\bar{p}_{fwD} = \frac{\pi}{2u\sqrt{uf(u)}} coth(y_D^*\sqrt{uf(u)}) \quad \text{(B-38)}$$

Where *f(u)* is defined in Eq. B-31. I_ν and K_ν are the modified Bessel functions of first and second kind, respectively ($\nu = 0,1$)). The definition of dimensionless PI (constant wellbore rate) is:

$$J_{crD} = \frac{1}{p_{fwD} - 2\pi t_D\left(\frac{1/4}{y_D^*}\right)} \quad \text{(B-39)}$$

Solution for constant wellbore flowing pressure

The mathematical model for CWP is similar to Eqs. B-1 through B-8, except the inner boundary condition:

$$p_{cpfD}(y_D = 0, t_D) = 1 \quad \text{(B-40)}$$

Where p_{cpfD} is the dimensionless fracture pressure:

$$p_{cpfD} = \frac{m(p_i) - m[p_f(y,t)]}{m(p_i) - m(p_{wf})} : gas \quad \text{(B-41a)}$$

$$p_{cpfD} = \frac{p_i - p_f(y,t)}{p_i - p_{wf}} : oil \quad \text{(B-41b)}$$

By using the Convolution theorem (van Everdingen and Hurst 1949), the dimensionless production rate is:

$$\bar{q}_{wD} = \frac{1}{u^2 \bar{p}_{fwD}} \quad \text{(B-42)}$$

Where $\bar{q}_{wD}$ is the Laplace transform of the production rate (constant wellbore pressure) and $\bar{p}_{fwD}$ is the fracture wellbore pressure (constant rate solution, Eqs. B-36 through B-38). These Laplace space solutions were numerically inverted using the Gaver-Wynn-

Rho algorithm (Valkó and Abate 2004). The definitions of dimensionless production rate, cumulative production, and dimensionless PI (constant wellbore pressure) are:

$$q_{wD} = \frac{p_{sc}T}{\pi n_{HF} T_{sc} \hat{k}_f^0 h[m(p_i) - m(p_{wf})]} q_g : gas \quad \text{(B-43a)}$$

$$q_{wD} = \frac{B\mu}{2\pi n_{HF} \hat{k}_f^0 h(p_i - p_{wf})} q_o : oil \quad \text{(B-43b)}$$

$$G_{pD} = \frac{p_{sc}T}{\pi n_{HF} T_{sc} \left(\hat{\phi}_f c_{tf} + \hat{\phi}_m c_{tm}\right)_i \mu_i x_f^2 h[m(p_i) - m(p_{wf})]} G_p : gas \quad \text{(B-44a)}$$

$$N_{pD} = \frac{B}{2\pi n_{HF} \left(\hat{\phi}_f c_{tf} + \hat{\phi}_m c_{tm}\right) x_f^2 h(p_i - p_{wf})} N_p : oil \quad \text{(B-44b)}$$

$$J_{cpD} = \frac{q_{wD}}{\left(1 - \frac{\pi G_{pD}}{2y_D^*}\right)} : gas \quad \text{(B-45a)}$$

$$J_{cpD} = \frac{q_{wD}}{\left(1 - \frac{\pi N_{pD}}{2y_D^*}\right)} : oil \quad \text{(B-45b)}$$

Asymptotic approximations of production rate (exponential, linear, and uniform permeability field)

Short-time approximation for production rate. Transient linear flow in the natural fractures:

$$q_{wlD-STA} = \frac{2}{\pi}\sqrt{\frac{\omega}{\pi t_D}} \quad \text{(B-46)}$$

Short-time approximation for production rate. Transient bilinear flow:

$$q_{wbD-STA} = \frac{2\sqrt[4]{\lambda(1-\omega)}}{\sqrt[4]{3}\pi\Gamma(3/4)\sqrt[4]{t_D}} \quad \text{(B-47)}$$

Intermediate-time approximation for production rate. Linear interporosity flow:

$$q_{wlD-ITA} = \frac{2y_D^*\sqrt{\lambda(1-\omega)}}{\sqrt{3}\pi^{3/2}\sqrt{t_D}} \quad \text{(B-48)}$$

Total recoverable hydrocarbon:

$$N_{pD-MAX} = \frac{2y_D^*}{\pi} \quad \text{(B-49)}$$

Solutions including skin factor

The convolution theorem (van Everdingen and Hurst 1949) facilitates inclusion of the skin factor effect in Laplace space:

$$\bar{p}_{fwDs} = \bar{p}_{fwD} + s/u \quad \text{(B-50)}$$

Where $\bar{p}_{fwDs}$ is the fracture wellbore pressure solution (constant production rate) including skin factor and $\bar{p}_{fwD}$ is the zero-skin solution (Eqs. B-36 through B-38). The corresponding production rate (constant wellbore pressure) in Laplace space is:

$$\bar{q}_{wDs} = \frac{1}{u^2 \bar{p}_{fwDs}} \quad \text{(B-51)}$$

Irrespective of transient linear or bilinear flow at early times, the short-time approximation of production rate in time domain is (s > 0):

$$q_{wDs-STA} = \frac{1}{s} \quad \text{(B-52)}$$

APPENDIX C

INDUCED PERMEABILITY FIELD MODEL – 2ϕ (DWP)

Solution in Laplace space

Fig. C-1 shows the conceptual model for the variable bottomhole pressure approach:

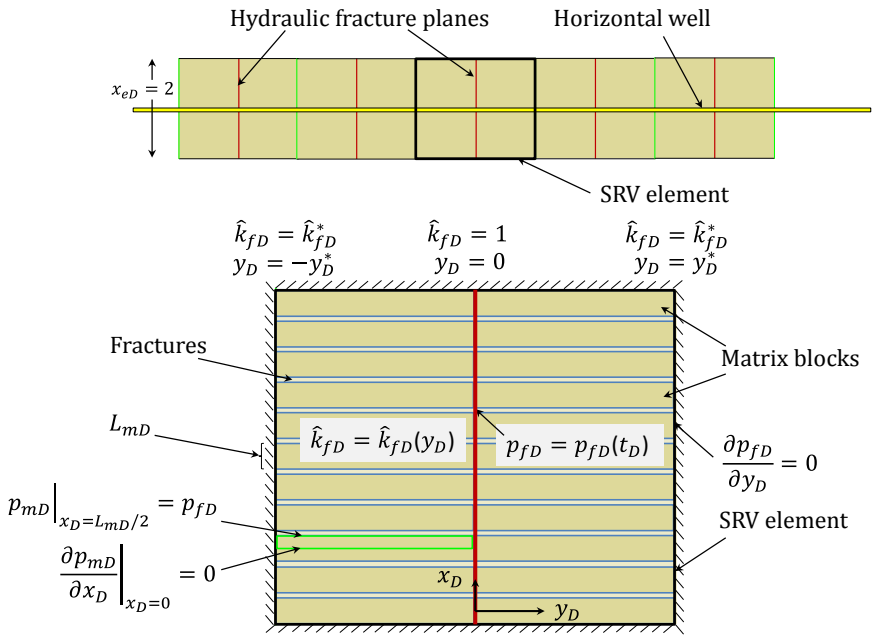

Fig. C-1—Induced permeability field in the double-porosity/double permeability idealization. Decaying wellbore pressure approach at the inner boundary condition.

Using the Convolution theorem:

$$\bar{q}_{wDs\tau} = \frac{\bar{p}_{wfexpD}}{u\bar{p}_{fwDs}} \quad \text{(C-1)}$$

Where $\bar{p}_{fwDs}$ is the fracture wellbore pressure including skin factor (Eq. B-50), and $\bar{q}_{wDs\tau}$ is the production rate (decaying wellbore pressure) in Laplace space. The numerator $\bar{p}_{wfexpD}$ in Eq. C-1 is the Laplace transform of the decaying bottomhole flowing pressure function:

$$p_{wfexpD}(t_D) = 1 - exp(-t_D/\tau_D) \quad \text{(C-2)}$$

Hence:

$$\bar{p}_{wfexpD} = \frac{1}{u} - \frac{1}{u+1/\tau_D} \quad \text{(C-3)}$$

τ_D is defined as follows:

$$\tau_D = \frac{\hat{k}_f^0 \tau}{(\widehat{\phi_f c_{tf}} + \widehat{\phi_m c_{tm}})_i \mu_i x_f^2} : gas \quad \text{(C-4a)}$$

$$\tau_D = \frac{\hat{k}_f^0 \tau}{(\widehat{\phi_f c_{tf}} + \widehat{\phi_m c_{tm}}) \mu x_f^2} : oil \quad \text{(C-4b)}$$

Where τ is the mean lifetime, representing the time when 63% of the total wellbore pressure change has happened after the start of production. We can use different functions to match the field data, such as the *hill-shaped* function:

$$p_{wfhillD}(t_D) = 1 - \frac{1}{1+t_D/\tau_D} \quad \text{(C-5)}$$

The Laplace transform of Eq. C-5 is:

$$\bar{p}_{wfhillD} = \frac{1}{u} + \tau_D e^{\tau_D u}\, Ei(-u\tau_D) = \frac{1}{u} - \tau_D e^{\tau_D u}\, \Gamma(0, u\tau_D) \quad \text{(C-6)}$$

Where $Ei(-u\tau_D)$ and $\Gamma(a,x)$ are the exponential integral and incomplete gamma functions, respectively. The dimensionless functions $p_{wfexpD}(t_D)$ and $p_{wfhillD}(t_D)$ are defined as $[p_i - p_{wf}(t)]/[p_i - p_{wf,stab}]$; $p_{wf,stab}$ is the stabilized value of the bottomhole flowing pressure.

Short-time approximations of production rate (exponential, linear, and uniform permeability field)

Transient linear flow in the natural fractures (Eq. B-46), no skin factor (*s*=0), and decaying wellbore pressure (Eq. C-2):

$$q_{wlD\tau-STA} = \frac{4\sqrt{\omega}\sqrt{t_D}}{\pi^{3/2}\tau_D} \quad \text{(C-7)}$$

Transient bilinear flow (Eq. B-47), no skin factor (*s*=0), and decaying wellbore pressure:

$$q_{wbD\tau-STA} = \frac{8\sqrt[4]{\lambda(1-\omega)}{t_D}^{3/4}}{3\sqrt[4]{3}\pi\Gamma(3/4)\tau_D} \quad \text{(C-8)}$$

Transient linear or bilinear flow including skin factor and decaying wellbore pressure:

$$q_{wDs\tau-STA} = \frac{t_D}{s\,\tau_D} \quad \text{(C-9)}$$

The short-term approximations using the hill-shaped function (Eq. C-5) are the same as C-7 through C-9.

APPENDIX D

INDUCED INTERPOROSITY FLOW FIELD MODEL

Solution for constant production rate

Fig. D-1 presents the conceptual model of the induced interporosity flow field:

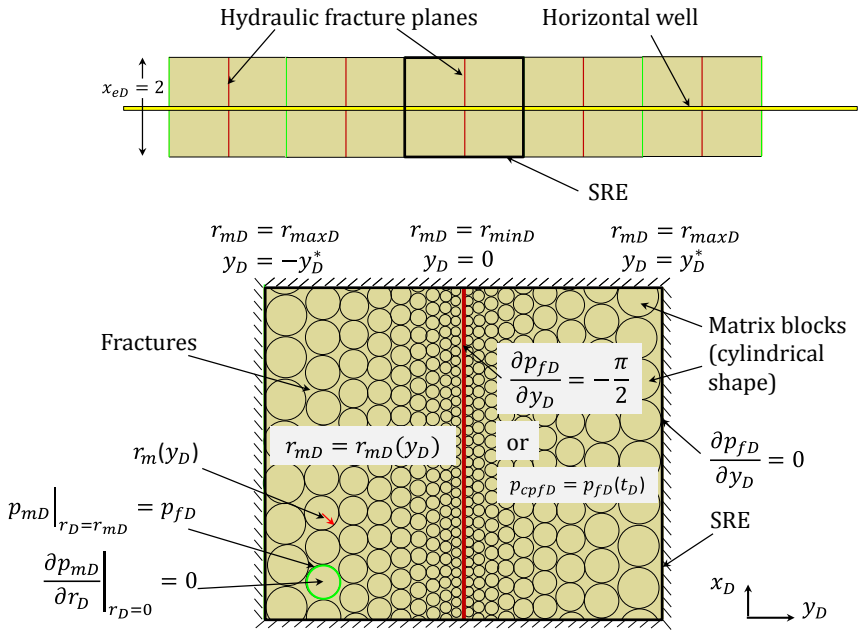

Fig. D-1— Plain view of an MFHW. The characteristic size of the matrix blocks gradually increases away from the hydraulic fracture plane.

The mathematical model for the fracture system and matrix blocks reads as:

$$\frac{\partial^2 p_{fD}}{\partial y_D^2} - q_{mfD} = \omega \frac{\partial p_{fD}}{\partial t_D}; 0 < y_D < y_D^* \quad \text{.....(D-1)}$$

$$p_{fD}(y_D, t_D = 0) = 0 \quad \text{(D-2)}$$

$$\left(\frac{\partial p_{fD}}{\partial y_D}\right)_{y_D=0} = -\frac{\pi}{2} \quad \text{(D-3)}$$

$$\left(\frac{\partial p_{fD}}{\partial y_D}\right)_{y_D=y_D{}^*} = 0 \quad \text{(D-4)}$$

$$\frac{1}{r_D}\frac{\partial}{\partial r_D}\left(r_D\frac{\partial p_{mD}}{\partial r_D}\right) = \alpha^2\frac{\partial p_{mD}}{\partial t_D}; 0 < r_D < r_{mD}(y_D) \quad \text{(D-5)}$$

$$p_{mD}(r_D, t_D = 0) = 0 \quad \text{(D-6)}$$

$$\left(\frac{\partial p_{mD}}{\partial r_D}\right)_{r_{mD}=0} = 0 \quad \text{(D-7)}$$

$$p_{mD}(r_{mD}(y_D), t_D) = p_{fD}. \quad \text{(D-8)}$$

where:

$$p_{jD} = \frac{\pi n_{HF} T_{sc} \hat{k}_f h[m(p_i) - m(p_j)]}{q_w p_{sc} T} : gas; (j = f \text{ or } m), \quad \text{(D-9a)}$$

$$p_{jD} = \frac{2\pi n_{HF} \hat{k}_f h(p_i - p_j)}{q_w B\mu} : oil; \ (j = f \text{ or } m) \quad \text{(D-9b)}$$

$$t_D = \frac{\hat{k}_f t}{(\hat{\phi}_f \hat{c}_{tf} + \hat{\phi}_m \hat{c}_{tm})_i \mu_i x_{HF}^2} : gas \quad \text{(D-10a)}$$

$$t_D = \frac{\hat{k}_f t}{(\hat{\phi}_f \hat{c}_{tf} + \hat{\phi}_m \hat{c}_{tm}) \mu x_{HF}^2} : oil \quad \text{(D-10b)}$$

$$y_D = y/x_{HF} \quad \text{(D-11)}$$

$$y_D^* = y^*/x_{HF} \quad \text{(D-12)}$$

$$r_D = r/x_{HF} \quad \text{(D-13)}$$

$$r_{mD}(y_D) = r_m(y)/x_{HF} \quad \text{(D-14)}$$

$$q_{mfD} = \frac{2}{r_{mD}(y_D)} \frac{\hat{k}_m}{\hat{k}_f} \left(\frac{\partial p_{mD}}{\partial r_D} \right)_{r_D = r_{mD}(y_D)} \quad \text{(D-15)}$$

$$\omega = \frac{\hat{\phi}_{fi} \hat{c}_{tfi}}{\hat{\phi}_{fi} \hat{c}_{tfi} + \hat{\phi}_{mi} \hat{c}_{tmi}} \quad \text{(D-16)}$$

$$\alpha^2 = (1 - \omega) \frac{\hat{k}_m}{\hat{k}_f} \quad \text{(D-17)}$$

$m(p)$ is the pseudopressure function (Al-Hussainy et al. 1966). The matrix equation and its boundary conditions in Laplace space are:

$$\frac{1}{r_D}\frac{d}{dr_D}\left(r_D\frac{d\bar{p}_{mD}}{dr_D}\right)=\alpha^2 u\bar{p}_{mD};\ 0<r_D<r_{mD}(y_D) \quad \text{(D-18)}$$

$$\left(\frac{d\bar{p}_{mD}}{dr_D}\right)_{r_D=0}=0 \quad \text{(D-19)}$$

$$\bar{p}_{mD}(r_{mD})=\bar{p}_{fD} \quad \text{(D-20)}$$

In Eq. D-18 we assume that the initial distribution of matrix pressure is uniform. $\bar{p}_{jD}$ is the Laplace transform of p_{jD} (j = f, m) and u is the Laplace variable of t_D. The solution of Eqs. D-18 through D-20 is:

$$\bar{p}_{mD}(r_D)=\frac{I_0(\sqrt{u}\alpha r_D)}{I_0(\sqrt{u}\alpha r_{mD})}\bar{p}_{fD}(y_D) \quad \text{(D-21)}$$

Hence,

$$\left(\frac{d\bar{p}_{mD}}{dr_D}\right)_{r_D=r_{mD}(y_D)}=\frac{I_1(\sqrt{u}\alpha r_{mD})}{I_0(\sqrt{u}\alpha r_{mD})}\,\alpha\sqrt{u}\bar{p}_{fD}(y_D) \quad \text{(D-22)}$$

where I_ν is the modified Bessel function of the first kind ($\nu = 0,1$). Substituting Eq. D-17 into Eq. D-22:

$$\frac{2}{r_{mD}}\frac{\hat{k}_m}{\hat{k}_f}\left(\frac{d\bar{p}_{mD}}{dr_D}\right)_{r_D=r_{mD}(y_D)} = \frac{\lambda(y_D)}{4}\sqrt{\frac{8(1-\omega)u}{\lambda(y_D)}}\frac{I_1\left(\sqrt{\frac{8(1-\omega)u}{\lambda(y_D)}}\right)}{I_0\left(\sqrt{\frac{8(1-\omega)u}{\lambda(y_D)}}\right)}\bar{p}_{fD}(y_D) \quad \text{(D-23)}$$

where

$$\lambda(y_D) = \frac{8}{r_m^2(y)}\frac{\hat{k}_m}{\hat{k}_f}x_{HF}^2 = \frac{8}{r_{mD}^2(y_D)}\frac{\hat{k}_m}{\hat{k}_f} \quad \text{(D-24)}$$

Substituting Eq. D-24 into the Laplace transform of D-15:

$$\bar{q}_{mfD} = \frac{\lambda(y_D)}{4}\sqrt{\frac{8(1-\omega)u}{\lambda(y_D)}}\frac{I_1\left(\sqrt{\frac{8(1-\omega)u}{\lambda(y_D)}}\right)}{I_0\left(\sqrt{\frac{8(1-\omega)u}{\lambda(y_D)}}\right)}\bar{p}_{fD}(y_D) \quad \text{(D-25)}$$

Substituting Eq. D-25 into the Laplace transform of D-1 and rearranging:

$$\frac{d^2\bar{p}_{fD}}{dy_D^2} = uf(u, y_D)\bar{p}_{fD} \quad \text{(D-26)}$$

where:

$$f(u, y_D) = \omega + \frac{\lambda(y_D)}{4u}\sqrt{\frac{8(1-\omega)u}{\lambda(y_D)}}\frac{I_1\left(\sqrt{\frac{8(1-\omega)u}{\lambda(y_D)}}\right)}{I_0\left(\sqrt{\frac{8(1-\omega)u}{\lambda(y_D)}}\right)} \quad \text{(D-27)}$$

The boundary conditions for the fracture system in Laplace space are:

$$\left(\frac{d\bar{p}_{fD}}{dy_D}\right)_{y_D=0} = -\frac{\pi}{2u} \quad \text{(D-28)}$$

$$\left(\frac{d\bar{p}_{fD}}{dy_D}\right)_{y_D=y_D{}^*} = 0 \quad \text{(D-29)}$$

If we assume linear and exponential variations of the characteristic dimension of the matrix blocks:

$$r_{mD}(y_D) = r_m(y)/x_{HF} = r_{minD}(1 + m_{rD}y_D): linear \quad \text{(D-30a)}$$

$$r_{mD}(y_D) = r_m(y)/x_{HF} = r_{minD}e^{m_{rD}y_D}: exponential \quad \text{(D-30b)}$$

$$\lambda(y_D) = \frac{8}{[r_{mD}(y_D)]^2}\frac{\hat{k}_m}{\hat{k}_f} = \frac{\lambda_{max}}{\left[1+\left(\sqrt{\lambda_{max}/\lambda_{min}}-1\right)(y_D/y_D^*)\right]^2}: linear \quad \text{(D-31a)}$$

$$\lambda(y_D) = \frac{8}{[r_{mD}(y_D)]^2}\frac{\hat{k}_m}{\hat{k}_f} = \lambda_{max}e^{-2m_{rD}y_D}: exponential \quad \text{(D-31b)}$$

$$m_{rD} = \frac{\sqrt{\lambda_{max}/\lambda_{min}}-1}{y_D^*}: linear \quad \text{(D-32a)}$$

$$m_{rD} = \frac{ln(\lambda_{max}/\lambda_{min})}{2y_D^*} : exponential \quad \text{(D-32b)}$$

$$\lambda_{max} = \frac{8}{r_{min}^2}\frac{\hat{k}_m}{\hat{k}_f}x_{HF}^2 = \frac{8}{r_{minD}^2}\frac{\hat{k}_m}{\hat{k}_f} \quad \text{(D-33)}$$

$$\lambda_{min} = \frac{8}{r_{max}^2}\frac{\hat{k}_m}{\hat{k}_f}x_{HF}^2 = \frac{8}{r_{maxD}^2}\frac{\hat{k}_m}{\hat{k}_f} \quad \text{(D-34)}$$

In general:

$$\frac{r_{maxD}}{r_{minD}} = \frac{r_{max}/x_{HF}}{r_{min}/x_{HF}} = \frac{r_{max}}{r_{min}} = \sqrt{\frac{\lambda_{max}}{\lambda_{min}}} \quad \text{(D-35)}$$

The Airy-spline scheme

Eqs. D-26 through D-29 were solved by dividing the spatial domain ($0 \le y_D \le y_D^*$) into J segments, such that the function $g = uf(u, y_D)$ can be approximated by a linear equation in each segment for any fixed u:

$$\frac{d^2\bar{p}_{fDa}}{dy_D^2} - g(y_D)\bar{p}_{fDa} = 0; \quad y_{Dl} < y_D < y_{Dr} \quad \text{(D-36)}$$

$$g(y_D) = g_l\frac{y_{Dr}-y_D}{y_{Dr}-y_{Dl}} + g_r\frac{y_D-y_{Dl}}{y_{Dr}-y_{Dl}} \quad \text{(D-37)}$$

with the boundary conditions:

$$\left(\frac{d\bar{p}_{fDa}}{dy_D}\right)_{y_D=y_{Dl}} = \bar{p}'_{fDl} \quad \text{(D-38)}$$

$$\left(\frac{d\bar{p}_{fDa}}{dy_D}\right)_{y_D=y_{Dr}} = \bar{p}'_{fDr} \quad \text{(D-39)}$$

where y_{Dl} and y_{Dr} are the coordinates of the left and right boundaries in each segment, respectively. g_l and g_r are the values of $uf(u, y_D)$ at the left and right boundaries of each segment, respectively (**Fig. D-2**). The variable coefficient (g) is equal to the true function [$uf(u, y_D)$] at the boundaries between the segments, for any particular value of the u variable.

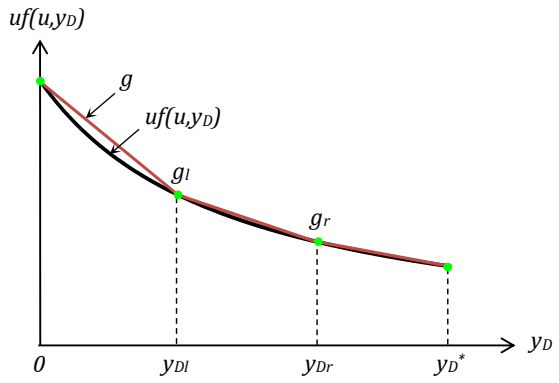

Fig. D-2—Discretization scheme to solve the ordinary differential equation using linear segments

The general solution of Eqs. D-36 through D-39 is:

$$\bar{p}_{fDa} = \frac{Ai\left(\frac{x_2 - yx_1}{x_1^{2/3}}\right)\left[\bar{p}'_{fDl}Bi'\left(\frac{g_r}{x_1^{2/3}}\right) - \bar{p}'_{fDr}Bi'\left(\frac{g_l}{x_1^{2/3}}\right)\right] - Bi\left(\frac{x_2 - yx_1}{x_1^{2/3}}\right)\left[\bar{p}'_{fDl}Ai'\left(\frac{g_r}{x_1^{2/3}}\right) + \bar{p}'_{fDr}Ai'\left(\frac{g_l}{x_1^{2/3}}\right)\right]}{\sqrt[3]{x_1}\left[Bi'\left(\frac{g_l}{x_1^{2/3}}\right)Ai'\left(\frac{g_r}{x_1^{2/3}}\right) - Ai'\left(\frac{g_l}{x_1^{2/3}}\right)Bi'\left(\frac{g_r}{x_1^{2/3}}\right)\right]} \quad \text{.....(D-40)}$$

where:

$$x_1 = \frac{g_l - g_r}{y_{Dr} - y_{Dl}} \quad \text{.....(D-41)}$$

$$x_2 = \frac{g_r\, y_{Dl} + g_l\, y_{Dr}}{y_{Dl} - y_{Dr}} \quad \text{.....(D-42)}$$

Ai(x) and *Bi(x)* are the Airy functions. We call this technique the Airy-spline scheme because the solution in each segment (Eq. D-40) is expressed in terms of Airy functions. In addition, the approximation $\bar{p}_{fDa}$ is continuous and has continuous first derivative. Note that:

$$\bar{p}_{fDa} = \bar{p}_{fDa}\left(y_{Dl}, y_{Dr}, g_l, g_r, \bar{p}'_{fDl}, \bar{p}'_{fDr}, y_D\right); \quad y_{Dl} \le y_D \le y_{Dr} \quad \text{.....(D-43)}$$

Thus, for a given set of reservoir properties, and a discretization scheme with *J* segments, the approximation of the fracture pressure in each segment is:

$$\bar{p}_{fDa1} = \bar{p}_{fDa}\left(0, y_{Dr1}, g_{l1}, g_{r1}, -\pi/(2u), \bar{p}'_{fDr1}, y_D\right); \qquad 0 \le y_D \le y_{D1};\ j = 1$$
$$\bar{p}_{fDaj} = \bar{p}_{fDa}\left(y_{Dlj}, y_{Drj}, g_{lj}, g_{rj}, \bar{p}'_{fDlj}, \bar{p}'_{fDrj}, y_D\right); y_{Dj} \le y_D \le y_{Dj+1};\ j = 2,3,..J-1 \quad \text{(D-44)}$$
$$\bar{p}_{fDaJ} = \bar{p}_{fDa}\left(y_{DlJ}, y_D^*, g_{lJ}, g_{rJ}, \bar{p}'_{fDlJ}, 0, y_D\right); \qquad y_{DJ-1} \le y_D \le y_D^*;\ j = J$$

These equations can be coupled by pressure continuity at the boundaries, leading to a system of (*J*-1) equations with (*J*-1) unknowns. The unknowns are the derivatives of the fracture pressure at the inner boundaries. The linear system has a *tri-diagonal structure*, as shown in **Fig. D-3** (this is an example with 40 segments).

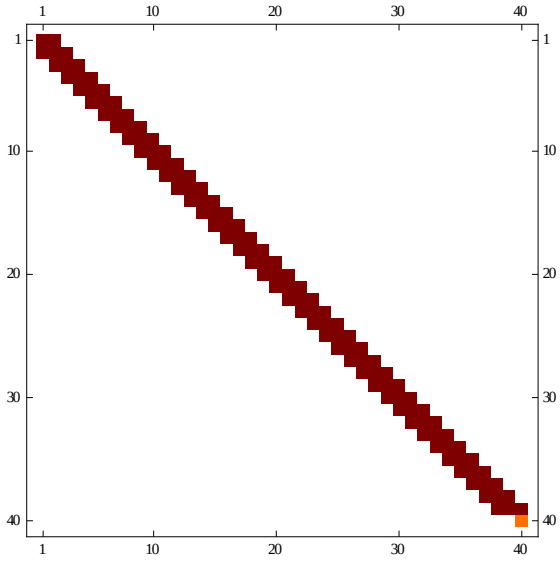

Fig. D-3—The linear system has a tri-diagonal structure. The elements of the matrix depend on the Airy functions evaluated at the boundaries between grid elements.

After solving the system D-44 for the pressure derivatives at the inner boundaries, we take the first segment to determine the fracture pressure at the hydraulic fracture face (y_D=0):

$$\bar{p}_{wfDa}(u) = \bar{p}_{fDa}(0, y_{Dr1}, g_{l1}, g_{r1}, -\pi/(2u), \bar{p}'_{fDr1}, 0) \quad \text{(D-45)}$$

At this step, all the arguments of Eq. D-45 are known, depending only on the Laplace parameter *u*. This approach can be used when the continuously varying function $uf(u, y_D)$ can be approximated by linear segments (as a function of location, y_D). For any value of the Laplace variable, the tri-diagonal system of linear equations has to be solved also in multi-precision, but that can be easily done in *Mathematica* (2012).

Solution for constant wellbore pressure

In this case, the inner boundary condition is:

$$p_{cpfD}(y_D = 0, t_D) = 1 \quad \text{(D-46)}$$

where p_{cpfD} is the dimensionless fracture pressure:

$$p_{cpfD} = \frac{m(p_i) - m[p_f(y,t)]}{m(p_i) - m(p_{wf})} : gas \quad \text{(D-47)}$$

$$p_{cpfD} = \frac{p_i - p_f(y,t)}{p_i - p_{wf}} : oil \quad \text{(D-48)}$$

The dimensionless production rate was obtained using the Convolution theorem (van Everdingen and Hurst 1949):

$$\bar{q}_{wD} = \frac{1}{u^2 \bar{p}_{fwDa}(u)} \quad \text{(D-49)}$$

where $\bar{q}_{wD}$ is the Laplace transform of the production rate (constant wellbore pressure) and $\bar{p}_{fwDa}(u)$ is the fracture wellbore pressure (constant rate solution, Eq. D-45). The inclusion of the skin factor was performed using the following expressions:

$$\bar{p}_{fwDas} = \bar{p}_{fwDa}(u) + s/u \quad \text{(D-50)}$$

$$\bar{q}_{wDas} = \frac{1}{u^2 \bar{p}_{fwDas}} \quad \text{(D-51)}$$

where $\bar{p}_{fwDas}$ is the fracture wellbore-pressure solution (constant production rate) including skin factor and $\bar{p}_{fwDa}$ is the zero-skin solution (Eq. A-45). $\bar{q}_{wDas}$ is the dimensionless production rate (constant wellbore pressure) including skin factor. These equations were numerically inverted using the multi-precision Gaver-Wynn-Rho algorithm (Valkó and Abate 2004). The definitions of the dimensionless production rate, cumulative production, and skin factor are:

$$q_{wD} = \frac{p_{sc}T}{\pi n_{HF} T_{sc} \hat{k}_f h [m(p_i) - m(p_{wf})]} q_g : gas \quad \text{(D-52)}$$

$$q_{wD} = \frac{B\mu}{2\pi n_{HF} \hat{k}_f h (p_i - p_{wf})} q_o : oil \quad \text{(D-53)}$$

$$G_{pD} = \frac{p_{sc}T}{\pi n_{HF}T_{sc}\left(\hat{\phi}_f\hat{c}_{tf}+\hat{\phi}_m\hat{c}_{tm}\right)_i\mu_i x_{HF}^2 h\left[m(p_i)-m(p_{wf})\right]} G_p : gas \quad \text{(D-54)}$$

$$N_{pD} = \frac{B}{2\pi n_{HF}\left(\hat{\phi}_f\hat{c}_{tf}+\hat{\phi}_m\hat{c}_{tm}\right)x_{HF}^2 h(p_i-p_{wf})} N_p : oil \quad \text{(D-55)}$$

$$s = \frac{\pi n_{HF}T_{sc}\hat{k}_f h\left[m(p_{wf,ns})-m(p_{wf,s})\right]}{p_{sc}Tq_g} : gas \quad \text{(D-56)}$$

$$s = \frac{2\pi n_{HF}\hat{k}_f h(p_{wf,s}-p_{wf,ns})}{B\mu\, q_o} : oil \quad \text{(D-57)}$$

$p_{wf,s}$ is the actual wellbore pressure with the skin factor effect and $p_{wf,ns}$ is the ideal wellbore pressure with no skin factor. The variable wellbore-pressure solution was obtained using the methodology described in section 3.